5-2014

4D reduced TE (RTE) spiral phase contrast NRI for rapid quantification and visualization of blood flow and hemodynamics.

Mohammadjavad Negahdar
University of Louisville

4D REDUCED TE (RTE) SPIRAL PHASE CONTRAST MRI FOR RAPID QUANTIFICATION AND VISUALIZATION OF BLOOD FLOW AND HEMODYNAMICS

By:

Mohammadjavad Negahdar

M.S., Telecommunication Engineering, K.N.Toosi University of Technology
B.S., Electrical Engineering, K. N. Toosi University of Technology

A Dissertation
Submitted to the Faculty of the
J. B. Speed School of Engineering of the University of Louisville
in Partial Fulfillment of the Requirements
for the Degree of

Doctor of Philosophy

Department of Electrical and Computer Engineering
University of Louisville
Louisville, Kentucky

May 2014

4D REDUCED TE (RTE) SPIRAL PHASE CONTRAST MRI FOR RAPID QUANTIFICATION AND VISUALIZATION OF BLOOD FLOW AND HEMODYNAMICS

By

Mohammadjavad Negahdar

M.S., Telecommunication Engineering, K.N.Toosi University of Technology

B.S., Electrical Engineering, K. N. Toosi University of Technology

A Dissertation Approved on

April 22, 2014

By the following Dissertation Committee

_____

Dr. Amir A. Amini

_____

Dr. Jacek M. Zurada

_____

Dr. Marcus F. Stoddard

_____

Dr. Guruprasad A. Giridharan

_____

Dr. Tamer Inanc

DEDICATION

I am dedicating this thesis to four beloved people who have meant and continue to mean so much to me. To my father, Ali who provided me with best kind of support and love. To my mother, Houri, who taught me that even the largest task can be accomplished if it is done one step at a time. To my sister, Elaheh, for her countless love and encouragement. And to my brother, Reza who is someone to lean on, someone to count on.

ACKNOWLEDGEMENTS

This dissertation is a result of team members without each of whom it would not have been possible to perform. First of all I would like to express my deep gratitude to my PhD advisor, Dr. Amir A Amini, whose professionalism, ambition and knowledge was the biggest support and guidance through my PhD dissertation. Dr. Amini spent countless hours discussing the technical approach, providing comments and help with the derivations, and helping prepare manuscripts and papers. During my PhD I enjoyed collaboration with Philips Healthcare, VA medical Center and the School of Medicine at University of Louisville. I would like to thank Dr. Marcus Stoddard for the special time and dedication he provided in various collaborations and in my PhD dissertation. Special thanks for the helpful and practical comments and guidance that I received from Dr. Guruprasad A Giridharan. I would also like to express my heartfelt thanks to the other members of my committee: Dr. Jacek M. Zurada, and Dr. Tamer Inanc, for their precious time and invaluable comments on my dissertation. I also would like to thank my previous committee member, Dr. Stephen Fischer (1963-2011), for helping me to learn deep concepts in MRI and pulse programming during my internship in Philips Healthcare.

I also would like to acknowledge the people with whom I have worked in the last five and a half years. First, I would like to thank my previous lab mate Dr. Mo Kadbi. We had a productive collaboration together during my PhD study resulting in many publications in the Medical Imaging Lab. I also would like to thank Jungwon Cha for his help and

support in many phantom studies. Special thanks to all of my collaborators: Dr. Motaz Alshaher, Dr. Melanie Traughber, Dr. Hui Wang, Dr Vahid Tavakolli, Mr Michael Kendrick and Ms. Rita Longaker.

Finally, I wish to express my gratitude to my family for their countless love and support during my study. Special thanks to my brother Reza for his encouragement and support in my life.

ABSTRACT

4D REDUCED TE (RTE) SPIRAL PHASE CONTRAST MRI FOR RAPID QUANTIFICATION AND VISUALIZATION OF BLOOD FLOW AND HEMODYNAMICS

Mohammadjavad Negahdar

April 22, 2014

4D flow Phase Contrast MRI is a relatively new technique in MRI which is capable of deriving time-resolved three-dimensional velocity fields in a 3D volume noninvasively. 4D flow imaging is a 3D k-space acquisition where for the third dimension, an additional phase-encoding step is required. The velocity field can then be used to obtain flow waveform, wall shear stress, vascular compliance, blood pressure, and other hemodynamic information. A significant limitation of 4D flow methods has been the requisite long scan times, requiring the patient to remain motionless at times on the order of 10-20 minutes, depending on scan parameters. The scan times may become more prohibitive in case of 4D cardiovascular studies where respiratory gating with navigator echoes is required.

In this thesis the feasibility of using a reduced TE stack of spirals k-space acquisition for 4D flow imaging are investigated. Starting with fundamentals of MRI, the basics of Phase contrast and 4D flow MRI are thoroughly discussed in Chapter 1-3 and subsequently experimental phantom results are reported in Chapter 4, pointing to the feasibility of performing highly accurate 4D velocity and flow measurement with the proposed pulse sequence under a variety of flow conditions and with substantial reductions in scan time when compared to conventional 4D flow. In phantom studies, results based on the root mean square error criterion indicate that 4D Reduced TE (RTE) Spiral PC MRI is capable of providing the same level of accuracy as conventional 4D conventional PC MRI but in a much shorter scan time (30% reduction in scan time when imaging an FOV of 100*100*60 mm^3 and spatial resolution of 1.5*1.5*3 mm^3). Moreover, the proposed method has the added advantage of achieving the shorter echo time of 2 ms versus 3.6 ms for conventional 4D flow at Q=50ml/s and 1.57 ms versus 3.2 ms at the higher flow rate of Q=150 ml/s leading to more accurate assessment of flow distal to narrowings. Statistical results indicate that at low flow rates performance of both methods are similar. At higher flow rates, however, 4D RTE spiral flow achieves better accuracy. Qualitative results in phantom studies also revealed that at higher flow rates, better flow visualization was achieved with4D RTE spiral flow compared with conventional 4D flow.

In the second part of Chapter 4, we also report on application of the proposed sequence, in-vivo, to 5 healthy volunteers and 5 subjects with mild to moderate Aortic Stenosis (AS) disease. Results from the proposed method were statistically correlated with velocity profiles derived from conventional 4D flow and Doppler Ultrasound. Results

indicate that 4D RTE Spiral is capable of providing the same level of accuracy in flow measurement as Conventional 4D flow MRI for imaging of the aortic valve, but on average resulted in a 30% reduction in scan time and 45% reduction in echo time. 4D RTE Spiral was also able to achieve an echo time of 1.68 ms versus 2.9 ms for that of conventional 4D flow MRI, permitting less signal dephasing in the presence of jet flows distal to occlusions.

With Doppler Ultrasound adopted as the reference method, 4D RTE Spiral flow measured peak velocity and maximum pressure gradient with a higher level of accuracy when compared to Conventional 4D flow MRI. Both methods measured left-ventricular out flow tract (LVOT) diameter, Aortic Valve (AV) eject time and time to AV peak with same accuracy. It is concluded that 4D RTE Spiral flow MRI is an excellent technique for flow measurement in cardiac patients who are unable to tolerate longer scan times, currently required by conventional 4D flow methods.

TABLE OF CONTENTS

LIST OF TABLES

LIST OF FIGURES

FIGURE PAGE

CHAPTER 1

MAGNETIC RESONANCE IMAGING (MRI)

1.1. Introduction

Magnetic Resonance Imaging (MRI) is a non-invasive 3D imaging technique which uses non-ionizing radiation and provides anatomical and functional images with superb contrast. Although MRI has acceptable spatio-temporal resolutions (around 1mm spatial resolution and less than 20ms temporal resolution), its spatial resolution is less than other modalities like X-ray computed tomography (CT) and ultrasound (US) and its temporal resolution is less than ultrasound. MRI is based on the well-known physical phenomenon called Nuclear Magnetic Resonance (NMR), first observed by Felix Bloch and Edward Purcell in 1946. This chapter will describe physical principles and underpinnings of magnetic resonance imaging.

1.2. Nuclear magnetic moment

The basis for NMR is the microscopic magnetic moment of the atomic nuclei. To be NMR active, a specific nucleus needs to possess a non-zero spin quantum number determined by its number of protons and neutrons. In nuclei with an even number of protons and neutrons, spins cancel each other out rendering the net spin equal to zero.

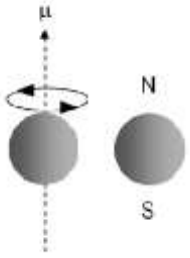

Figure 1: Precession of proton generates a magnetic moment which behaves like a microscopic bar magnet with a north and a south pole. Taken from [1].

In the case of nuclei with an odd number of protons and an odd number of neutrons, the spin quantum number is an integer. However in the case of odd mass number (sum of protons and neutrons) the net spin number is a half integer (i.e. ½, 3/2, 5/2).

A nucleus with nonzero spin quantum number is called NMR-active since it will have a non-zero magnetic moment which can be used to generate a detectable radiofrequency (RF) signal at Larmor frequency. NMR active nuclei, such as the ^{1}H (containing a single proton and no neutron) rotate about itself (Figure 1), generating a magnetic moment μ. In particular, μ describes the strength and direction of a microscopic magnetic field which surrounds the nucleus and is defined as:

$$\mu = \gamma h \sqrt{I(I+1)}/2\pi \qquad (1)$$

where γ is the gyromagnetic ratio and has units of radian per second per tesla and is specific to each nucleus, h is the Planck's constant and I is the spin quantum number. Table 1 shows gyromagnetic ratio of commonly used NMR active elements. ^{1}H, ^{13}C, ^{31}P and ^{19}F are important in MR imaging; however, because of the abundance of ^{1}H in the human body, most diagnostic MR imaging procedures utilize protons due to availability of a stronger NMR signal.

Table 1 Gyromagnetic ratios for common NMR active nuclei used in NMR and MRI.

	Nucleus	$\gamma/2\pi$ [MHz/ Tesla]
Gyromagnetic ratio	^{1}H	42.58
	^{13}C	10.71
	^{19}F	40.08
	^{31}P	17.24

Although the magnitude of magnetic moment is constant and known for NMR-active elements, in the absence of an external magnetic field, its direction is completely random

and variable (Figure 2), and as a result, the sum of magnetic moments of the ensemble has a net zero value. To obtain an NMR signal from magnetic moments of nuclei, all individual moments are needed to constructively sum. This can be achieved by introducing an external static magnetic field, typically referred to as the B_0 field.

Based on the quantum mechanical description, protons cannot attain an arbitrary energy level and consequently their magnetic moment cannot attain an arbitrary angle with the external magnetic field B_0. Indeed, in the presence of an external magnetic field, μ is either aligned parallel or antiparallel to B_0 at an angle of $\mp 54.7^{\circ}$ (Figure 3). This gives rise to two energy levels for the corresponding spins. The spins in the antiparallel state are in the high energy state and the spins in the parallel state are in a low energy state.

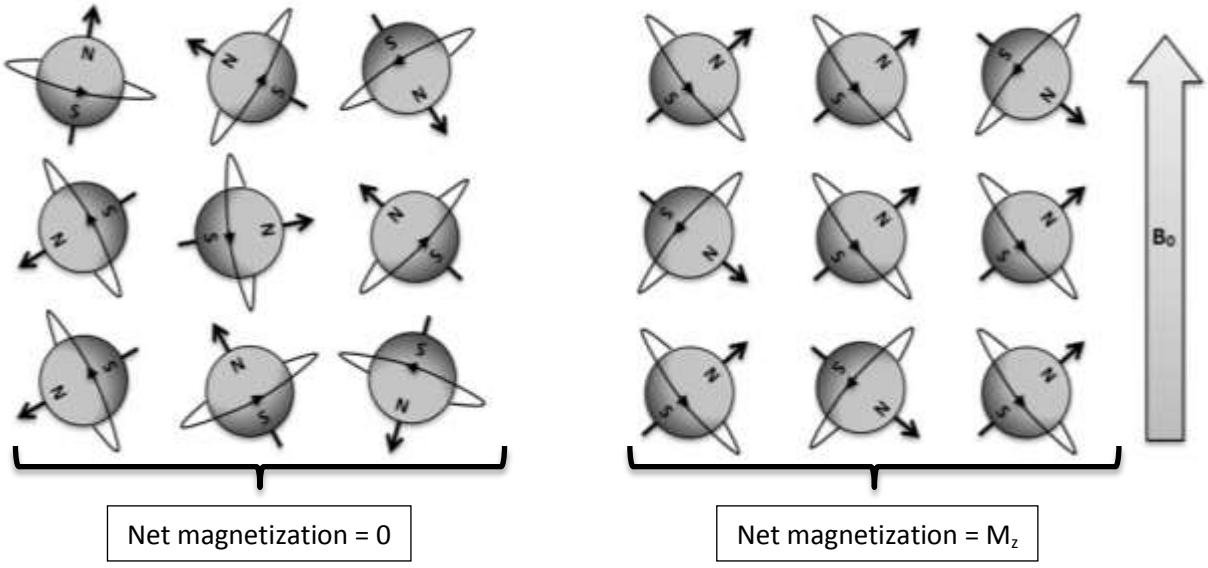

Figure 2: Proton alignments in the absence (left) and in the presence (right) of an external static magnetic field. In the absence of an external magnetic field, the directions of magnetic moments are completely random, resulting in a net zero magnetization. In the presence of an external magnetic field, the protons either become parallel or anti-parallel to the field, though the number that are in the parallel state is slightly larger. The resulting sum becomes non-zero, is detectable, and is the basis for the NMR signal.

The external magnetic field, B_0, attempts to align the spins to be identically parallel to the direction of B_0 – this creates a torque $\vec{C}$ perpendicular to both $\vec{\mu}$ and $\overrightarrow{\mathbf{B_0}}$ vectors (Figure 4). The direction and magnitude of the applied torque may be found from the expression

$$\vec{C} = \vec{\mu} \times \overrightarrow{\mathbf{B_0}} \tag{2}$$

Since $\vec{\mu}$ and $\overrightarrow{\mathbf{B_0}}$ never align, the result of torque is an indefinite precession of the spins around the $\overrightarrow{\mathbf{B_0}}$ field which means that protons with magnetic moment μ, rotate about the z-axis (assuming that $\hat{z}$ is the direction of the external magnetic field), keeping the constant angle between μ and B_0. The angular velocity of nuclear precession is called Larmor frequency and determined by:

$$\omega_0 = \gamma B_0 \tag{3}$$

For example, a hydrogen nucleus precesses at the frequency of 42.58 MHz per Tesla, while a carbon-13 nucleus precesses at 10.71 MHz per Tesla.

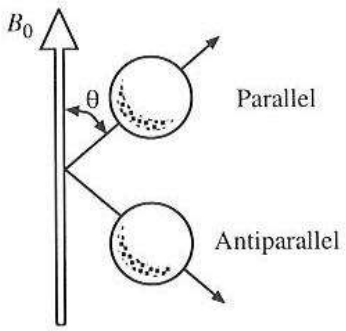

Figure 3: In the presence of an external magnetic field, spins are either parallel (low energy state) or antiparallel (high energy state) to the direction of external magnetic field. Taken from [2]

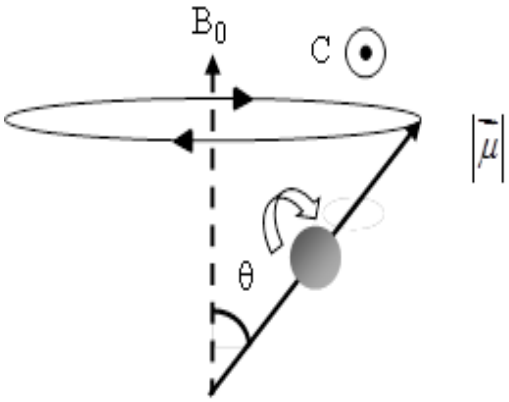

Figure 4: Interaction of external magnetic force, B_0, and magnetic moment, μ, generates a rotational torque, C, in the out of plane direction. Taken from [1].

1.3. Bulk Magnetization

To describe signal acquisition, macroscopic net magnetization vector, **M,** should be introduceed which is the vector sum of all microscopic magnetic moments. With μ_n representing the magnetic moment of the n_{th} nuclear spin, the net magnetization vector, **M,** may be calculated as follows:

$$\overrightarrow{\boldsymbol{M}} = \sum_{n=1}^{N_s} \overrightarrow{\boldsymbol{\mu_n}} \tag{4}$$

where N_S is total number of spins in the volume. If all magnetic moments precess around B_0 and are randomly distributed around a precession cone (Figure 5), it is clear that the in-plane components of magnetic moments cancel each other and this leads to zero in-plane net magnetization. However, the z-component of magnetic moments constructively producing a significant magnetization vector in z-direction. Figure 5 demonstrates distribution of individual magnetic moments, precessing around the z-axis.

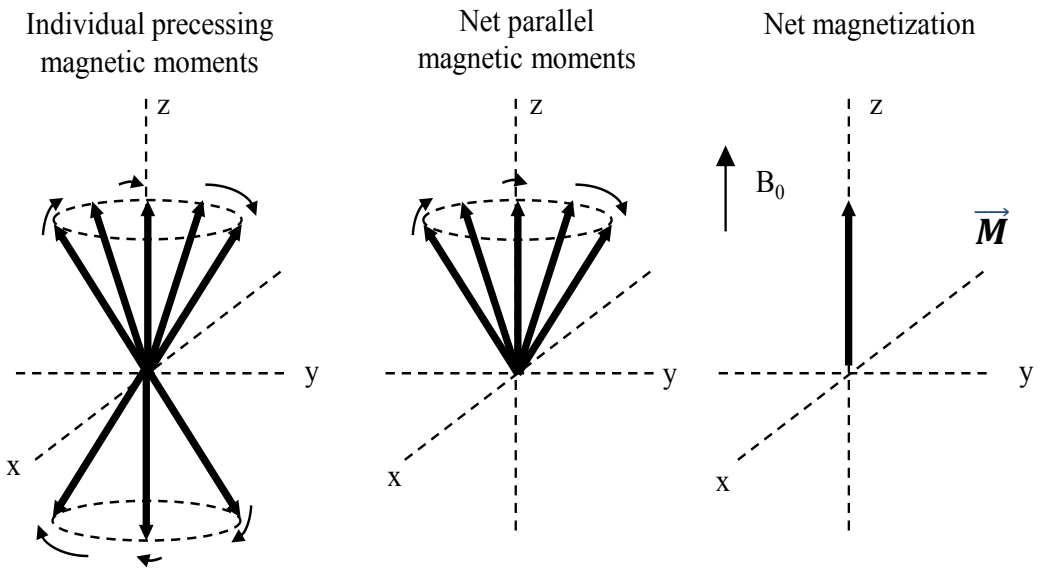

Figure 5: Left: parallel and anti-parallel individual magnetic moments precessing around z-axis. Middle: precessing magnetic moments corresponding to slightly more number aligned parallel to B_0 than antiparallel. Right: The net magnetization vector which has no component in x-y plane. Taken from [1].

Despite a net non-zero magnetization in the $\hat{z}$ direction, it is not detectable. To detect this magnetization, it needs to be rotated into the transverse plane where it can induce a current in an RF coil. Therefore, the net magnetization in the $\hat{z}$ direction should be rotated into the x-y plane, through application of a second magnetic field, typically referred to as the B_1 field (B_1 is dynamic and also has a significantly smaller strength than B_0). As with B_0, B_1 induces a torque on **M** and rotates it into the transverse plane. To interact correctly with target protons, the B_1 field needs to oscillate precisely at the Larmor frequency (which is the resonance frequency). Practically, while B_1 is applied, the net magnetization, **M**, and consequently the cone of magnetic moments, slowly precess about the B_1 field, causing it to tip away from the $\hat{z}$ direction. The angle α, through which the net magnetization rotates around B_1 field, is called the tip angle and is proportional to magnitude of B_1 and its duration τ_{B_1}, as expressed by the following equation:

$$\alpha = \gamma B_1 \tau_{B_1} \quad (5)$$

Figure 6 demonstrates how application of a 90 degree B_1 field on the cone of magnetic moments rotates the cone around x axis towards the y axis. It should be mentioned that during application of the B_1 field, magnetic moments simultaneously precess around both the B_0 and B_1 fields causing the net magnetization vector, M, to travel along a helical path during application of B_1 field in the laboratory frame (Figure 7).

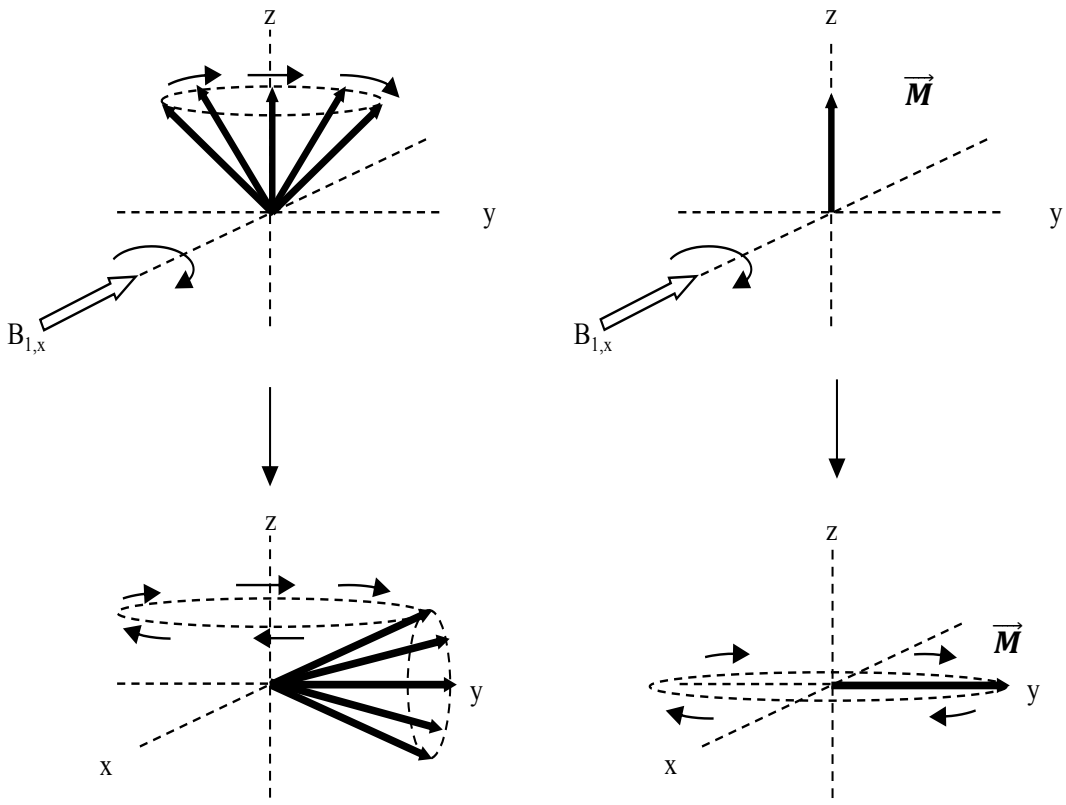

Figure 6: Top left: effect of B_1 field in the $\hat{x}$ direction on magnetic moments. Bottom left: after applying B1 for a specific duration,the cone of magnetic moments is tiped by 90 degrees towards the transverse plane. Top and bottom right: In the rotating frame, the net magnitization is tipped by 90 degrees into the transverse plane. Taken from [1].

Since the B_1 field is applied for a short time with frequency in the radiofrequency range, it is usually referred to as an RF pulse. For example a RF pulse which tips the net magnetization entirely into the transverse plane is called a 90^o RF pulse. A tip angle of 90^o leads to maximum net magnetization in transverse plane, whereas a 180^o pulse leads to no transverse magnetization, moving the longitudinal magnetization from $+\hat{z}$ to $-\hat{z}$ direction.

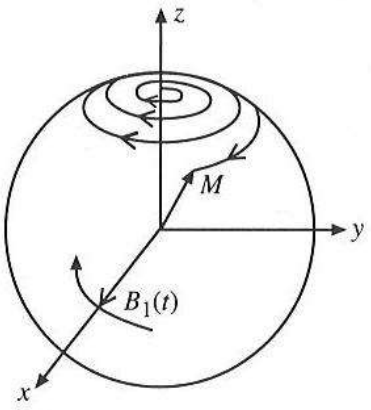

Figure 7: Helical path of the net magnetization vector in the laboratory frame from z axis toward x-y plane because of simultaneous precession around B_0 and B_1 magnetic fields. Taken from [2].

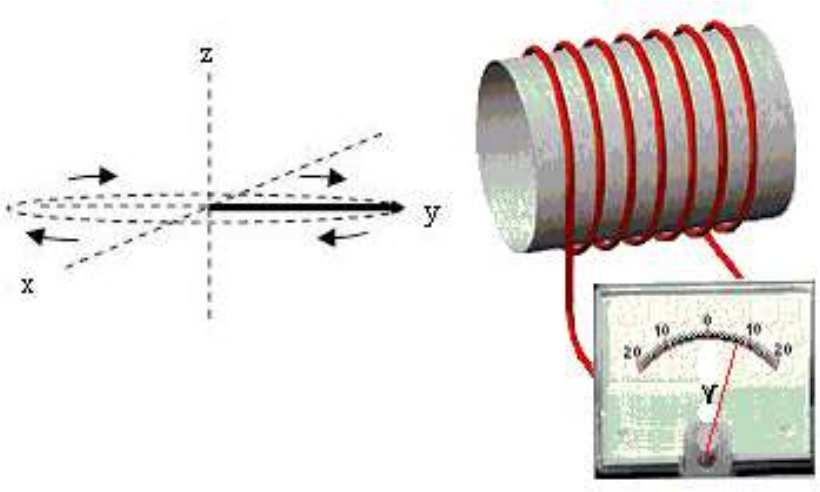

Figure 8: Installation of receiver RF coil close to imaging tissue to detect time varing signal.

1.4. Signal detection

Based on Faraday's law, a time varying magnetic field produces current in a loop of wire enclosed by the magnetic field. As shown in Figure 6 (d), after the net magnetization has been tipped into the transverse plane, it precesses about the z-axis inducing current in a loop of wire. The induced voltage is proportional to negative time derivative of magnetic flux:

$$\mathrm{V(t)} = -\frac{\partial \Phi_\mathrm{t}}{\partial \mathrm{t}} \tag{6}$$

$$\Phi_\mathrm{t} = \iint_{\mathrm{coil}} \mathrm{B(t).\,dS} \tag{7}$$

where B(t) is the actual magnetic field at coil location. To obtain a stronger signal, a coil is positioned as close as possible to the object that is being imaged. Figure 8 shows how a rotating magnetic moment induces current in an RF coil.

As mentioned, an RF pulse is used to tip the net magnetization into the transverse plane. The RF pulse is applied via a transmit coil which needs to transmit energy precisely equal to $E = h\omega_0/2\pi$ to protons in order for them to change between parallel and antiparallel energy spin states. In the macroscopic view, this energy state transition causes M_z to decrease from its equilibrium value of M_0, and the transverse component of magnetization to become nonzero. However, this transition is temporary and following a short time after the B_1 field has been turned off, the spin populations will return to equilibrium. Bloch equations govern time evolutions of M_x, M_y and M_z through time:

$$\begin{aligned} \frac{dM_x}{dt} &= \gamma\, M_y \left(B_0 - \frac{\omega}{\gamma}\right) - \frac{M_x}{T_2} \\ \frac{dM_y}{dt} &= \gamma\, M_z B_1 - \gamma\, M_x \left(B_0 - \frac{\omega}{\gamma}\right) - \frac{M_y}{T_2} \end{aligned} \tag{8}$$

$$\frac{dM_z}{dt} = -\gamma M_y B_1 - \frac{M_z - M_0}{T_1}$$

As an example in utility of the Bloch equations, assume an RF pulse is applied along the x axis and subsequently turned off. The temporal evolution of the transverse and longitudinal magnetization may then be found from solution of the Bloch equations:

$$M_z(t) = M_0 \cos\alpha + (M_0 - M_0 \cos\alpha)(1 - e^{-t/T_1}) \quad (9)$$

$$M_y(t) = M_0 \sin\alpha \, e^{-t/T_2}$$

The longitudinal component of magnetization relaxes back from $M_0 \cos\alpha$ to M_0, its equilibrium value just before excitation, with a characteristic time typically referred to as the longitudinal

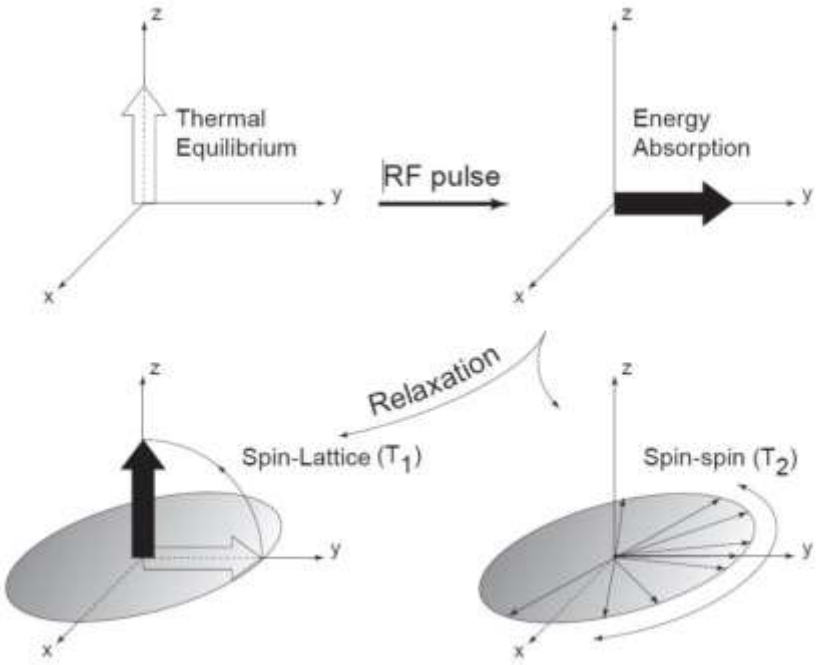

Figure 9: Schematic of two relaxation phenomena after application of an RF pulse, leading the distribution of spin populations to return to equilibrium. Taken from [3].

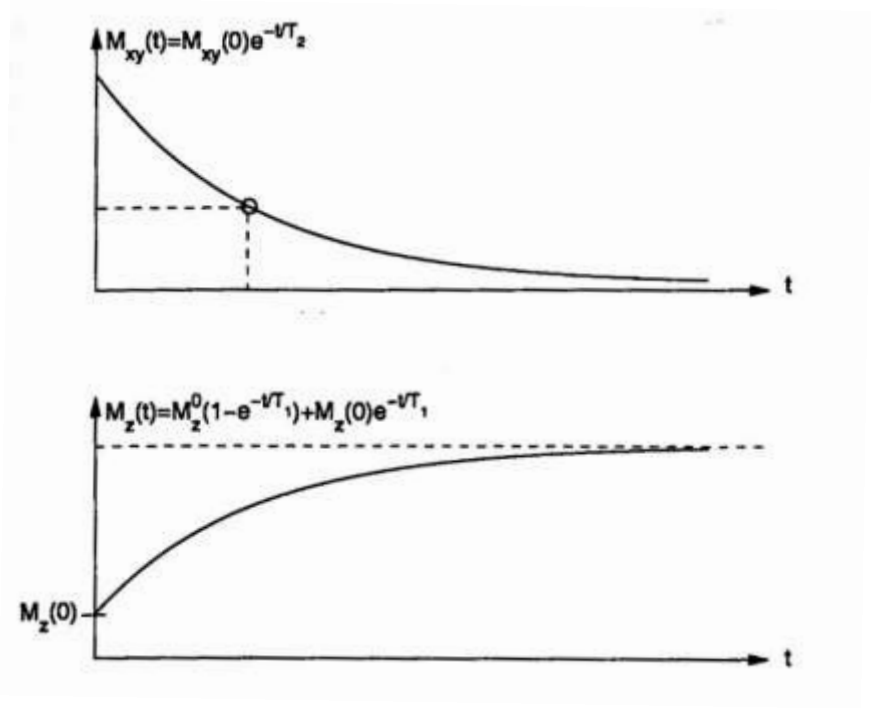

Figure 10: Top: T2 spin-spin relaxation depicts exponential decay of transverse magnetization with characteristic time T2. Bottom: Spin-Lattice (longitudinal) relaxation depicts recovery of longitudinal magnetization with characteristic time T1. Taken from [1].

relaxation time, T_1. This happens as a result of spin-lattice relaxation, which involves the spins losing their energy to the surrounding lattice and switching energy level from anti-parallel to parallel.

T_2 (transverse relaxation) on the other hand is the characteristic time decay for spin-spin relaxation causing transverse magnetization to decay to zero through loss of phase coherence between the spins precessing in the transverse plane. Figure 9 shows both relaxation phenomena after application of an RF pulse.

Figure 10 illustrates spin-lattice and spin-spin relaxations after an arbitrary tip angle. It should be noted that different tissues have different values of T_1 and T_2 relaxation times – this is the primary source of the exquisite tissue contrast in MR. Table 2 shows T_1 and T_2 relaxation times for tissues at 1.5 tesla.

Table 2: Tissues T_1 and T_2 relaxation times at 1.5 T

Tissue	T_1(ms)	T_2(ms)
Fat	260	80
Muscle	870	45
Gray matter	900	100
White matter	780	90
Liver	500	40
Cerebrospinal fluid	2400	160
Blood	1350	200
Myocardium	950	50

1.5. Magnetic Resonance Imaging

Without spatial encoding, the detected NMR signal is the sum of the all individual signals from each proton. Indeed, based on machinery described thus far, it is not possible to distinguish between the signals from different spatial locations. In 1973, Paul Lauterbur realized that imposing magnetic field gradients on top of the B_0 field will produce a range of proton resonance frequencies, each dependent on the position of the particular spin; introduction of magnetic field gradients therefore provides the means for localization of signal in the detected NMR signal. Three separate gradient coils are required for encoding the three spatial dimensions and for performing tomographic imaging. Figure 11 shows arrangement of three separate gradient coils which are physically located inside the bore of the MRI scanner. The purpose of each gradient coils is to add or subtract a time and spatially dependent magnetic field to the static magnetic field.

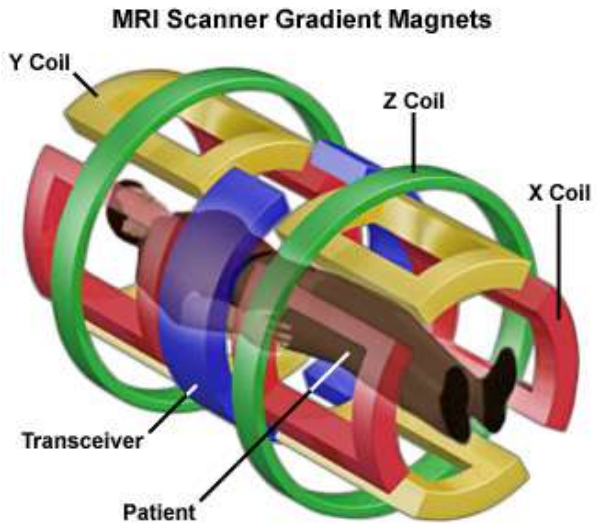

Figure 11: Arrangment of 3 gradient coils and transceiver (transmit/receive) body coil inside the scanner. These gradient fields are switched on and off, generating spatially dependent magnetic fields and Larmor frequencies. Taken from [http://www.magnet.fsu.edu].

Therefore by applying gradient fields G_x, G_y and G_z in X, Y, and Z directions, respectively, each spin experiences a unique magnetic field according to its location as shown in the following expression:

$$\boldsymbol{B} = \boldsymbol{B}_0 + \overrightarrow{\boldsymbol{G}_r}.\vec{\boldsymbol{r}} \tag{10}$$

$$\overrightarrow{\boldsymbol{G}_r} = (Gx, Gy, Gz), \qquad \vec{\boldsymbol{r}} = (x, y, z)$$

where $\vec{\boldsymbol{r}}$ is location vector inside the scanner and G_x, G_y and G_z are spatial derivative of the magnetic field in x, y and z directions, respectively (each a constant).

$$G_x = \frac{\partial B}{\partial x}, G_y = \frac{\partial B}{\partial y}, G_z = \frac{\partial B}{\partial z} \tag{11}$$

Three spatial dimensions are encoded into the MR signal through slice select, phase encoding, and frequency encoding gradients respectively. Note that these gradients are arrived at through a combination of x, y, and z gradients.

1.5.1. Slice Selection

Reliable and effective clinical diagnoses require sufficient spatial coverage of an organ through a series of parallel imaged slices at a specific orientation. This is achieved by using a frequency selective RF pulse applied simultaneously with a magnetic field gradient. The spatial location and orientation of the imaged slice in that case is the one whose spins experience a constant magnetic field:

$$\boldsymbol{B} = \boldsymbol{B}_0 + \overrightarrow{\boldsymbol{G}_r}.\vec{\boldsymbol{r}} = C_1 \tag{12}$$

where C_1 is a constant. And, since $\boldsymbol{B}_0$ is a constant,

$$\overrightarrow{\boldsymbol{G}_r}.\vec{\boldsymbol{r}} = C_2 \tag{13}$$

It can immediately be concluded that equations (12) (and (13)) is the equation of a plane with normal vector $\overrightarrow{\boldsymbol{G}_r}$ and with distance from the origin related to C_2. This implies that by choosing the proper $\overrightarrow{\boldsymbol{G}_r}$ we can determine the specific orientation for an imaged slice and since $\overrightarrow{\boldsymbol{G}_r}$ can be arbitrary, the imaged slice can have an arbitrary orientation. Figure 12 illustrates the orientation of an imaging slice with normal $\overrightarrow{\boldsymbol{G}_r}$.

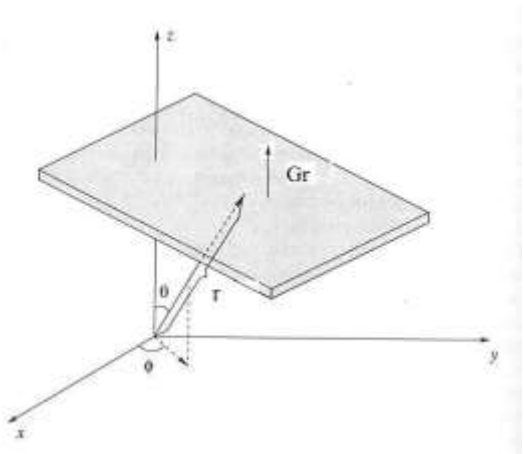

Figure 12: Orientation of an imaging slice based on $\overrightarrow{G_r}$. Taken from [2].

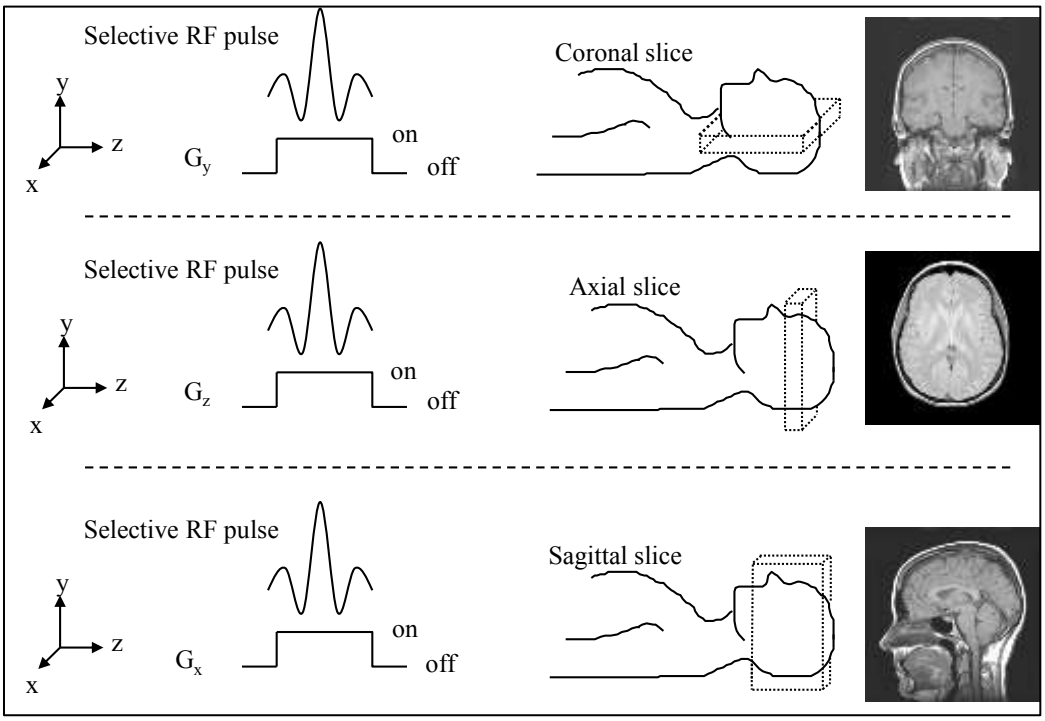

Figure 13: Schematic of the 3 most popular slice orientations in MRI arrived at by applying frequency selective RF pulses in y, z and x directions (top, middle and bottom respectively) corresponding to coronal, axial, and sagittal orientations in the brain. Taken from [1].

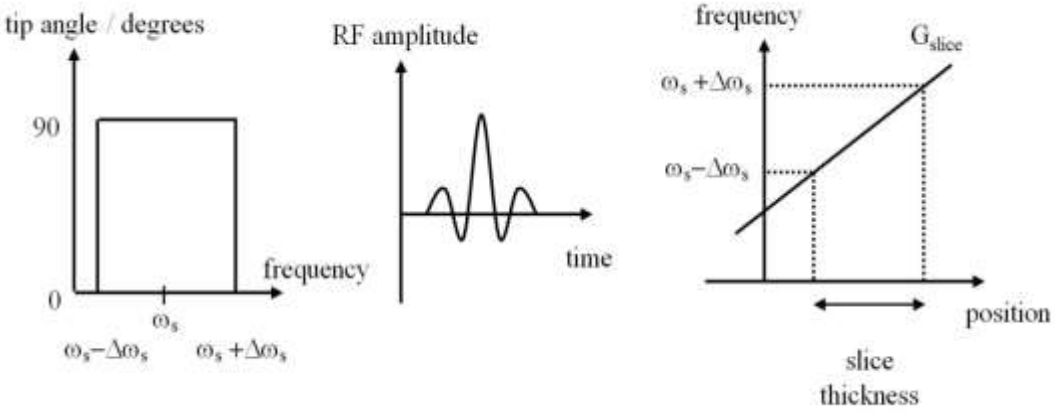

Figure 14: (Left) RF pulse in frequency domain affects spins precessing at frequency $[\omega_s - \Delta\omega_s\,,\ \omega_s + \Delta\omega_s]$. (Center) typical RF pulse in time domain. (Right) The relationship between bandwidth of RF pulse and thickness of imaging slice. Taken from [1].

In particular, axial orientations result from (G_y=G_x=0), sagittal from (G_y=G_z=0) and coronal from (G_x=G_z=0). Figure 13 illustrates these three specific imaging scenarios.

Slice thickness is determined by the bandwidth and strength of the RF pulse through equation (14):

$$\text{Slice Thickness} = \frac{2\Delta\omega_s}{\gamma\, G_{slice}} \tag{14}$$

where ω_s is the central frequency of the RF excitation pulse with a strength of $G_{slice} = \sqrt{Gx^2 + Gy^2 + Gz^2}$ and bandwidth of $2\Delta\omega_s$. Figure 14 demonstrates a frequency selective RF pulse in frequency and time domain to determine a specific slice position and slice thickness. In order to simplify the argument, let us assume that the slice select gradient is on only in the Z direction. By applying the slice select gradient and an RF pulse of a specific center frequency and bandwidth, before the transverse magnetization has completely decayed, the NMR signal becomes limited to a specific slice along the z direction. It is convenient therefore to model the acquired signal mathematically as

$$S \propto \iint_{2D\ Slice} \rho(x,y)dx\,dy \tag{15}$$

where $\rho(x,y)$ is the so-called proton density, i.e., the density of spins at a specific point (x, y).

As discussed earlier, image formation in MRI also requires in-plane spatial encoding; as there is a need to spatially resolve the MR signal from specific tissue locations. The next sections will introduce two additional gradient encodings which permit spatial encoding in the in-plane directions – these two directions are typically referred to as the frequency-encoding and the phase-encoding directions.

1.5.2. Phase Encoding

Phase encoding is performed by turning on the phase encoding gradient G_{phase} *before* signal acquisition. There are N_p different values for phase encoding gradient. Each one corresponds to one horizontal line of data acquisition matrix. Assuming the direction of G_{phase} to be y, turning on the phase encoding gradient results in spatial dependence of the spins' frequency of precession on its y coordinate

$$\omega_y = \gamma . G_y . y \tag{16}$$

where γ is gyromagnetic ratio. The phase encoding gradient is left on only for a short period before signal acquisition. Therefore, after turning off the phase encoding gradient, all spins will accumulate a y-dependent phase as predicted by equation (17):

$$\Phi \left(G_y, \tau_{pe}\right) = \omega_y . \tau_{pe} = \gamma . G_y . y . \tau_{pe} \tag{17}$$

where in (17), τ_{pe} is the length of time that the phase encoding gradient remained on. Therefore, subsequent to application of the phase encoding gradient, the signal equation (equation (15)) needs to be revised as

$$S\left(G_y, \tau_{pe}\right) \propto \iint_{2D\ Slice} \rho(x,y)\, e^{-j\,\gamma\, G_y\, y\, \tau_{pe}}\, dx\, dy \tag{18}$$

In summary, with the spatial encodings described so far, each horizontal line of data from a tissue slice with a specific y coordinate is uniquely identifiable in the acquired signal.

1.5.3. Frequency Encoding

In addition to phase encoding, frequency encoding is performed by turning on a second gradient, $G_{freq,}$ *during* signal acquisition. This gradient is perpendicular to the direction of both G_{slice} and G_{phase}. Assuming x is the direction for G_{freq}, during application of G_{freq},

spins precess at a slightly different frequency relative to their original angular velocity (or equivalently their precessional frequency) according to their location along the x axis:

$$\omega\,(G_x, x) \;=\; \gamma . G_x . x . t \tag{19}$$

Considering the effect of the frequency encoding gradient, the horizontal locations of spins are uniquely encoded in the acquired signal as follow

$$S(G_x, t) \;\propto\; \iint_{2D\ Slice} \rho(x,y)\, e^{-j\,\gamma\, G_x\, x\, t}\, dx\, dy \tag{20}$$

Subsequent to application of both the phase the frequency encoding gradients, the acquired signal encodes information about the strength of the signal originating at location (x,y) in the imaged tissue slice :

$$S\big(G_y, \tau_{pe}, G_x, t\big) \;\propto\; \iint_{2D\ Slice} \rho(x,y)\, e^{-j\,\gamma\, G_x\, x\, t}\, e^{-j\,\gamma\, G_y\, y\, \tau_{pe}}\, dx\, dy \tag{21}$$

$$\propto \iint_{2D\ Slice} \rho(x,y)\, e^{-j\,\gamma\,(\,G_x\, x\, t\,+\,\,G_y\, y\, \tau_{pe})}\quad dx\, dy$$

During application of the frequency encoding gradient, data are acquired in N_r successive points which are determined by data bandwidth in frequency domain. The timing diagram showing the specific time for application of the RF pulse, the slice select gradient, and the phase and frequency encoding gradients is demonstrated in Figure 15 – this type of a diagram is typically referred to as a pulse sequence diagram. This sequence is repeated N_p times with different values for the magnitude of the phase encoding gradient, this acquiring N_p lines in the data acquisition matrix.

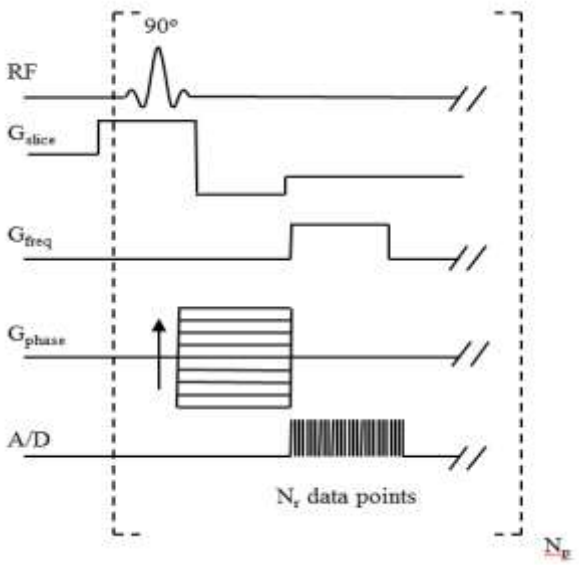

Figure 15: A pulse sequence which collects MRI data includes application of phase encoding and frequency encoding gradients. Phase encoding gradient has Np different values to construct a two dimensional dataset of size of Nr*Np. Note that this sequence does not acquire negative frequencies. Taken from [1].

From Equation (21), it should be evident that the data are collected in the spatial frequency domain, though they themselves are time signals. To explain how exactly these time signals transform into an image, two new frequency parameters are introduced as shown in Equations (22) and (23):

$$k_x = \frac{\gamma}{2\pi} G_x t \tag{22}$$

$$k_y = \frac{\gamma}{2\pi} G_y \tau_{pe} \tag{23}$$

where k_x and k_y are two spatial frequency parameters in x and y directions respectively – a back of the envelope calculation will show that k_x and k_y indeed have the correct spatial frequency units of cm^{-1}. Therefore Equation (21) can be written as:

$$S(G_y, \tau_{pe}, G_x, t) \propto \iint \rho(x,y)\, e^{-j\,2\pi\, k_x\, x}\, e^{-j\,2\pi\, k_y\, y}\, dx\, dy$$

$$\propto \iint \rho(x,y)\, e^{-j2\pi\,(k_x x + k_y y)}\, dx\, dy \tag{24}$$

The right hand side of equation (24) is the 2D Fourier Transform of the proton density, $\rho(x, y)$. Therefore the MR image of the 2D tissue slice may be obtained by taking the 2D inverse Fourier Transform of the acquired signal

$$S(G_y, \tau_{pe}, G_x, t) \xrightarrow{\text{Inverse Fourier Transform}} \rho(x, y) \tag{25}$$

1.6. K-space data structure

Two dimensional k-space representations for MRI was introduced by Twieg and Ljunggren [4] in order to better understand the MRI data acquisition process. As demonstrated in Figure 15, after the phase encoding gradient is turned off, frequency encoding gradient is turned on while data is read off, successively reading N_r data points. Subsequently, horizontal lines are collected in an identical way, though with a different amplitude for the phase encoding gradient. Figure 16 demonstrates the sampling structure of the k-space data. Line 1 of k-space data corresponds to a maximum negative value of phase encoding gradient and the last line (line N_p) corresponds to a maximum positive value of the phase encoding gradient. The time to acquire a single horizontal line in k-space is typically referred to as the repetition time or TR for short.

The spacing between k-space lines in x and y directions (Δk_x and Δk_y) are determined by dimensions of imaged object in x and y directions – the Field Of View (FOV) in MRI terminology. According to Fourier relations, FOV in the x and y directions are as follows:

$$FOV_x = \frac{1}{\Delta k_x} = \frac{2\pi}{\gamma\, G_x t_{dw}} \tag{26}$$

$$FOV_y = \frac{1}{\Delta k_y} = \frac{2\pi}{\gamma\, \Delta G_y \tau_{pe}} \tag{27}$$

where t_{dw} is the dwell time (temporal distance between two successive data points in the frequency encoding direction), and ΔG_y is the difference in value of the phase encode gradient amplitude between two successive phase encoding steps.

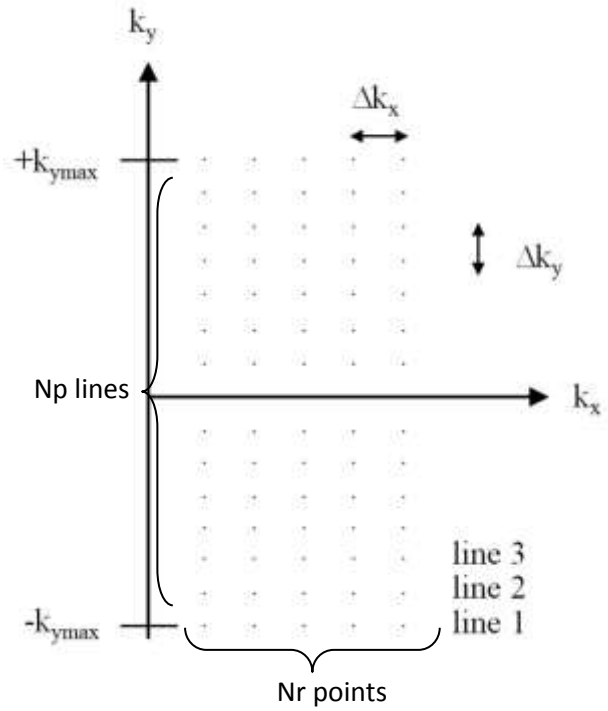

Figure 16: K-space coverage corressponding to pulse sequence in figure 15. Np horizontal lines and Nr vertical lines correspond to Np phase encoding steps and Nr data points in the read direction in figure 15 respectively. Taken from [1].

To cover the negative K_X frequencies, two methods are used in MR imaging sequences: application of an 180^o refocusing pulse in the slice select direction or application of a refocusing gradient pulse in the frequency encode direction.

1.7. Imaging Sequences

There are numerous pulse sequences in MRI, each producing a different type of contrast for different clinical application or physiological measurement. However there are two basic sequences which may be considered to be the basis for others. These are the spin echo and gradient echo sequences.

1.7.1. Spin echo

The principle behind the spin echo sequence is application of two RF pulses. The first 90^o RF pulse tips the net magnetization into the transverse plane while application of the second 180^o RF pulse a short while later refocuses the dephasing spins in the transverse plane. Both of these RF pulses are slice selective and applied while the slice select gradient (G_{slice}) is on. The time between application of the 90^o RF pulse and the center of the acquisition window is typically referred to as the echo time (T_E) while the time between application of two successive 90^o RF pulses is called the repetition time (T_R). T_E and T_R are two significant imaging parameters which can be set by the operator to create specific tissue contrast in the image (e.g., T1-weighted, T2 weighted, or a combination of these). Figure 17 demonstrates the basic spin-echo pulse sequence. The effect of the 180^o RF pulse on spin dephasing is demonstrated in Figure18.

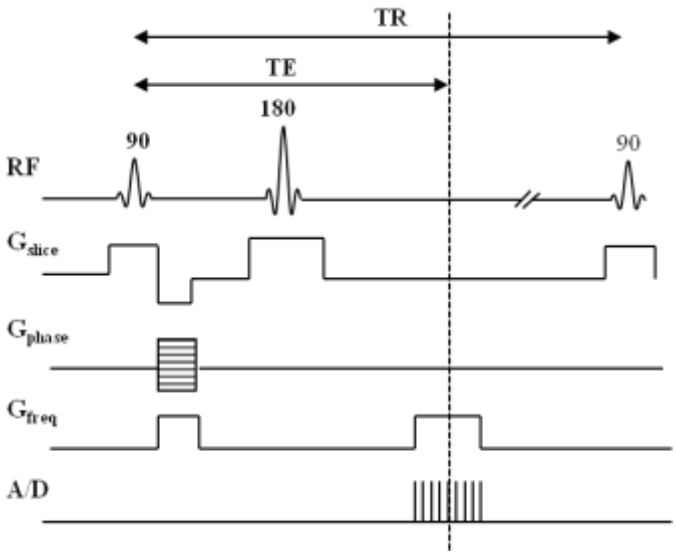

Figure 17: A spin echo pulse sequence, showing echo time (T_E) and repetition time (T_R) which may be set by the operator on the console to achieve a specific type of tissue contrast. Taken from [1].

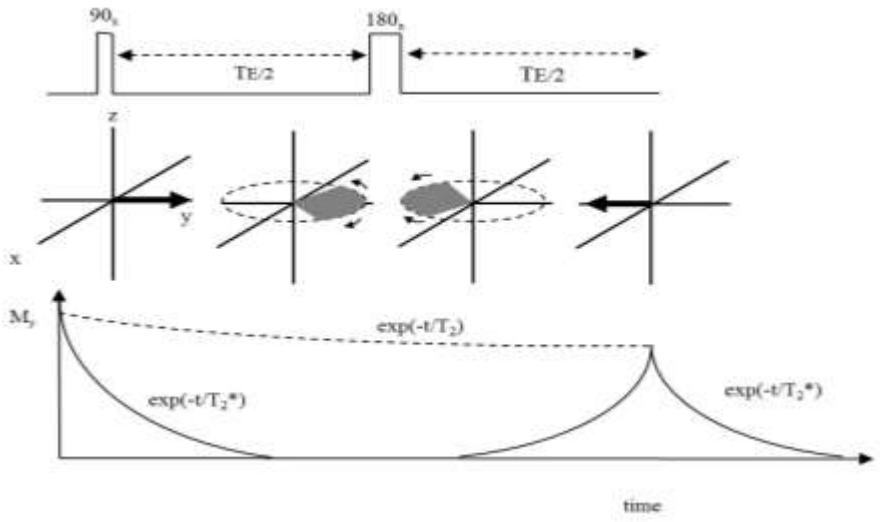

Figure 18: Effect of the spin echo sequence on the spins and the detected signal. The 90° RF pulse tips the magnetization into the transverse plane, at which time the transverse magnetization (and the NMR signal) start to decay with time constant T_2^*. The 180° RF pulse (applied at time TE/2) rephrases the spins, generating an echo at time TE. The peak of the detected signal decays with time constant T2. Taken from [1].

Spin dephasing occurs due to the static magnetic field inhomogeneities as well as differences in the magnetic susceptibility of the tissues – this causes the transverse magnetization to decay faster with characteristic time T_2^* which is shorter than T_2. The 180° RF pulse refocuses spins in the transverse plane causing the transverse magnetization to decay with T_2.

1.7.2. Gradient echo

The main difference between the gradient echo and spin echo pulse sequences is the method used to rephrase the spins in the transverse plane. With gradient echo, a gradient with negative polarity (called dephasing gradient) is applied for a short time $\tau_{dephase}$ immediately before frequency encoding (and data acquisition) starts. . Duration of $\tau_{dephase}$ is found from:

$$G_{dephase}\,\tau_{dephase} = \tau_{rephase}\,G_{rephase} = \frac{T_{acq}}{2}\,G_{rephase} \qquad (28)$$

Frequency encoding with negative polarity makes it possible to acquire a signal from the negative portion of the k-space. Figure 19 shows the gradient echo pulse sequence as well as the temporal extent of the rephrasing and dephasing gradients.

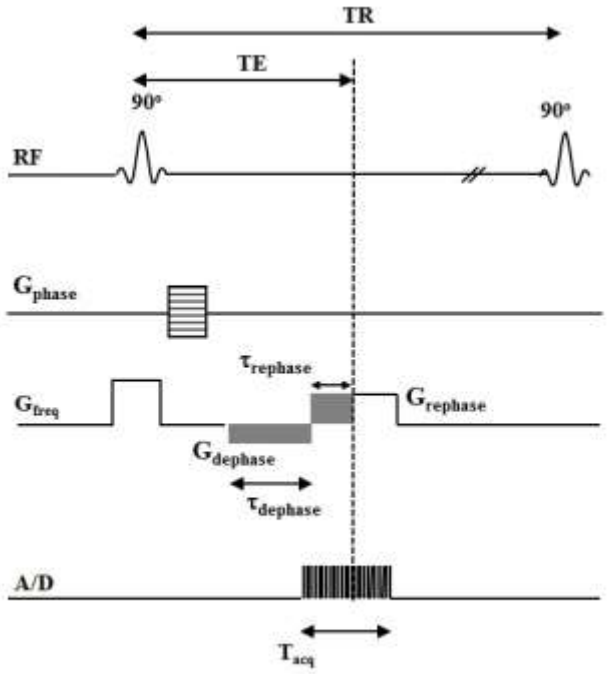

Figure 19: A basic gradient echo pulse sequence. Definition of TE and TR are the same as TE and TR in the spin echo pulse sequence. Taken from [1].

Three major type of image contrast is achievable through setting the echo time and the repetition time. Long T_R and short T_E time results in proton density-weighted image contrast. Short T_R and T_E on the other hand produce T_1-weighted contrast. Long T_R and long T_E generate T_2-weighted contrast. For any given pulse sequence all three types of contrast are achievable. Many disease states are characterized by a change of the tissue T_1 or T_2, and correspondingly, T_1 or T_2 weighted imaging is the proper method for detection of disease.

The contribution of MRI in terms of the total number of diagnostic examinations continues to increase because of its ability to perform anatomical and functional imaging.

In addition to T1, T2, and proton-density weighting, it is possible with MRI to determine motion and flow, to tag tissues and blood, and to image diffusion and other structural and functional determinants for disease diagnosis. Moreover by introducing contrast agents, it is possible to further study tissue perfusion and vascular flow with high contrast.

1.8. Cardiac MRI

MRI is a slow imaging modality, requiring several heart cycles to collect the necessary data to reconstruct cardiac images. Precisely for this reason, early cardiac images were of little diagnostic value due to severe motion blur. There were two primary challenges in cardiac MRI: a) how to freeze the motion of the heart during the cardiac cycle due to the inherent movement of the heart due to its pumping action. (b) how to freeze the motion of the heart due to the respiratory lung motion. Both of these challenges were effectively dealt with through synchronization of the data collection with physiological signals – a) the electrocardiogram and b) a physiological signal derived from the movement of the diaphragm.

1.8.1. ECG gating

The ECG is the electrical signal representing the wave of polarization and depolarization of cardiac tissue in each cardiac cycle recorded through leads placed on the subject's chest. Each cardiac cycle is started with the generation of the R-wave in the ECG signal which corresponds to ventricular depolarization and the end-diastolic phase of the cardiac cycle. Synchronization of data collection with the electrocardiogram is typically referred to as ECG gating and it requires automatic determination of the peak of the R wave. The importance of ECG gating is that it can eliminate the motion blur by acquiring data in successive R-R intervals relative to the ECG R-wave. However, ECG gating assumes that

the heart beats periodically and that the same time point in the ECG signal corresponds to the same heart position in time and space in successive beats.

In ECG gated cardiac MRI, k-space is divided into several segments and each segment is acquired in one cardiac cycle – this is the so-called segmented k-space acquisition. Figure 20 illustrates a 4-segment segmented k-space acquisition of an 8 line full k-space (typical numbers are 128 or 256 for actual in-vivo cases). Data for each segment is aquired in separate cardiac cycles and at specefic times after the ECG R-wave. For the example in Figure 20, all of the k-space data is aquired in 4 cardiac cycles: the two black lines in k-space are aquired in the first cardiac cycle, the two blue lines in the second cycle, the two red lines in the third cardiac cycle, and the two brown lines in the fourth cardiac cycle.

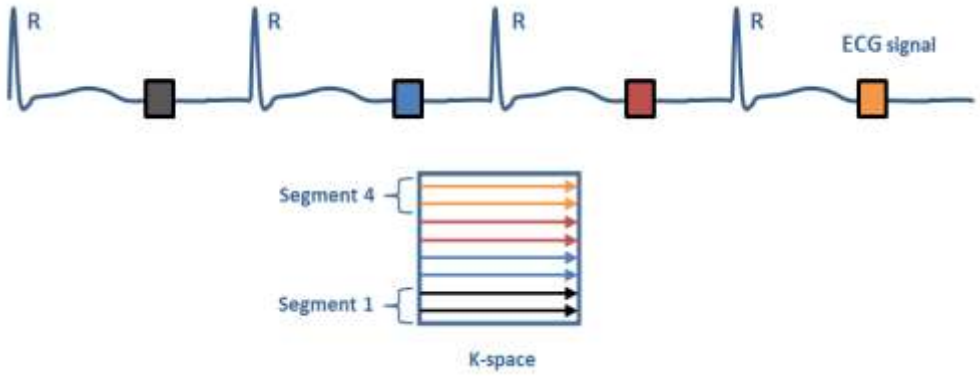

Figure 20 Schematic of ECG signal including R waves in 4 cardiac cycles and segmented k-space acquisition.

1.8.2. Cine Imaging

Cine imaging refers to the cardiac MRI technique which produces a movie (Cine) of the beating heart throughout the cardiac cycle with the cardiac cycle typically divided into 10 to 20 phases, depending on the heart rate and imaging parameters. Figure 22 shows schematic of segmented ECG-gated imaging of an 8-line full k-space Cine sequence.

Here four cardiac phases are collected, requiring two k-space acquisitions (corresponding to the same segment) for each phase. In the first cardiac cycle (first R-R interval) first segment for all cardiac phases are acquired. During second cardiac cycle, second segment of all cardiac phases are acquired and so on.

Increasing number of segments allow us to collect more images in each cardiac cycle (meaning higher temporal resolution), however with the cost of requiring more cardiac cycles to acquire the requisite k-space data to reconstruct the Cine sequence. For the example in Figure 22, it is possible to increase the number of phases from 4 to 8 in each cardiac cycle, however in that case, 8 cardiac cycle will be needed in order to collect all of the k-space data (1 k-space lines per cardiac phase per cardiac cycle). In Cine cardiac MRI, typically, 15-18 phases are sufficient to visualize the dynamics of heart motion.

The pitfalls of ECG-gating occur because of artifacts that may be encountered in the ECG signal. The artifacts may have internal or external sources. Internal sources are like muscular activity causing small spikes in ECG signal or the motion of the blood in the magnetic field generating an electric current which can distort the cardiac conduction signal (resulting from the magneto-hydrodynamic effect) and external sources can be any kind of RF or electromagnetic interference. In cases when ECG gating is not possible or is ineffective, peripheral pulse triggering can be employed using a pulse oximeter which monitors a patient's blood oxygen saturation through a sensor placed on the subject's fingertip (see figure 21). Peripheral pulsation has a time shift relative to the beginning of each cardiac cycle due to blood pulse propagation which should be considered during image acquisition.

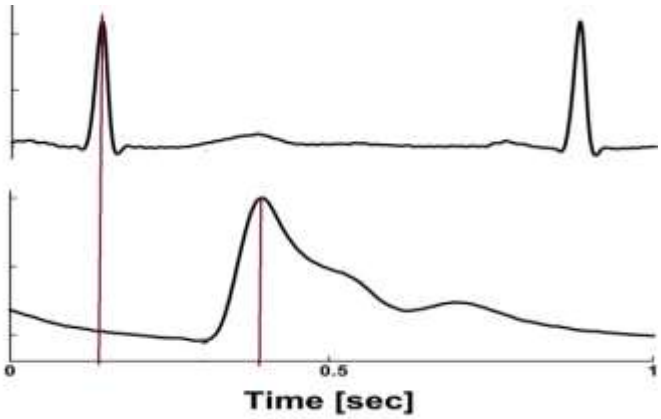

Figure 21 Demonstration of schematic ECG waveform (top) and pulse oximetry waveforms (bottom) through one cardiac cycle. Detected peak signal in pulse oximetry has a time shift relative to ECG signal. Taken from [5].

Another approach to overcoming the artifacts is to use vector cardiogram gating (VCG). The electrical axis of the heart and the MR blood flow artifact have different orientations, therefore the use of both time and space domain information inherent in VCG data would improve cardiac triggering in the MR environment. VCG is a method of using the electrical signal from the heart in 4 dimensions (x, y, z, and time) by means of a continuous series of vectors so that the interference from the magnet is reduced. VCG can distinguish electrical activity of the heart from ions in the blood permitting more accurate triggering compared to normal ECG gating.

Regardless of the issues encountered with ECG triggering, Cine imaging has been shown to be highly effective in studying cardiac function, valvular function, and in studying the blood movement through the heart for the majority of cardiac patients. The challenge in Cine imaging is the increased scan time relative to single shot imaging, during which respiratory motion of the lung may cause motion artifacts.

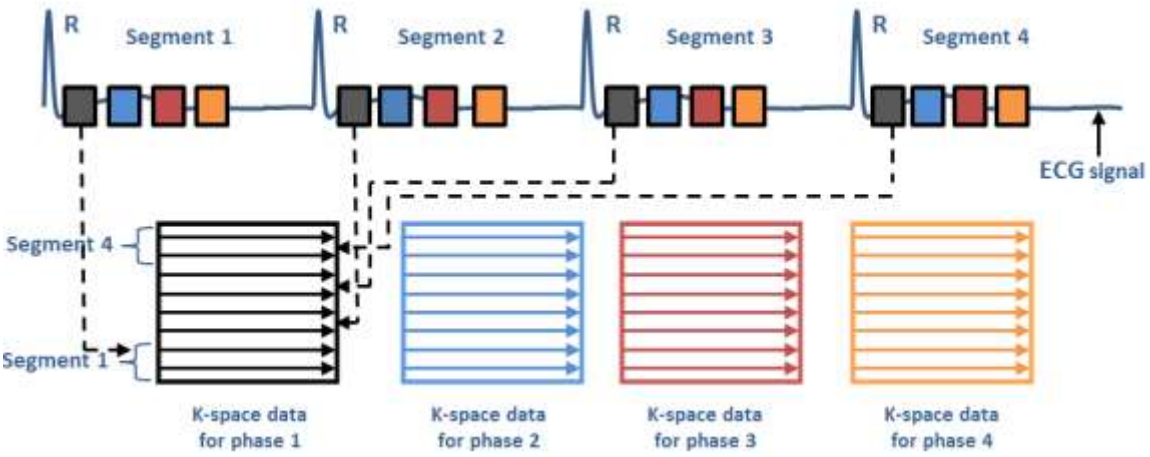

Figure 22 Schematic of ECG-gated Cine acquisition. In this figure, each color represents one cardiac phase, corresponding to one frame in a movie. To illustrate, in this figure, the k-space for each frame is divided into 4 segments and each segment data is acquired in its corresponding number R-R cycle so that segment 1 is acquired in the first cycle and segment 4 is acquired in the 4th cycle.

1.8.3 Breath-hold Imaging

The second potential source of motion artifacts in cardiac MRI arises due to movement of the lung during the respiratory cycle. Breath-held imaging is a very reliable technique for reducing the respiratory motion artifacts, but only when the subject is able to stop breathing for 10-15 seconds and when this period is sufficient to collect the requisite k-space data to reconstruct a Cine sequence. In breath-held imaging, the subject is asked to hold his/her breath for the duration of image collection. Breath-held scan require one or more manual starts and breath hold instructions from the MRI operator to the subject. It also prolongs the total scan time when compared to the predicted scan time, depending on the actual length of the pauses between successive breath holds. Longer scan times can be performed by dividing total scan time into 2-3 breath holds. However, for very long scan times (longer than 45-60 seconds), breath hold scans are no longer possible and navigator gating is required.

1.8.4 Respiratory Gating

In multi-shot free breathing cardiac MRI studies or in general in thoracic and abdominal imaging studies, respiratory motion can cause severe motion artifacts that may not be corrected for later. Although it is possible to perform breath-hold imaging when imaging a single 2-D slice, in the case of 3D or 4D imaging, it is not possible to acquire the required k-space data in a single breath-hold. Additionally, when performing multiple breath-hold imaging, it is difficult to ensure that the residual lung volume is identical in different breath-holds. For these reasons, for 3D and 4D imaging, or when the subject is unable to hold their breath, a different approach based on navigator gating is often adopted. The basis for respiratory gating with navigator echoes is cylindrical excitation of the border between the liver and the lung through application of a prepulse sequence in order to image a small area perpendicular to the lung-liver border. In the resulting images which are reconstructed in real time, the contrast between lung and liver is sufficiently high to allow straightforward detection of the border with ease. This information is used as a gating signal during acquisition of k-space data, more specifically, only k-space data that are collected when the navigator is within a certain respiratory window is accepted and is otherwise discarded and not used in image reconstruction.

Navigator measurement are synchronized to the ECG signal and reconstructed in a close to real time manner to integrate with the data acquisition. The length of navigator window can be planned to include the right hemidiaphragm [6, 7]. Navigator window should be long enough to cover the complete excursion of the diaphragm during the respiratory cycle and short enough to not include any static tissue.

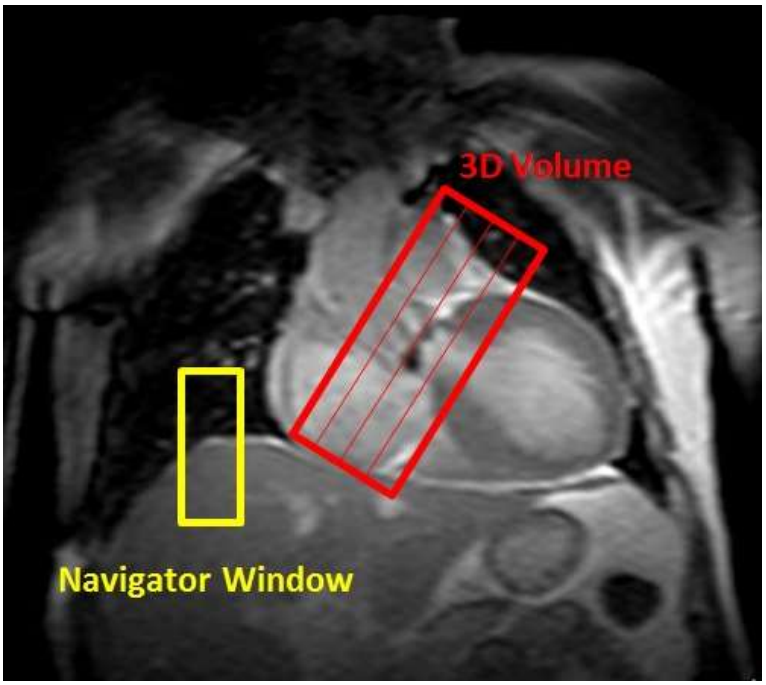

Figure 23: Set up of navigator window for a cardiac study. Navigator window (yellow box) is typically placed on the border of lung-liver.

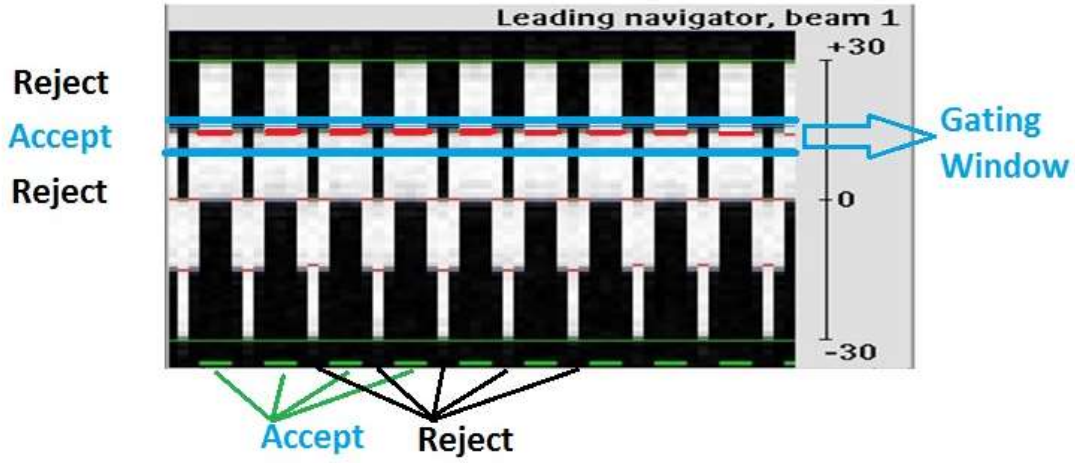

Figure 24: Schematic of navigator window which show displacement of chest-liver border in foot-head direction. Blue lines define accept window for data acquisition.

Depending on the subject's breathing pattern, a certain percentage of the acquired k-space data which fall outside of a predefined window is rejected. Typically, 50-70% of the data are rejected, needing to be acquired again. Therefore, respiratory gating can

increase the imaging time to up to 3 times or more. Figure 23 shows the navigator set up in a cardiac study to image the region around the Aortic valve in 3-D. Figure 24 shows displacement of chest-liver border in foot-head direction through time in the navigator user interface for an artificial example. Whenever the liver-chest border line falls into predefined gating window (within the two blue lines), the collected k-space data is accepted by the scanner, but otherwise is rejected.

1.9. Conclusion

The purpose of this chapter was introduction to basics of Magnetic Resonance Imaging and main challenges and artifacts encountered in imaging. Also an overview of Cardiac imaging with emphasize on motion artifact and suggested solution to mitigate them including ECG and respiratory gating was provided. The next chapter will explain motion encoding techniques, permitting velocity and flow measurement capabilities for MRI.

CHAPTER 2

MRI VELOCITY AND FLOW MEASUREMENT TECHNIQUES

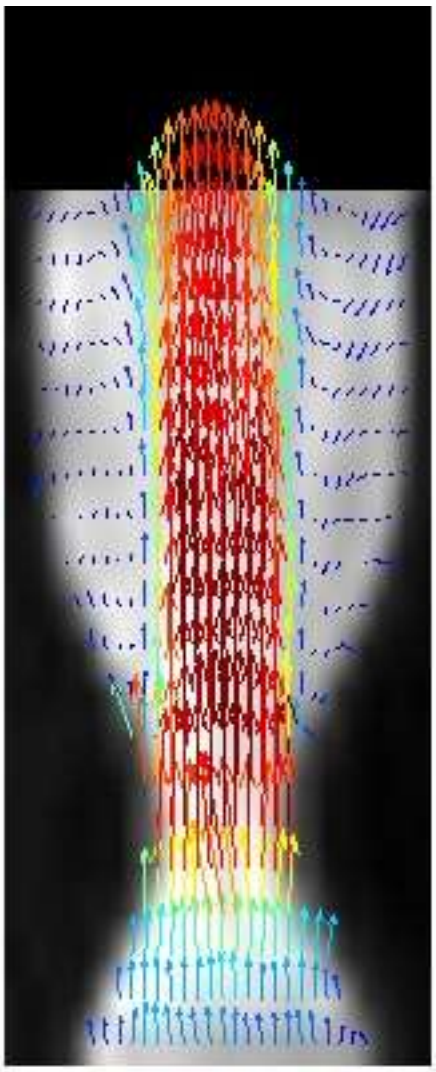

2.1. Flow Regimes

The phase of the MR signal is sensitive to motion and can be used to measure velocity and flow with the phase-contrast (PC) MRI technique. In this chapter, we will review the basic fluid mechanics of blood flow before embarking on description of PC MRI and other MRI techniques which are commonly utilized for measurement and visualization of flow in the vasculature.

2.1.1. Laminar Flow

Flowing blood is faced with frictional forces from the vessel wall and neighbor blood components in its way through the vessel, so blood flows with various velocities across the diameter of the vessel. The most known flow pattern for healthy human subjects with a constant vessel thickness is the Laminar flow regime**.** In Laminar flow, the velocity profile takes on a parabolic shape where the velocities at the center of the vessel are higher than the surrounding ones with zero velocity at the vessel wall. Figure 25 shows the Laminar flow distribution in a normal vessel.

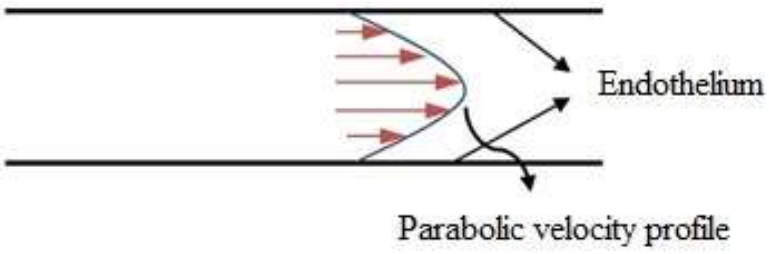

Figure 25: Laminar flow velocity distribution in a vessel.

2.1.2. Turbulent Flow

In the case of high velocity through a stenosis or vessel branches like the carotid and iliac bifurcations there is a different story here there are complex flow patterns with flow vortices and turbulent flow at and distal to the stenosis. A flow vortex is usually caused by rapid deceleration of the jet after a stenosis, or at the peripheral area of arterial bifurcations. In a vortex, there are slowly whirling flow patterns close to the vessel wall after the stenosis. Figure 26 demonstrates this flow circulation distal to the stenosis. Flow vortices and turbulent flow can cause MR signal loss (also referred to as signal dephasing) because of the protons (spins) moving in arbitrary directions. The possibility of turbulent flow is calculated by fluid's Reynolds number (Re) [8] and is defined in Equation (29).

$$Re = \frac{(\rho DV)}{\eta} \tag{29}$$

Where ρ is the fluid density, D is the vessel diameter, V is the flow velocity, and η is the fluid viscosity. Reynolds numbers (Re) less than 2000 imply laminar flow; whereas Reynolds numbers (Re) more than 2,000 imply the possibility of turbulent flow [9, 10]; Re above 1,000 and less than 2,000 results in transitional flow (i.e., not laminar but not fully turbulent).

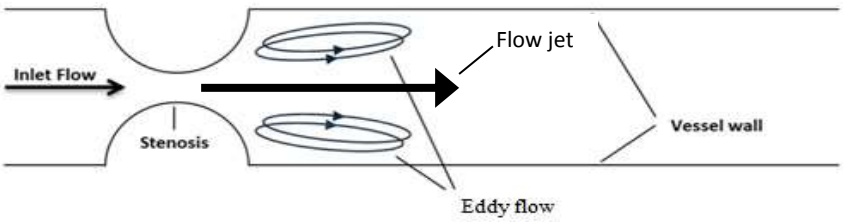

Figure 26: Vortex formation and velocity separation occurs distal to a narrowing.

2.1.3. Pulstile flow

In this case there is a complex time varying flow function. The function depends on many known and unknown parameters in the human body including vessel wall compliance and stiffness. The temporal changes in flow can lead to spatial artifacts in image reconstruction and registration. Pulstile flow is more significant in arteries than veins. Peak systolic velocity in normal subjects generally decreases with distance from the heart. Rapid changes in velocity are troublesome in velocity quantification with MR. Many fast imaging methods have been proposed to overcome artifacts due to pulsatile flow [11-13].

2.2. MR Angiography: Visualization of Vascular Anatomy

Flow visualization and quantification in-vivo is very helpful for diagnosis and monitoring of many vascular and cerebro-spinal diseases. Doppler ultrasound is currently the most widely adopted method for cardiovascular flow imaging. However existence of air, bone, or a surgical scar is a significant barrier to accurate evaluation [14, 15]. e.g., due to presence of the skull, Doppler has found limited applications to intracranial flow imaging.

Magnetic Resonance Imaging (MRI) is a unique imaging modality with superb anatomic imaging capability with excellent soft-tissue contrast that also has the capability to image functional hemodynamic such as velocity and flow. In MR flow imaging, scan time is intimately related to both spatial and temporal resolution [16] with short imaging times achievable by reducing temporal and spatial resolutions. However, low temporal resolution leads to underestimation of peak velocities while the total imaging time is

usually limited to the length of a breath-hold. On the other hand, poor spatial resolution can lead to data inconsistency, partial volume effects, and phase dispersion which can degrade the image quality and accuracy [17, 18]. Fourier Velocity Encoding is more accurate than Phase Contrast MRI in quantification of high speed and complex flows where a range of flow velocities may be present in an imaged voxel [19, 20]. This idea eliminates partial volume artifact, however, it leads to a considerably longer scan time.

In general, MR flow imaging methods can be categorized in two major groups: flow angiography and flow quantification. In flow angiography, goal is to visualize the flowing blood (or other fluids such as the cerebrospinal fluid or urine). The essential goal of Magnetic Resonance Angiography (MRA) is to portray blood vessels having high contrast with stationary tissues to provide physiological information and to evaluate them for vascular pathologies such as stenosis, aneurysm, dissection, and coarctation. Results provide valuable information about tissue perfusion and an organ's function. Methods such as black blood imaging and bright blood imaging which use the so-called TOF (time-of-flight) effect have been developed to achieve this goal [21]. Using intravenous contrast agents to shorten T_1 of blood provides brighter image of blood having higher contrast than surrounding tissues. TOF methods are explained in Section 2.2.1

Quantitative flow measurement methods provide us with a numerical tool to evaluate the amount of flow. Clearly, comparison of measured flow in a diseased vessel with the expected normal flow can be helpful in the diagnosis of patients and can help in understanding and monitoring of the disease process. Quantitative flow methods essentially are based on the accumulated phase of moving spins against stationary ones. Two major phase-based methods are the Phase Contrast MRI (PC MRI) and Fourier

Velocity Encoding (FVE) techniques [22]. These methods are explained in Sections 2.3.5 and 2.3.6.

2.2.1. Time of Flight (TOF)

Time of flight has become a very well-known method in magnetic resonance angiography (MRA). This method uses a different saturation for moving and stationary spins to make an angiographic contrast. Flow perpendicular to the imaging slice can result in fresh spins entering the slice during RF excitation pulses, causing different magnetization saturation for static vs. moving spins. Basically TOF methods can be categorized in two approaches: black blood and bright blood imaging. The first approach tries to void the signal from moving spins and decrease the related echo signal resulting brighter signal for stationary tissue against darker signal from flowing blood.

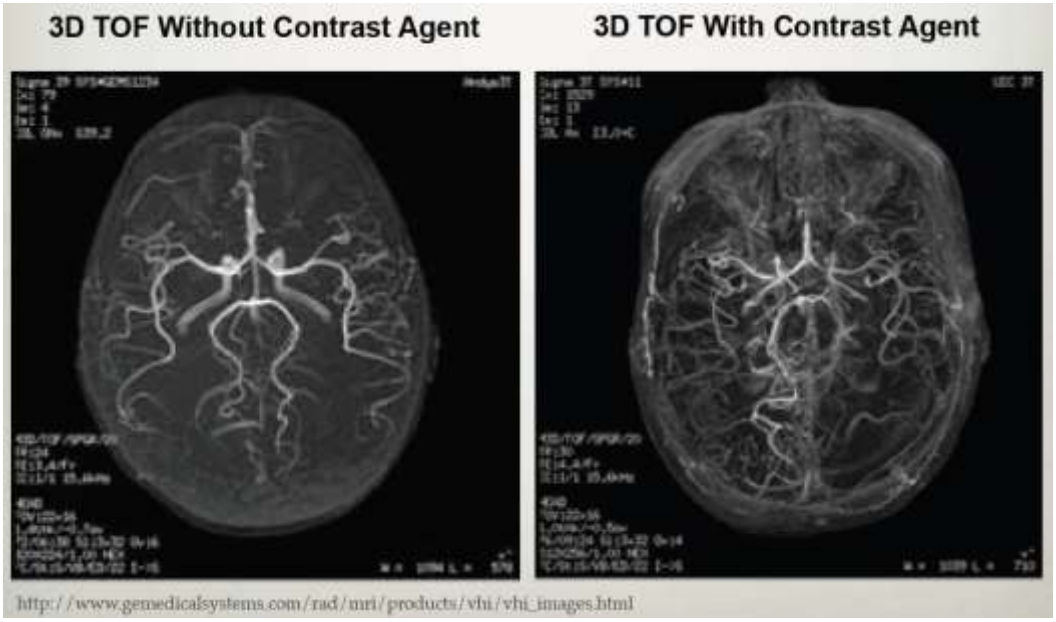

Figure 27: Application of Time of Flight in brain MRA with and without contrast agent, taken from [www.gemedicalsystem.com/rad/mri/products/vhi/vhi_images.html]

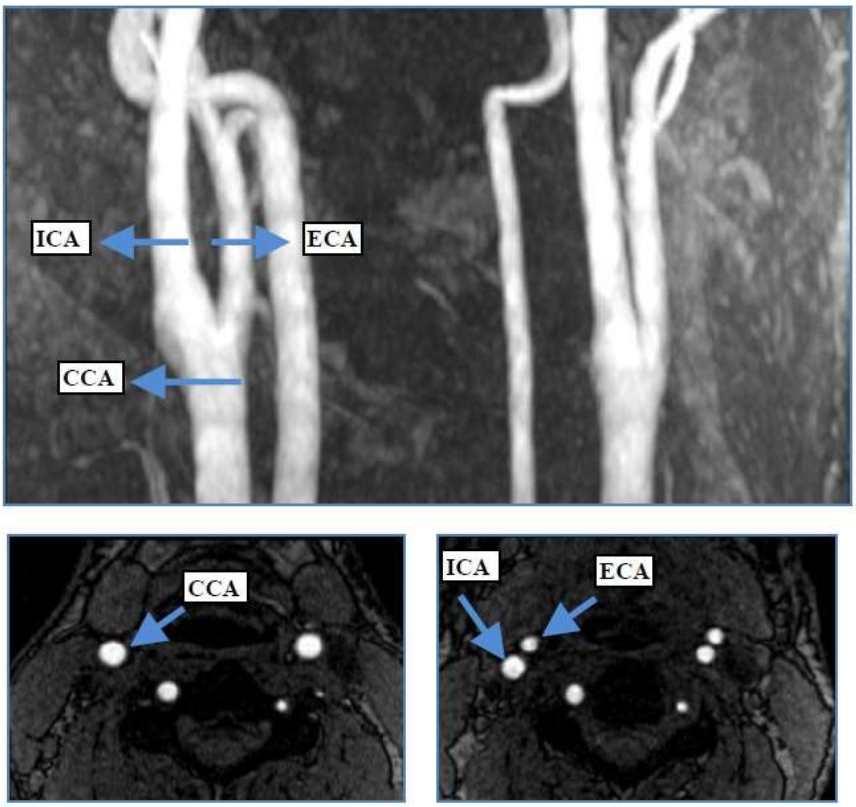

Figure 28 (Top): A maximum intensity projection (MIP) obtained from time of flight (TOF) MRI study. (Bottom): Axial magnitude images from TOF in the CCA and ICA/ECA in arrows location before bifurcation (left) and after bifurcation (right)

The second approach saturates magnetization of stationary tissues, and uses the fresh blood flowing into the slice during image acquisition to produce image contrast. In this method a brighter intensity is for blood flowing into the slice. Figure 27 demonstrates the usage of TOF effect in brain MRA. Figure 28, demonstrates carotid anatomy in volunteer. A maximum intensity projection (MIP) obtained from time of flight (TOF) MRI study is displayed on the top. Axial magnitude images from TOF in the CCA and ICA/ECA are shown in the bottom. Arrows refer to right CCA, ICA and ECA. Using of contrast agent can make small vessels clearer and brighter. Relatively long imaging time continues to be a considerable problem with TOF methods [23, 24].

2.2.1.1 Black Blood Imaging

This technique was originally developed to improve segmentation of myocardium from the blood in heart imaging. It uses a spin echo pulse sequence with 90^0 and 180^0 slice selective RF pulses. In the conventional spin echo technique, spins experience both 90^0 excitation RF pulse and 180^0 refocusing RF pulse, generating an echo and contributing to image formation.

In the TOF effect, after the initial 90^0 pulse, the fast moving, excited, flowing blood leaves the imaging slice, and in the meantime, fresh, unexcited blood enters into the imaging slice. This new fresh blood only experiences the 180^0 refocusing RF pulse and as a result does not contribute to the echo, causing a signal void for moving blood (low intensity). In contrast stationary tissues and slow moving blood, experience both 90^0 and 180^0 RF pulses leading to MR signal (high intensity). Figure 29 shows the TOF effect in black blood imaging for different velocities.

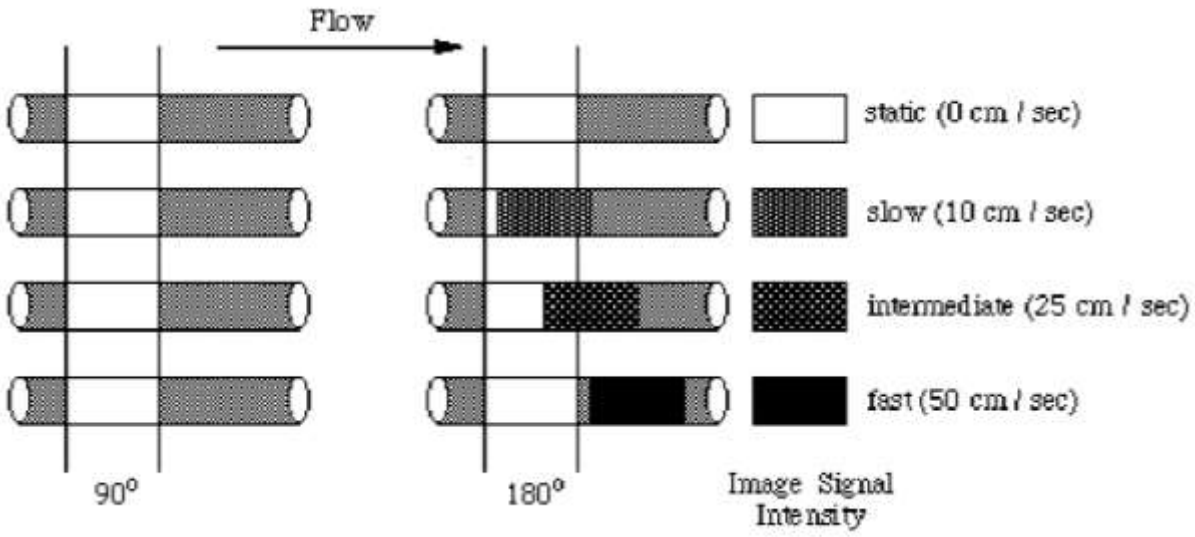

Figure 29: Effect of flowing blood on image signal intensity in Black-Blood-Imaging versus different velocities. Taken from [9].

The percentage of signal loss in black blood imaging depends on flow velocity, slice thickness, and echo time. Higher velocity and thinner slice thickness lead higher percentage of signal loss and darker pixel in the image.

2.2.1.2 Bright Blood Imaging

Bright blood imaging has become a popular tool for evaluation of ventricular function [25]. In this method we use one additional slice selective 90^0 saturation RF pulse (preparation pulse) immediately before the conventional 90^0 excitation RF pulse in the gradient echo pulse sequence. Stationary spins experiencing both saturation and excitation pulses have a weaker echo signal since the time interval between the two 90^0 RF pulses is not long enough for the longitudinal magnetization to fully recover.

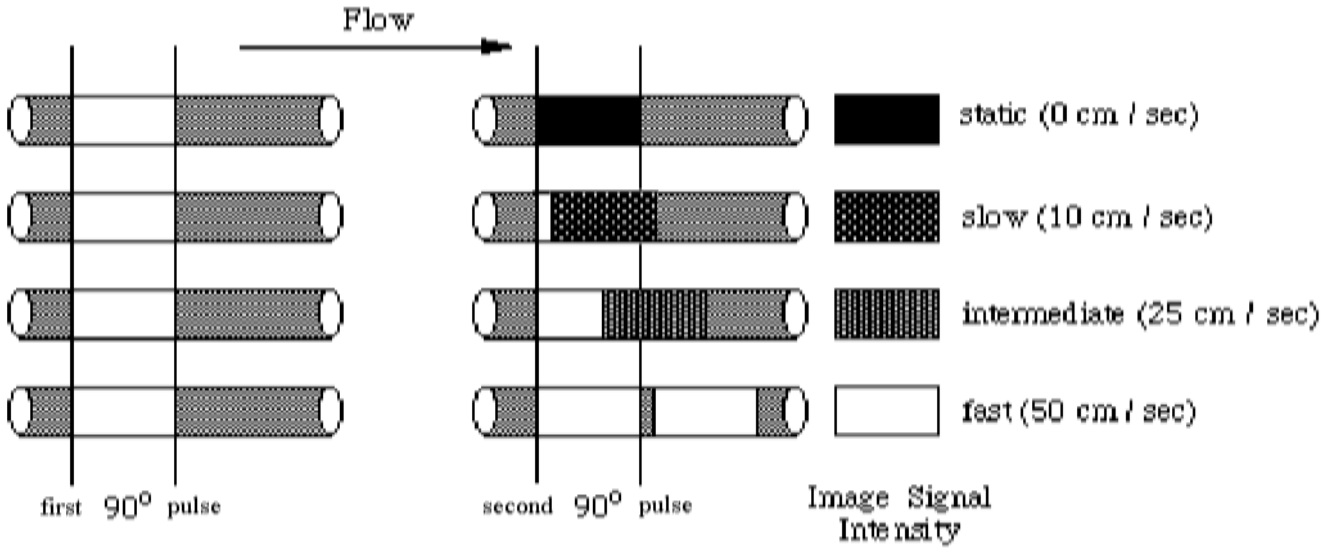

Figure 30 Effect of flowing blood on image signal intensity in Bright-Blood-Imaging verse as different velocities taken from [9]

On the other hand, unsaturated fresh spins replace saturated ones in the time interval between the two 90^0 RF pulses, These fresh spins produce higher signal intensity at echo time and generate the brighter image of blood since they do not experience the first 90^0

RF pulse. Higher velocity leads to higher signal intensity. Figure 30 shows the TOF effect in bright blood imaging for different velocities. Signal intensity can increase in the presence of higher flow velocities, thinner imaging slice, and longer time interval between the two 90^0 RF pulses.

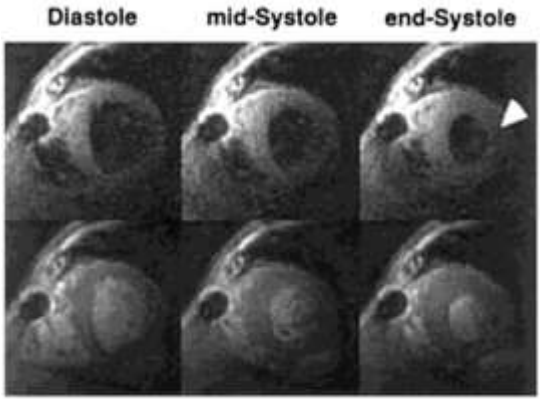

Figure 31: Black (upper row) and Bright (bottom row) blood cardiac imaging in a normal volunteer. Taken from [25].

Figure 31 shows black blood and bright blood imaging of the left ventricle in a normal volunteer during end diastole, mid-systole, and end-systole. For more recent ideas including real time TOF imaging the interested reader is referred to [21, 25].

2.3. MR Velocity and Flow Quantification Techniques

MR flow quantification methods are highly versatile and can in principle determine all three components of velocities within an image voxel. To achieve this goal, new elements in the gradient waveforms of the imaging pulse sequence are introduced. These elements make the phase of the MR signal for each pixel dependent on its velocity.

2.3.1. Bipolar Gradients

Bipolar gradients are combinations of two identical gradient pulses with opposite polarity which are added to the gradient waveform for the direction (i.e., x, y, or z) where velocity measurement is required [22]. Bipolar gradients can be applied along the phase encoding, frequency encoding, or slice select direction subsequent to the excitation. They can encode velocity of moving spins in the phase of the signal intensity. Figure 32 shows general type of bipolar gradients.

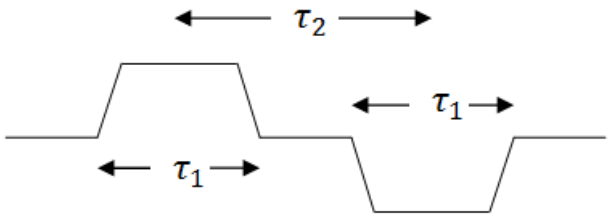

Figure 32: Trapezoid bipolar velocity encoding gradients

Based on theory of MR physics, a spin at position $\boldsymbol{r}$, will accumulate a phase shift that is equal to the time integral of the precessional frequency (equation 30)

$$\emptyset\,(r,t) = \gamma \int_o^t \boldsymbol{G}(\tau)\,.\,\boldsymbol{r}(\tau)\,d\tau \qquad (30)$$

where $G(\tau)$ is a magnetic field gradient felt by a spin, γ is a constant (the gyromagnetic ratio), and $r(\tau)$ is a location of the spin. When bipolar gradients are applied, the phase shift accumulated after the first gradient pulse will be canceled by the second pulse for the static tissue. However, if the location of the spin changes between the two gradient pulses, the phase shifts no longer cancel each other. The residual phase shift depends on

the distance that the spin has moved between the two gradient pulses and is proportional to the spin's mean velocity.

If a spin is at initial position x_0 when the first pulse of the bipolar gradient is applied and it is assumed that the position of the spin is constant during first pulse, the accumulated phase shift according to equation (30) becomes

$$\emptyset_1 = \gamma G x_0 \tau_1 \tag{31}$$

If the spin moves with constant velocity $\boldsymbol{v}$, its position when the second pulse of the bipolar gradient applied, is given by

$$x_2(t) = x_0 + v.\tau_2 \tag{32}$$

Then, the accumulated phase shift by the second pulse according to equation (30) is:

$$\emptyset_2 = -\gamma G (x_0 + v.\tau_2)\tau_1 \tag{33}$$

And the total accumulated phase shift is obtained by summation of (31) and (33)

$$\emptyset = \emptyset_1 + \emptyset_2 = -\gamma G v \tau_1 \tau_2 \tag{34}$$

The above equation shows that bipolar gradient results in a phase shift proportional to the gradient amplitude, the spin velocity, the pulse duration, and the separation time between two lobes of bipolar gradient. Figure 33 shows a bipolar gradient and its effect on static spins with different location and spin with constant velocity (it is assumed there is no gap between lobs).

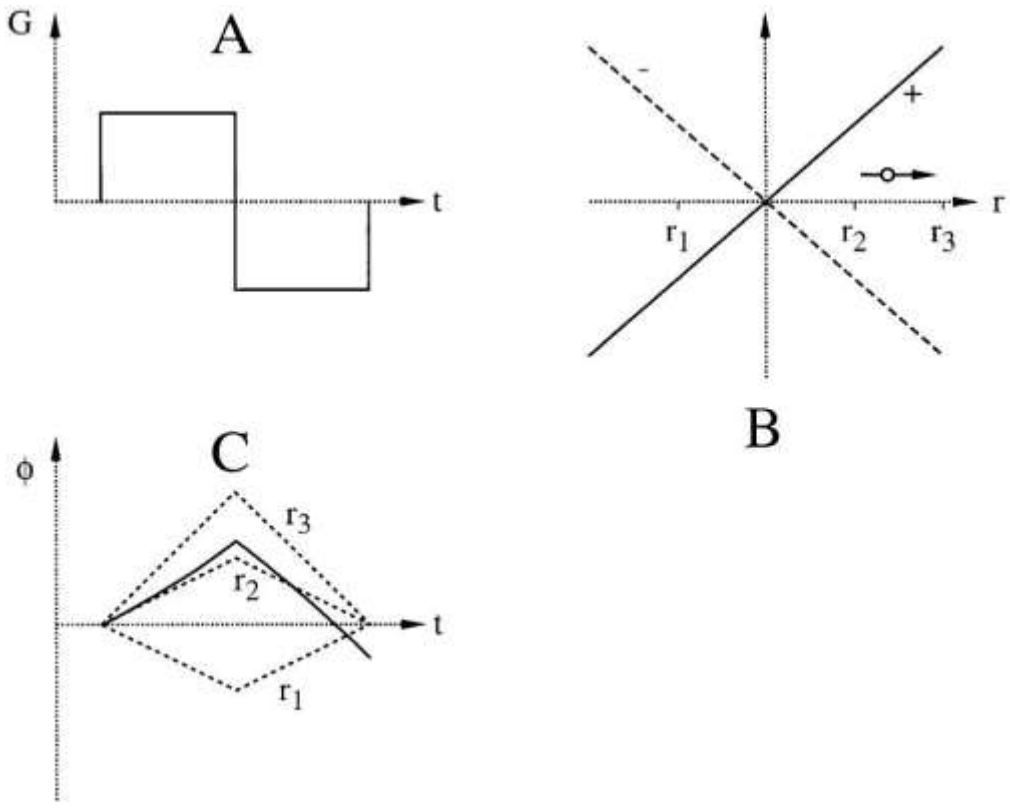

Figure 33: (A): Bipolar gradient lobe. (B): spins with different positions (r_1, r_2, r_3) (C): effect of bipolar gradient on cumulative phase of 3 static spins at different locations r_1, r_2,r_3 and a moving spin, moving from position r_2 to position r_3. Taken from [26]

2.3.2. Gradient Moment Analysis

One can get an expression for motion-induced phase shifts of any order using gradient moment analysis [27]. Using the Taylor series expansion, the position of a spin at time *t*, *x*(*t*), can be approximated as

$$x(t) \cong x_0 + \frac{\partial x(t)}{\partial t}.t + \frac{\partial^2 x(t)}{2!*\partial t^2}.t^2 + \ldots + \frac{\partial^n x(t)}{n!*\partial t^n}.t^n \quad (35)$$

By plugging in Equation (35) into Equation (30), the phase shift at time *T* is shown in Equation (36)

$$\emptyset(T) = \gamma \sum_{n=0}^{N} \frac{\partial^n x(t)}{n! * \partial t^n}.M_n(T) \quad (36)$$

Where $M_n(T)$ is the gradient moment of order n for the gradient pulse $G(t)$, and is defined by:

$$M_n(T) = \int_0^T G(t).t^n\, dt \tag{37}$$

Nulling a particular order of gradient moment by adding extra lobes to the pulses will make an MR pulse sequence insensitive to that order of motion. For example, in MR pulse sequences that are insensitive to constant-velocity, $M_0 = 0$. With increasing order of moment nulling, the pulse sequence duration also increases and the longer the pulse sequence, the more the artifacts and the less the temporal resolution. Therefore, there is a tradeoff between pulse sequence duration and moment nulling order.

2.3.3. Phase Contrast MRI (PC-MRI)

The basis of phase contrast technique, first proposed by Hahn [28] in 1960, is that spins moving in the presence of a magnetic field gradient accumulate a different phase from stationary ones. The first application of this method was developed by Moran [22], and subsequently applied in human cases by Van Dijk [29].

The drawback of the PC technique is that the phase can be affected by many undesirable factors like magnetic field in-homogeneity, pulse sequence tuning, acceleration, partial volume artifact, and eddy current (these artifacts are explained in detail Sections 2.3.7 and 2.3.8). Numerous papers have been published on how to correct and compensate for the undesirable factors noted above. To remove signal from static tissue and constant noise, it is suggested to use two different sequences with identical zero moments, and different first moment and subtract them. Figure 34 shows a reference and a velocity encoded scan, and the result of phase map subtraction, yielding the velocity map.

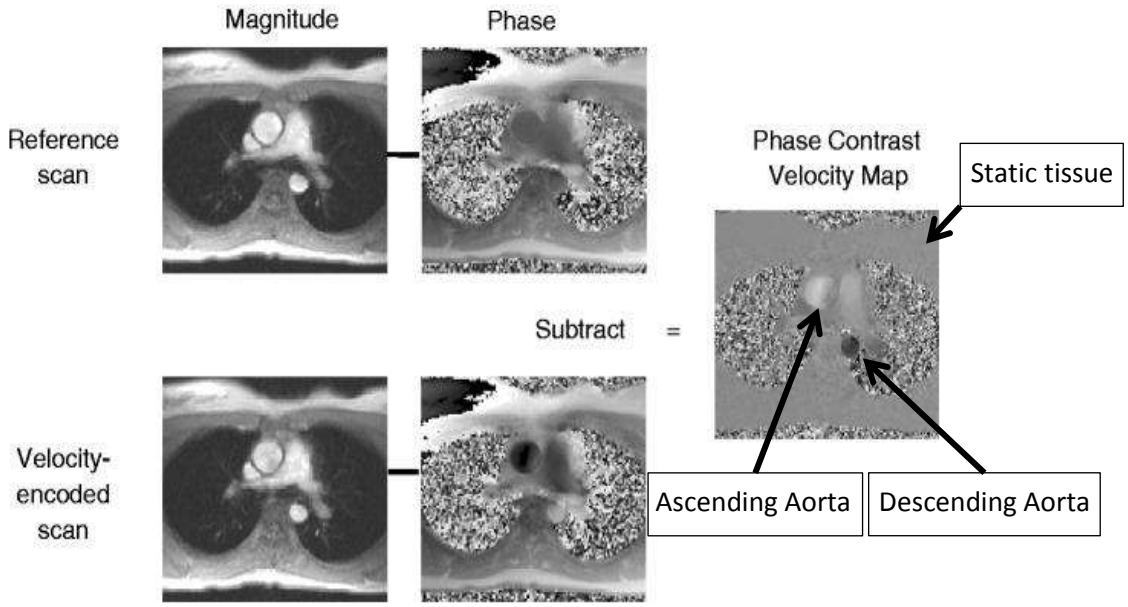

Figure 34: In PC MRI, the magnitude and phase images are reconstructed from the reference scan (top row) and also from the velocity encoded scan (bottom row). The corresponding phase images are subtracted resulting in the PC velocity image. Taken from [30].

2.3.4. Velocity Encoding (V_{enc}) Value

According to the gradient moment analysis, a zero o^{th}order gradient moment and a non-zero 1^{st}order gradient moment are needed for velocity encoding in Phase Contrast imaging. The phase-shift due to motion in that case is given by:

$$\emptyset = \gamma v M_1 \tag{38}$$

$$\Delta\emptyset = v\,(\gamma\,\Delta M_1) \tag{39}$$

Hence, velocity measurements are obtained from the phase values of the acquired images. Note that we are assuming that acceleration and higher order motion terms are zero during the data acquisition. Phase values that are greater than π radians cannot be discriminated from their modulus 2π counterparts. For example, a phase shift of $\frac{3\pi}{2}$ is indistinguishable from a phase shift of $-\frac{\pi}{2}$ radians. So, the velocity corresponding to a phase-shift of π radians defines the upper limit and $-\pi$ the lower limit on the range of

velocities that can be accurately measured. This upper limit is referred to as velocity encoding value or V_{enc}, for short. From Equation (38), V_{enc} is defined as:

$$V_{enc} = \frac{\pi}{\gamma \Delta M_1} \tag{40}$$

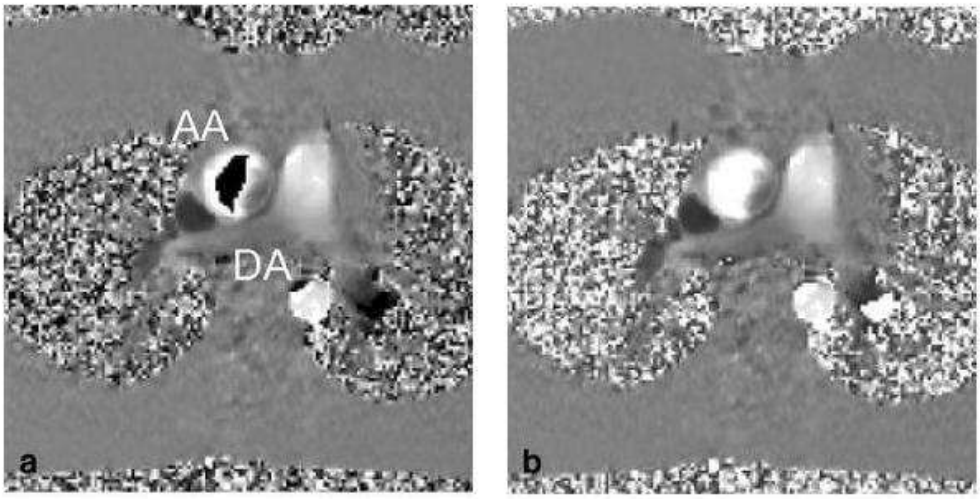

Figure 35: Velocity measurement in the ascending aorta. (a) Aliasing due to small Venc. (b) Correct velocity image after increasing Venc - taken from [30]

Any velocity value outside of the range [$-V_{enc}$, $+V_{enc}$] will be aliased and assigned to a smaller value. Although many methods have been proposed to unwrap the aliased phase values [31, 32], choosing V_{enc} larger than the maximum expected velocity values avoids velocity aliasing and is preferred in Phase Contrast imaging. However, V_{enc} cannot be made arbitrarily large because of the signal-to-noise ratio (SNR) considerations [30, 33] – a large V_{enc} results in more velocity noise. Conversely, a small V_{enc} tends to increase flow ghosting in velocity images. Therefore, choosing the proper value for the V_{enc} requires some consideration. Figure 35 shows the effect of aliasing due to choosing a V_{enc} value smaller than the peak velocity when imaging the ascending aorta. The problem is fixed by increasing the value for V_{enc}. The effect of V_{enc} on standard deviation of measured velocity is given by:

$$\sigma_v = \frac{V_{enc}}{\pi}\ \sigma_\varphi \tag{41}$$

where σ_φ is standard deviation of phase of measured MR signal. Therefore higher V_{enc} causes higher noise in velocity even in constant phase standard deviation.

2.3.5. K-space Trajectories in PC MRI

This section discusses different data acquisitions methods to cover k-space in PC-MRI. There are three major k-space coverage methods: (a) conventional Cartesian trajectory, (b) radial trajectory, and (c) spiral trajectory. Each method leads to different gradient read-outs with their own advantages and disadvantages

2.3.5.1. Cartesian Trajectory

This method uses conventional Cartesian coordinates to cover the k-space (Figure 36). Implementation of this method is straightforward; it is sufficient to add a bipolar gradient in desired flow measurement direction of regular imaging sequence. However, this method can lead to long echo times which can result to signal loss. Additionally, relatively long repetition times decrease the temporal resolution in the case of Cine imaging. Motion artifacts are another disadvantage of Cartesian scans, leading to ghosting of the moving object in the phase-encode direction. Figure 37 demonstrates 2D Cartesian pulse sequence with velocity encoding in slice selection direction. In the case of 3D velocity measurement, same reference scan can be used for all three velocity encoded directions, reducing temporal resolution from $6 * T_R$ to $4 * T_R$.

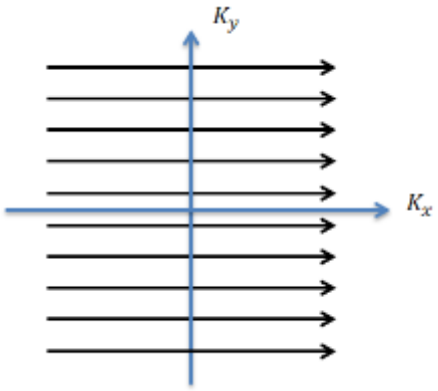

Figure 36: k-space trajectory for Cartesian acquisition.

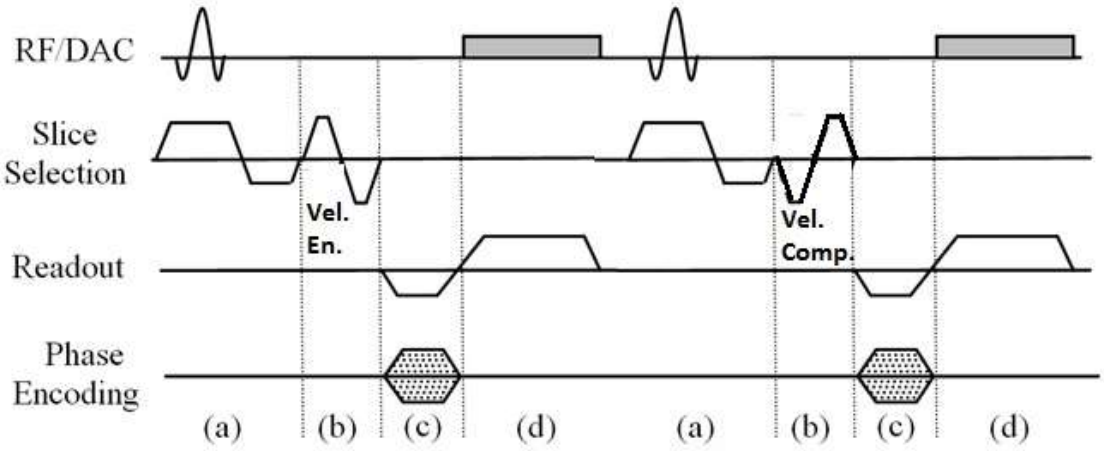

Figure 37: Cartesian PC MRI pulse sequence. It consists of (a) a slice selective RF excitation pulse (b) a bipolar velocity encoding gradient (c) c phase encoding gradient (d) Cartesian read-out

2.3.5.2. Radial Trajectory

Radial phase-contrast has also been developed, but has primarily been used for vessel visualization and angiography, though subsequently, it was extended for quantitative flow measurement. Barger [34] introduced PIPR (Phase-contrast with Interleaved Projections), an interleaved under sampled projection technique for contrast-enhanced phase-contrast angiography. PIPR uses radial trajectory as shown in Figure 38 to fill the k-space. The motivation behind PIPR is that with phase contrast acquisitions, the degree of under

sampling can be even larger than contrast enhanced MRI which is typically used for vessel visualization since in the case of PC MRI, background tissue will be subtracted and will not contribute to artifacts. In PIPR since every velocity encoding (V_x, V_y and V_z) applies to a different projection angle, reducing the number of velocity encoding from six to four as is typical with Cartesian readout is no longer possible.

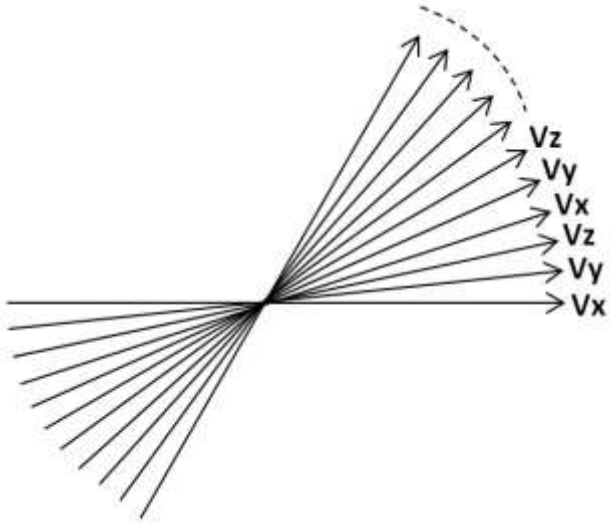

Figure 38: k-space trajectory for radial acquisition.

Relative to Cartesian PC, Radial acquisition can reduce ghosting artifact significantly. However, because of reduced number of acquisition angles, smearing and streaking artifacts will be visible. PIPR suffers from low SNR in the case of high resolution acquisitions, and suffers from under sampling artifacts in the case of low resolution acquisitions. Barger et al. also showed that PIPR can achieve good results in constant flow measurements. Figure 39 shows basic radial pulse sequence. In radial acquisition there is no phase encoding direction and subsequently there is no need to phase encoding gradient resulting in shorter echo time.

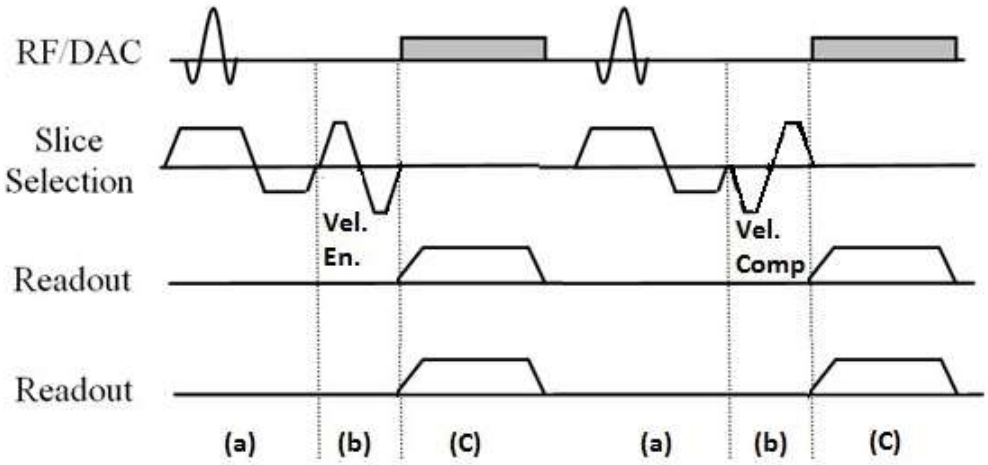

Figure 39: Radial PC MRI pulse sequence. It consists of (a) slice selective RF excitation pulse (b) bipolar velocity encoding gradient (c) radial read-outs.

Recently Ultra short TE (UTE) has been developed based on radial acquisition [35, 36] which has a significant improvement on disturbed flow or flow jet where Cartesian technique fails due to intravoxal dephasing and fluid mixing. This can be done through use of non-Cartesian radial sampling of the Free Induction Decay (FID), and combination of slice-selective and flow encoding gradients.

Generally, with the radial acquisition it is possible to obtain a higher spatial resolution per unit time than with Cartesian phase contrast.

2.3.5.3. Spiral Trajectory

Implementation of PC-MRI with parallel lines in Cartesian trajectory suffers from several issues including error due to acceleration, partial volume artifact, off-resonance, (these will be explained in Sections 2.3.7 and 2.3.8 in detail). Essentially the basic problem with the Cartesian sequence is its long acquisition time which can lead to many other artifacts.

Additionally due to relatively long acquisition time, in breath-held scanning respiratory motion artifacts in the abdomen and thorax areas are more severe. The long acquisition time also decreases the temporal resolution which is undesirable and prevents real-time imaging. Moreover, sampling the center of k-space on every interleave reduces artifacts from pulstile flow [37].

These considerations provide incentive for having a new strategy for covering the k-space, instead of using horizontal read-outs in k-space, a spiral trajectory may be used for filling the k-space. In this method, the repetition time T_R and scan time decrease significantly.

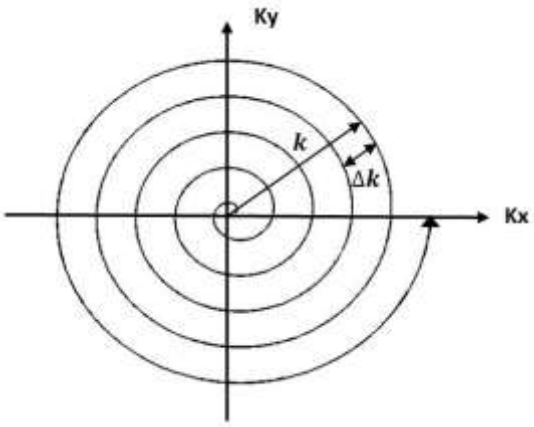

Figure 40: K-space trajectory of a single spiral interleave showing sample spacing Δk, in the radial direction.

Figure 40 shows the k-space trajectory of a single spiral interleave. The shape of the gradient waveforms in spiral MRI is different from the gradient waveform in cartesian MRI [38]; equations (42-44) show the expressions for the spiral gradient waveforms:

$$K_x = k(t)\cos(\theta\,(t)) \tag{42}$$

$$K_y = k(t)\sin(\theta(t)) \tag{43}$$

$$k(t) = A\,\theta(t) \tag{44}$$

Where A is a constant, and is determined by the Nyquist criterion. If Δk is radial distance advanced by one rotation, D is the size of FOV, to satisfy the Nyquist criterion for uniform density spiral trajectories:

$$\Delta k \leq \frac{1}{D} \tag{45}$$

Pike [39] suggested a rapid, interleaved, spiral k-space acquisition. The advantage of this method is the capability for single breath-hold imaging, significantly decreasing time-related artifacts such as respiratory ghosting and acceleration-related errors, among others.

In interleaved spiral phase contrast instead of using one long spiral arm with N rotations, N short spiral interleaves with one rotation can be used (Figure 41). With this approach, the total read-out time required to cover the entire k-space stays the same but density of data sampling increases at the origin leading to higher accuracy and SNR in reconstruction. The Nyquist rate is satisfied in both cases, however with interleaved spiral a higher data density is achieved at the origin of k-space. Additionally, with interleaved acquisitions (with M interleaves), the total read-out time is separated into M shorter read-out times, resulting in less dephasing in outer part of k-space and off-resonance artifacts [40]. Figure 41 demonstrates conventional single shot spiral and interleaved spiral trajectories for covering identical regions in k-space and the pulse sequence for spiral acquisition.

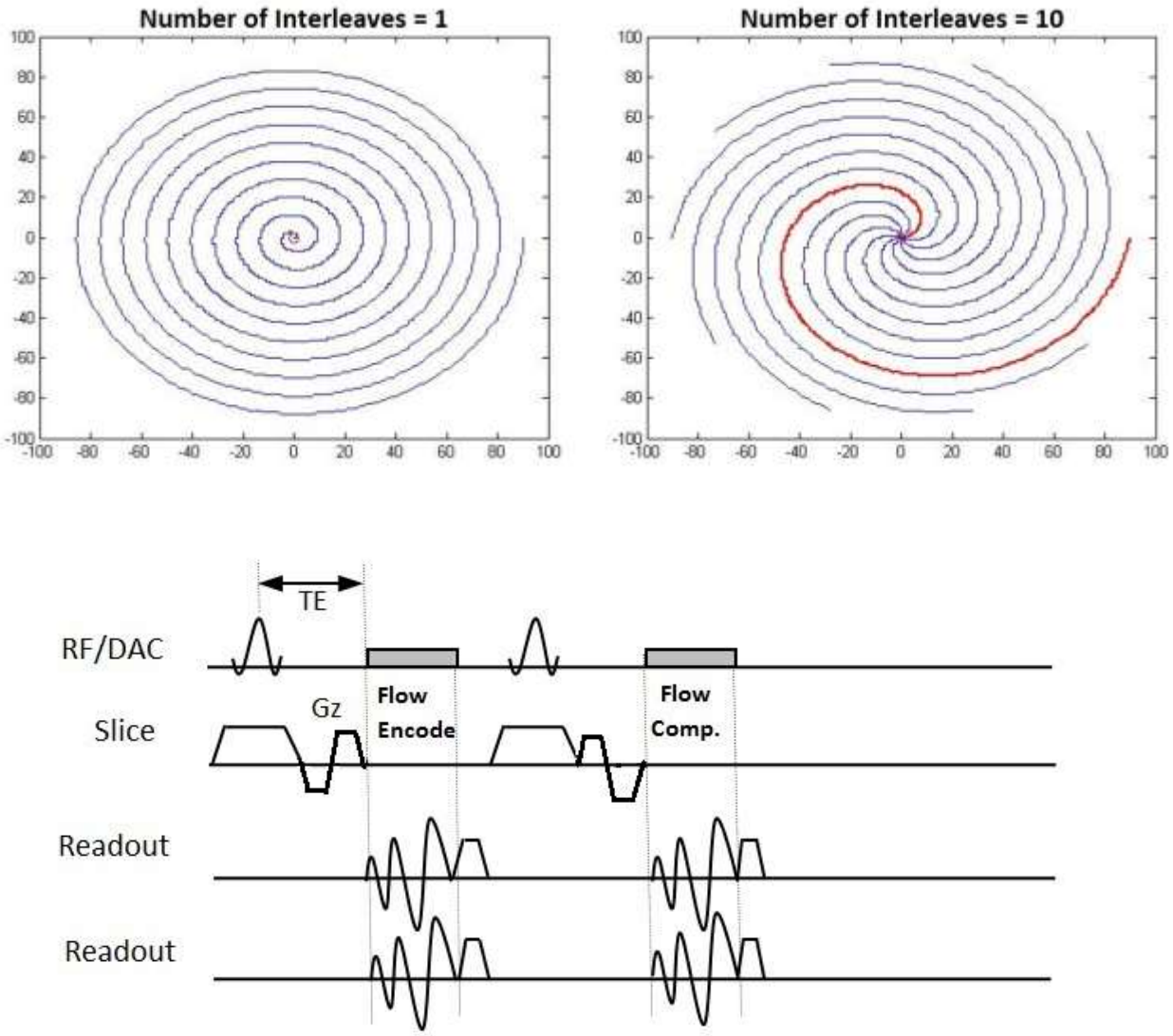

Figure 41 Demonstration of (left top) conventional single shot spiral acquisition with 10 rotations and (right top) interleaved spiral acquisition with 10 interleaves.(Bottom) 2D Pulse sequence of Spiral acquisition with two back to back acquisition, flow encode and flow compensated acquisition.

Many other velocity acquisition and k-space coverage techniques exist which have not been discussed here. Luk Pat et al. [12] proposed one-shot velocity imaging by Bowtie k-space coverage. Barger et al. [41] proposed VIPR (Vastly undersampled Isotropic Projection Reconstruction), they exploited the fact that for MRA, vastly undersampling the number of projections in a 3D projection reconstruction method can be used to limit

the scan time without compromising coverage or resolution. The common disadvantage of non-Cartesian trajectories comes from the basic definition of the discrete Fourier transform which requires Cartesian gridded data as input. As a result, all non-Cartesian acquired data first need to be re-gridded as Cartesian data prior to inverse Fourier transformation, resulting in interpolation errors.

2.3.6. Fourier Velocity Encoding (FVE)

Fourier velocity encoding involves an additional Fourier encoding along a velocity dimension [11, 22]. The velocity variable is v, and the velocity frequency variable is $\mathrm{k_v} = \frac{\gamma}{\pi} \mathrm{M_1}$ (s/cm). Several velocity encoding levels are used to obtain desirable resolution for flow encoding, and different velocity encoding levels are typically achieved by acquiring velocity images with different bipolar gradient amplitudes. The procedure essentially phase-encodes along k_v axis. An image acquired with a particular value of k_v is denoted by $S_{k_x,k_y}(k_v)$. For a specific sample (k_x, k_y), this represents one sample from the Fourier transform of the velocity distribution of all spins in all voxels. The voxel velocity distribution is denoted $s_{x,y}(v)$ and is obtained by one dimensional inverse Fourier transformation along k_v. Velocity field of view determines by increment between successive bipolar velocity encoding amplitudes, and the velocity resolution is determined by the first moment of the largest bipolar velocity encoding gradient. Improving velocity encoding resolution leads to larger bipolar gradients, and decreases temporal resolution[11]. Placing the bipolar gradient along the z-axis will encode through-plane velocities. Placing the bipolar gradient along x or y will encode in-plane

velocities. Oblique flow can be encoded using a combination of bipolar gradients along the x, y, and z axes.

The FVE imaging pulse sequence consists of a slice-selective RF excitation pulse, a bipolar velocity encoding gradient, readout gradients, and refocusing and spoiling gradients. The dataset corresponding to each bipolar gradient is a horizontal plane in k-space with constant kv determined by amplitude of bipolar gradient.

Figure (42) demonstrated FVE pulse sequence with spiral trajectory in x and y directions and velocity encoding (k_v) in z-direction. Figure (43) shows FVE k-space for 4 velocity encoding values with spiral readout. It is clear that such a scheme is time consuming. As proposed by Carvalho et al. [11], partial Fourier reconstruction along velocity encoding dimension can reduce the total imaging time by up to 58%. To demonstrate application of his technique, Carvalho obtained results of spiral FVE acquisitions in the aortic valve and

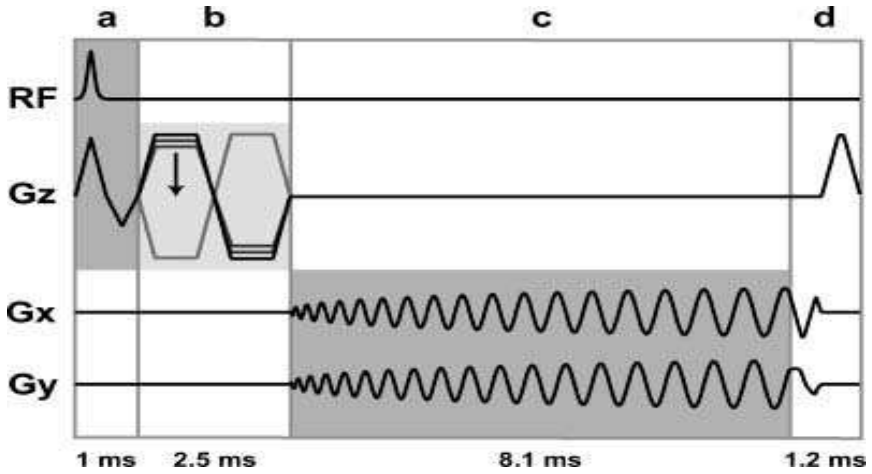

Figure 42: Spiral FVE pulse sequence. It consists of (a) slice selective RF excitation pulse, (b) bipolar velocity encoding gradient, (c) spiral readout, and (d) refocusing and spoiler gradients. Taken from [11]

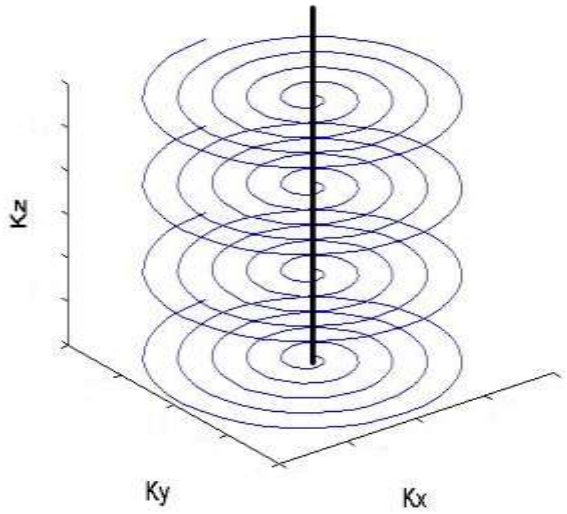

Figure 43: Spiral FVE k -space sampling scheme. The dataset corresponding to each temporal frame is a stack-of-spirals in kx, ky space. Each spiral acquisition corresponds to a different kv encode.

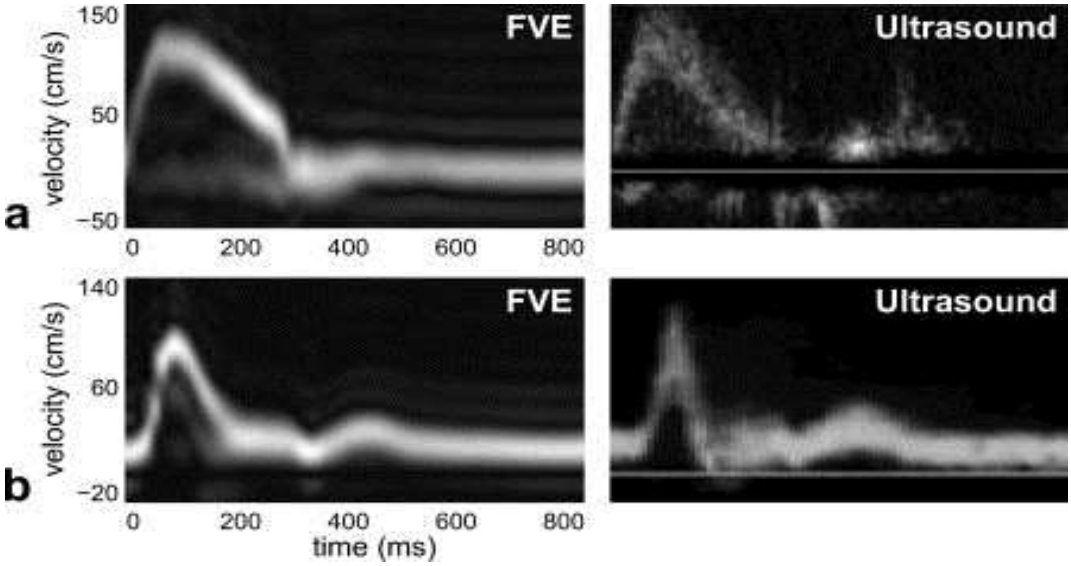

Figure 44: Comparison of FVE and ultrasound waveform in a healthy volunteer in (a) aortic valve and (b) carotid artery taken from [11].

the carotid artery and compared the results with ultrasound. Results showed that the peak and the time velocity waveforms in both the aortic valve and carotid artery were in good agreement with Ultrasound (Figure 44).

2.3.7. Artifacts

There are many artifacts in MRI, and many solutions have been suggested in order to avoid or reduce them. In this section, artifacts relevant to flow and velocity measurement techniques which can occur when collecting MR flow-dependent data such as TOF MRA or PC MRI will be considered.

2.3.7.1. Partial Saturation

This artifact is more severe in sequences that have a high temporal resolution (short T_R), and a wide variety of velocity distribution in imaging slice. This artifact occurs because of partial saturation of spins moving slowly perpendicular to the slice orientation. That is, pre-saturated spins in previous T_R do not have enough time to relax nor enough time to leave the slice. Nayak et.al [13] performed Bloch simulations to find out effective steady state slice profile for different velocities and flip angles. The results, in Figure 45, are images of effective slice profile (horizontal axis) for velocity between 0 and 2 m/s (vertical axis), for different flip angles.

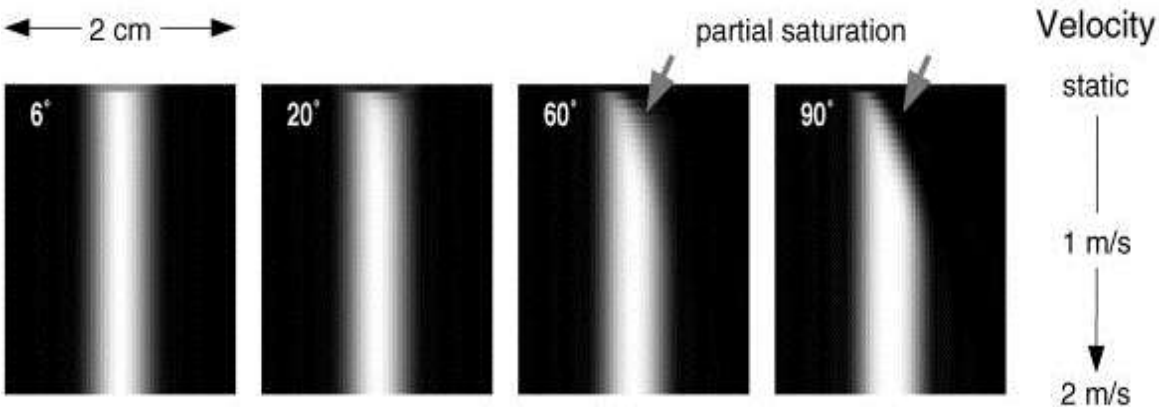

Figure 45: Bloch simulation of the partial saturation effects particularly affecting high flip angles and low velocities. Slice thickness is 2cm, flip angles are [6, 20, 60, 90] degrees, and velocity varies between 0 and 2m/s in the vertical direction. Taken from[13].

It was concluded that with flip angles higher than 20 degree, a partial saturation artifact is more considerable. Also, it was shown that spins moving slower than 50 cm/s can be troublesome. The best way to avoid partial saturation artifact is to use small flip angles. This is especially the case slow moving spins are present within the region of interest.

2.3.7.2. In-Plane Flow Artifact

Another important artifact related to high velocity flows is in plane flow during readout and acquisition. In-plane flow artifact leads to spatial dispersion of flow in the transverse plane. Velocity point spread function (PSF) is a useful tool for illustrating this artifact. The point spread function (PSF) describes the response of an imaging system to a point source or point object. A more general term for the PSF is a system's impulse response [42].

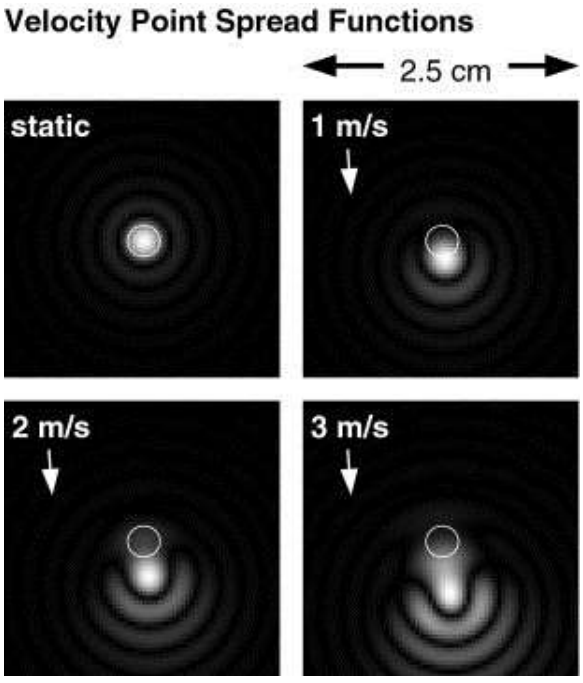

Figure 46 Bloch equation simulation to depict Velocity PSF in the case of in-plane flow during readout. The white empty circle is a special resolution element. As shown in the bottom row, for in plane velocities higher than 2m/s, spatial displacement accrues. Taken from [13].

To obtain velocity PSF, Bloch equations are simulated. Simulations for different in-plane flow showed in plane velocities less than 2m/s exhibit small artifact, and velocities higher than 2m/s are more severe. Nayak [13] performed this simulation to find out dependency of PSF on different velocities, (Figure 46). PSF distortion causes blurring in the direction of flow, displacement artifact, loss of spatial resolution, and partial volume effect.

2.3.7.3. Partial Volume Artifact

Probably partial volume artifact is the most critical in affecting the accuracy of PC velocity measurement. Assume an imaging voxel volume contains 50% static spins and 50% spins moving at a constant velocity. Suppose the phase for moving spins is $\emptyset_m$ and for static spins is zero. The measured signal for this voxel is then a summation of two phase vectors from static and moving spins. The phase of measured signal $\emptyset$, will have a value somewhere between $\emptyset_m$ and zero (Figure 47).

Correction methods for this artifact depend on our goal from measurement. If we want to measure only velocity of moving spins, the desired measurement is $\emptyset = \emptyset_m$, obtained by suppressing signal intensity from static tissue. Many approached have been proposed in order to suppress or reduce the signal from static tissues and to enhance flow related signal (Figure 47B). In the case of volume flow calculation, it is desirable that moving and static spins contribute based on their fraction in the voxel volume. For the example given above, the resultant phase should be $\emptyset = \emptyset_m/2$ (Figure 47A). When multiplied by the total area of imaged vessel in the slice, this value will result in the correct flow[26].

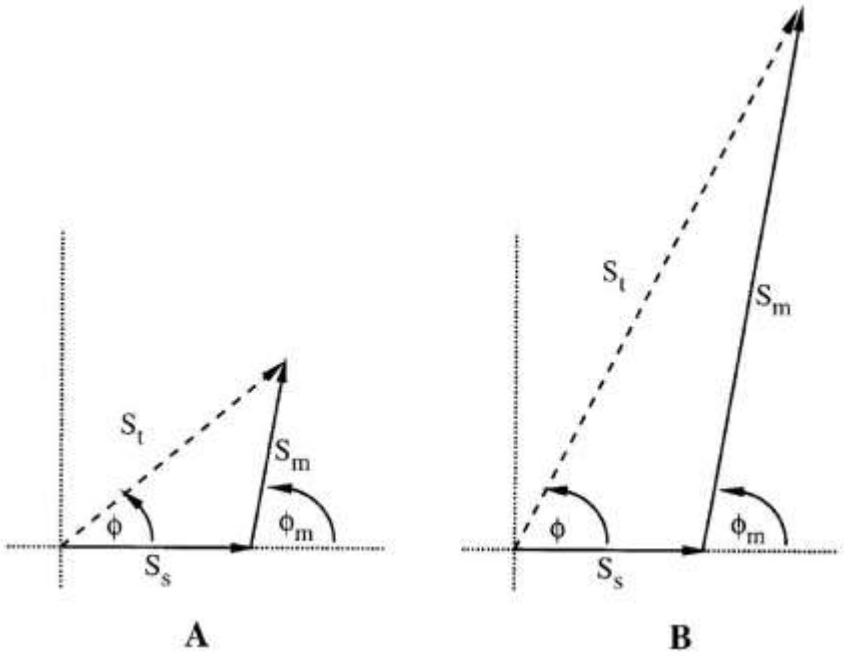

Figure 47: The total signal S_t in voxel is the vector sum of the signals from static spins S_S and moving spins S_M. (a) Without flow related enhancement (b) with flow related enhancement. Taken from [26]

Typically, use of flow enhancement methods results in the moving spins to have a more significant contribution than their actual fraction to the final signal. Figure (47B) demonstrated this situation in which moving spins have 3 times the intensity of static spins. This enhancement would lead to overestimation of flow measurement. Statistical approaches have also been adopted for modeling and estimation of partial volume errors [43, 44].

2.3.8. Phase Errors

There are several factors that can cause imperfection in MRI flow quantification accuracy (both PC and FVE). The major sources of inaccuracy in velocity encoded images are eddy currents, Maxwell terms, gradient field distortions, intravoxel dephasing, and flow acceleration effects [45, 46].

2.3.8.1 Eddy currents

In PC and FVE MRI, two consecutive bipolar velocity encoding gradients cause different eddy currents to be induced in RF Coils – this is due to magnetic field gradient switching, which result in parasitic current in the gradient coil and subsequently lead to phase errors in each phase image. Since the errors are unrelated, subtraction of two phase images does not remove errors due to eddy currents. Many methods have been proposed to correct eddy current errors - by estimating phase errors from surrounding static tissues and subtracting from moving flow phase images[47].

2.3.8.2 Maxwell terms

In MRI, to encode spatial information over the volume of interest, linear magnetic field gradients are employed. However, from Maxwell's equation, the magnetic field must have zero divergence and negligible curl – this results in higher orders of dependency of the linear magnetic field to location. The resulting nonlinear terms are typically referred to as Maxwell terms, causing phase errors. These phase errors are usually corrected during image reconstruction, however, knowledge of the gradient waveforms is required [45, 48].

2.3.8.3 Acceleration

In section 2.3, it was assumed acceleration is zero during imaging this is clearly an oversimplification and in many instances is not satisfied in cardiovascular imaging. By considering non-zero acceleration (and assuming zero higher order terms)

$$\hat{v} = v + a \,.\, \bar{t} \tag{46}$$

Where v is correct velocity and $\hat{v}$ is the measured value. The parameter $\bar{t}$ depends on flow encoding gradients, but essentially is the time interval between the application of the excitation pulse and the flow encoding gradient [26]. As a result, the most effective way to reduce acceleration effect is to reduce T_E, T_R, and the time interval between excitation pulse and flow-encoding gradient; this goal is satisfied by using stronger gradients and well-designed pulse sequences. Many techniques have been proposed for measuring the effect of acceleration on phase images – many techniques have also been proposed for compensating for acceleration [49].

2.4. Conclusions

MRI is a non-invasive modality for accurate and clear anatomical imaging with superb soft-tissue contrast. The intrinsic sensitivity of the MRI signal to spin motion gives us an opportunity to acquire flow and velocity-related information by use of PC and FVE sequences, among others. A disadvantage of phase-based methods (such as PC and FVE) is the sensitivity of the phase image to many factors that can cause artifacts and errors in the measurements, as outlined in Section 3.8 and 3.9. Many approaches have been proposed to estimate and correct them; however, there are still some errors and artifacts that have not yet been fully explained. A long scan time is another factor that has impeded clinical applications of PC and FVE techniques. New methods based on fast sampling strategies such as 4D RTE Spiral has been proposed which to some extent alleviate the scan time problem. The next chapter will investigate the application of a new 4D RTE Spiral phase contrast MRI method for assessment and visualization of flow in both in-vitro and in-vivo scenarios.

CHAPTER 3

LITERATURE REVIEW ON 4D FLOW MRI

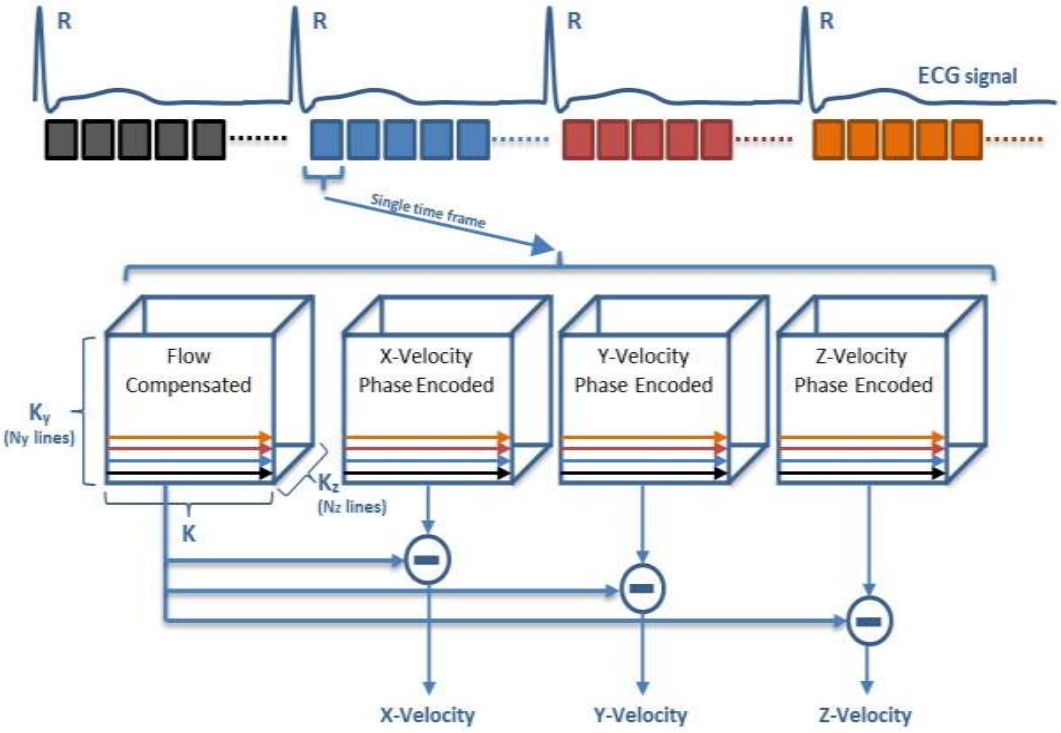

3.1. Introduction

4D flow MRI is a recent development in Phase contrast MRI which provides time-resolved three-dimentional velocity field of a dynamic volume. 4D flow imaging is a 3-D k-space gated acquisition where in the 3rd dimension, an additional phase-encoding is required. 4D flow is proving to be an important tool in clinical studies involving cardiac and cardiovascular disease. Main limitation in application of 4D flow PC MRI has been the relatively long scan time. The scan time becomes even more prohibitive in free breathing studies where application of navigator gating is required, leading to increased scan time; the total scan time being determined by the patients' specific breathing pattern. In this chapter, we describe the variants of 4D flow MRI and explain drawbacks of these techniques, motivating the need for 4D reduced TE (RTE) spiral flow which leads to accurate and clinically acceptable total scan times.

3.2. 4D Flow MRI

Traditional PC-MRI is performed using methods that encode velocity in one direction (often through plane) in a two-dimensional (2D) imaging slice. Time resolved 2D Cine PC MRI is an acquisition gated to the ECG signal which makes it possible to observe temporal variation of velocities and flow at a single 2D slice location within a breath-hold [26, 50]. 4D flow imaging is a 3D gated acquisition and offers the ability to encode all three velocity directions in a 3D spatial volume through time. Results permit time-resolved high spatial resolution imaging of complex flow patterns in a 3D imaging volume. 4D PC MRI can be adopted to visualize global and local blood flow in various vascular regions [51, 52]. Recent studies have shown the potential of 4D PC MRI for detection and visualization of complex flow patterns associated with vascular diseases

such as an aneurysm or stenosis in a variety of vasculatures such as the aorta, carotid arteries, intracranial arteries, etc [53-60]. As 4D flow requires acquisitions with 3 velocity encoding gradient directions in 3 spatial dimensions through time, data acquisition requires much longer scan times, no longer possible in a single breath-hold. Therefore several strategies have been suggested to overcome breathing artifacts in the thoracic and abdominal regions by using navigator echoes, typically placed at the lung-liver interface. These methods which provide respiratory gating permit imaging during free breathing, providing significant benefit in clinical applications however in cost of prolonging total scan time.

3.2.1. Conventional 4D flow MRI

As opposed to 2-D acquisition, in 4-D acquisition, a sequence of temporally gated 3-D k-space acquisitions is performed where for the 3rd dimension, an additional phase-encoding is required (therefore, 3-D acquisitions require read-out along x, phase-encoding along y, and a third phase-encoding along z).

To acquire 4-D Phase Contrast data, further, each line of 3D k-space should be acquired twice (once with flow encoding and once with flow compensation), resulting in temporal resolution of 6 * TR. Assuming Ny and Nz are the number of k-space lines in Y and Z directions, the total scan time in that case will be $Ny * Nz$ heartbeats which can be long in case of a large imaging volume. To speed up the imaging time, the segmented k-space acquisition method is adopted which acquires $Nseg$ k-space lines of all required phase-encoding steps in each cardiac phase, reducing the total imaging time to $Ny * Nz/Nseg$ heart beats. This reduction of the total imaging time is, however, at the cost of decreased

temporal resolution, becoming $6 * TR * Nseg$. As an example, consider Ny=128, Nz=32, TR=7 msec and Nseg=2. These parameters will lead to a total imaging time of $Ny * Nz/Nseg$ =128*32/2 = 2048 heart beats and results in a temporal resolution of 6 * 7 msec * 2 = 84 msec, leading to only a few acquired cardiac phases, not suitable for the purpose of flow calculation especially through the rapidly changing systolic phase of the cardiac cycle. In order to remedy the poor temporal resolution, a four-point acquisition technique was proposed. As described in [61], velocity acquisition for a specific direction requires velocity encoding in two separate scans: a flow-encoded and a flow compensated scan. Therefore, to acquire 3 components of velocities will lead to 6 separate scans, causing long scan times or poor temporal resolution with segmented k-space acquisitions. The four-point method instead requires a flow-compensated acquisition and three velocity encoded acquisitions (one for each of the x, y, and z velocities). With this approach, to arrive at velocities in a specific direction, the same flow compensated acquisition is subtracted from each of the velocity-encoded acquisitions, thus improving the temporal resolution to $4 * TR * Nseg$. As expected, choosing an Nseg > 1 will worsen the temporal resolution but will reduces the total imaging time. Returning to the example previously given, the four point approach once again results in 2048 heart beats for the imaging time, but with TR=7 msec and Nseg = 2, improves the temporal resolution from 84 msec to 4 * 7 msec * 2 = 56 msec. However, if $Nseg$ is increased to 3, it will result in a temporal resolution of 84 msec, while improving the total imaging time to 1365 heart beats. In summary, the four point method improves the temporal resolution or (reduces) the total scan times by a factor of 4/6. Also, consider the fact that using 3 separate 3D flow encoded scans to acquire the 3 components of velocities

requires 3 * Ny * Nz / Nseg successive TR's for acquisition of 3 separate flow encoded scans and 3 separate flow compensated scan. Figure 48 illustrates 4D k-space data collection with the four-point acquisition method with $Nseg = 1$. In addition to simple four-point method other balanced four-point methods like Hadamard and five-point balanced acquisition method have been proposed leading to SNR improvement of velocity data [62, 63]. The Hadamard scheme will be explained in the next section.

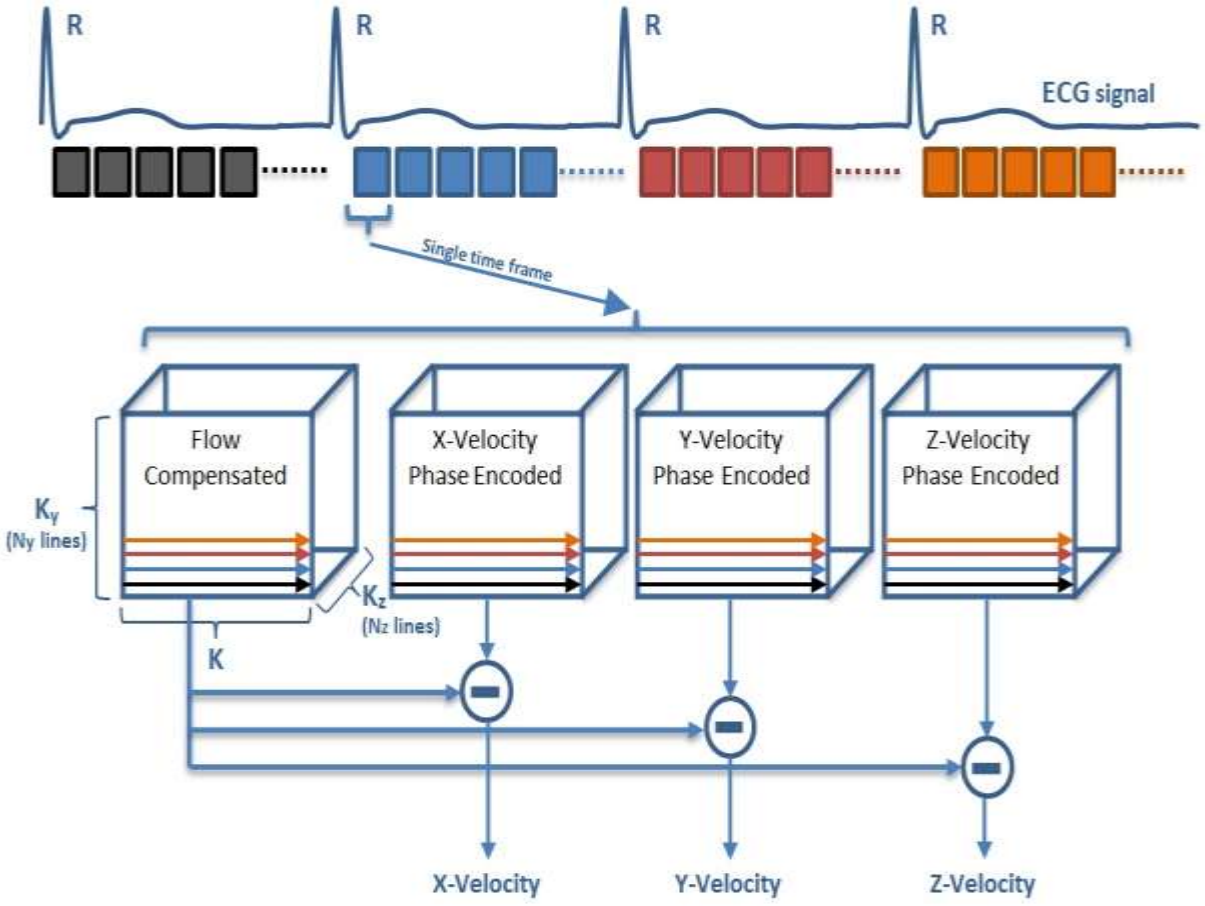

Figure 48: Time diagram of Cartesian 4D PC MRI. In each phase, 4 successive acquisitions are collected. The whole 3D k-space is filled in $NyNz/Nseg$ heart beats.

3.2.2. Previous Work on Conventional 4D Flow

Markl et al. [6] showed the potential for 4D visualization of healthy hearts and adjacent large vessels when using conventional 4D flow with gradient echo sequences, providing short echo and repetition times on the order of TE = 2-4 ms and TR = 5-7 ms. Spatial resolutions were on the order of 1.7*2.2*2.5 mm^3, 3D imaging volume = 320*260*70 mm^3, temporal resolution was on the order of 40.8 ms, and maximum velocity encoding was Venc = 150 cm/s. Scan times were on the order of 14.4-16.5 minutes depending on patient's heart rate and body habitus.

Hope et al. [64] showed the application of conventional 4D flow MRI in the evaluation of a 14 year old boy with Bicuspid Aortic Valve and Aortic Coarctation but without evidence of aortic stenosis or regurgitation. They could show abnormal flow features in patients with aortic coarcation and bicuspid aortic valve (BAV) with mild dilation of the ascending aorta (3.2 cm^2 at the level of the main pulmonary artery). They also show unusual flow features in the ascending aorta that had not been previously reported in this clinical setting and that may be unique to BAV. Their proposed pulse sequence was designed to achieve spatial resolution of 1.17*1.56*2.60 mm^3, FOV = 300*270*78 mm^3, and temporal resolution of 74.4 ms using maximum velocity encoding of Venc=160 cm/s for total scan time of about 14 minutes.

Harloff et. al. [65] demonstrated visualization of potential embolization pathways by 4D flow MRI at 3T. The determination of individual embolic pathways using 4D flow MRI were reported for two acute stroke patients. For the patient data, particle traces were initiated from emitter planes closely positioned at the site of the thrombus or plaque in the ascending aorta. The pulse sequence was designed to provide a spatial resolution of

2.1*3.2*3.5 mm^3 for in-plane FOV = 400*300 mm^2 with slice thickness= 3.5mm, and temporal resolution of 48.8 ms. Echo time and repetition times were 3.5 ms and 6.1 ms, respectively for Venc = 150 cm/s. Based on visualizations on two acute stroke patients they concluded that in contrast to other imaging modalities such as TEE, 4D flow MRI has the capability to evaluate the extent of retrograde flow channel at any user defined location in the entire thoracic aorta. Low temporal and spatial resolution for visualization of detailed blood flow in the supraaortic branches was the main drawback of this study.

4D visualization and quantification with 4D flow MRI is hampered by long acquisition times. Marcus et al. [66] performed quantitative validation of two 4D flow MRI accelerated techniques: one based on Sensitivity Encoding (SENSE) parallel imaging and second based on the Broad-use Liner Speed-up technique (k-t BLAST). 2D PC MRI was performed as a reference scan. The main finding of this study was that quantitative 4D flow MRI accelerated with SENSE has a good accuracy and 4D flow MRI accelerated with k-t BLAST underestimates stroke volume (SV) in comparison to reference 2D PC MRI.

Thirteen healthy volunteers were scanned and the stroke volumes were obtained from different scans and compared. Stroke volumes from SENSE 4D flow MRI (96.2 ∓ 22.6 ml) and 2D PC MRI (98.4 ∓ 18.7 ml) were very close. However, thestroke volume quantified using k-t BLAST 4D flow MRI (84.8+-19.1 ml) was significantly lower when compared to 2D PC MRI (98.4∓ 18.7 ml). Acquisition time for SENSE 4D flow MRI was 22.5 ∓ 0.3 minutes (range 14-33 minutes). 4D flow with k-t BLAST had a shorter scan time of 10.8 ∓ 0.7 minutes (range 8-14 minutes). Remaining imaging parameters were as following. SENSE 4D flow MRI: TE/TR = 3.7/6.3 ms, spatial resolution = 3*3*3

mm^3, temporal resolution 50-55 = ms and SENSE parallel imaging factor = 2. k-t BLAST 4D flow MRI: TE/TR = 3.7/7.6 ms, spatial resolution = 3*3*3 mm^3 and temporal resolution 45-60 ms. 2D PC MRI: TE/TR = 5.3/8.6 ms, spatial resolution = 1.2*1.2*6 mm^3 and temporal resolution = 35ms. The study was performed at 1.5 T.

Navigator gating has always been one of the challenges in 4D flow MRI. Uribe et al. [67] proposed a self-gating technique for respiratory motion compensation for 4D flow MRI. They modified a 4D fast field echo (FFE) phase contrast sequence for respiratory self-gating. Similar to that their previous paper [68], an additional K_0 profile is obtained at certain time intervals (e.g., every 260 ms). A Fourier transform of the K_0 profile along the readout direction (feet-head) resulted in a projection of the whole volume. The breathing motion was obtained by cross-correlating the projections with a reference projection kernel in real time. The output of cross-correlation is a respiratory displacement measured in millimeters, determining whether data is accepted or rejected. If the time efficiency is less than 25%, the position of acceptance window was recalculated based on histogram of the position in the last 30 seconds. Their technique was tested in 15 volunteer quantitatively by measuring the stroke volume in the great arteries and compared to 2D PC MRI as reference scan. To assess the consistency of flow measurements, the ratio of pulmonary stroke volume (Q_p) and aortic stroke volumes (Q_s) were calculated for both methods. Mean, standard deviation, and range of Q_p/Q_s ratio for two acquisition methods (2D PC MRI and self-gated 4D PC MRI) were reported showing a good agreement between the two techniques. The ratio in 2D PC MRI was 0.96 ∓ 0.07 in range of [0.86-1.06] and the ratio in 4D PC MRI was reported to be 0.95 ∓ 0.07 in the range of [0.81-1.03]. For each technique, the other scan parameters were as follows.

Reference 2D PC MRI: spatial resolution = 2.43*2.43*10 mm^3, FOV = 350*300*10 mm^3 TE/TR = 2.4/4.4 ms, temporal resolution = 35.2 ms, nominal scan time = 1:24 minutes. Self-gated 4D PC MRI: spatial resolution = 2.5*2.5*5 mm^3, FOV = 300*260*150 mm^3 TE/TR = 2.7/4.8 ms, temporal resolution = 38.4ms, nominal scan time = 6:15 minutes, effective scan time = 15-16 minutes Note that the nominal scan time is the expected total scan time prior to commencing image acquisition as reported on the console. The effective scan time is the actual scan time which invariably is higher due to gating to the respiratory signal which rejects some of the acquired k-space data.

In another study by Hope et al. [69], 8 healthy volunteers and 26 patients with aortic coarctation were imaged to assess blood flow in the thoracic aorta with conventional 4D flow MRI scan as well as a 2D PC MRI reference scan. Flow waveforms were quantified in two slices in the proximal and in the distal descending aorta for all subjects. Regression analysis (Pearson coefficient r) and limits of agreement (LOA) analysis were used to evaluate blood flow data generated by 4D PC MRI and reference 2D PC MRI data. Comparison showed good agreement between the two approaches (r = 0.99, LOA = -6.8 to 8.3 ml/s for proximal descending aorta and r = 0.99, LOA = -6.9 to10.8 ml/s in the distal descending aorta). Also the difference in the two flow waveforms between these two planes in the descending aorta was used to calculate collateral flow, showing good correlation (r = 0.96 and LOA = -5.4 to 7.7ml/s). Scan parameters for the two techniques were as following. 4D PC MRI: spatial resolution = 1.17*1.56*2.60 mm3, FOV= 300*270*78 mm^3, TE = 2-2.4ms, TR = 4.8-5.5 ms, temporal resolution = 74-77ms, Venc= 160-200cm/s, scan time: 9-15 minutes. 2D PC MRI: slice thickness = 8 mm, TE = 3 ms, TR = 7.1 ms, Venc = 160-250 cm/s. They concluded that 4D PC MRI is a reliable

technique for evaluation of blood flow in the descending aorta and for the calculation of collateral flow in patients with coarctation. The study was performed on 1.5T.

3.2.3. Previous Work on Non-Cartesian 4D Flow

4D VIPR

Conventional 4D flow MRI suffers from longer scan times and/or low spatial resolutions and potentially flow related artifacts. Gu et al. [70] proposed a highly undersampled 3D radial acquisition (isotropic-voxel radial projection) or PC VIPR (Vastly undersampled Isotropic Projection Reconstruction) which has the capability to increase product of volume coverage and spatial resolution by a factor of 30 for the same scan time as conventional 4D flow MRI, providing the possibility to increase spatial resolution or to decrease scan time significantly. The VIPR acquires k-space data along radial trajectories uniformly and each radial line passes through center of k-space. In VIPR streaking artifacts due to the undersampling of the k-space spread out in 3D k-space and are far less noticeable than 2D k-space acquisition. Additionally, streaking artifacts related to stationary tissues are removed by subtraction in PC VIPR which make phase contrast a well suited application for undersampled radial acquisitions. Although PC VIPR can improve scan time and spatial resolution, it limits the in plane resolution due to isotropic resolution and dependency of in-plane resolution and through-plane resolution. The reported imaging parameters are: FOV = 240*240*180 mm^3, spatial resolution = 0.63*0.63*0.63 mm^3, TR/TE = 17.34 / 7.57 ms, number of readouts = 384 and scan time = 3:50 minutes. The sequence was implemented on a GE 1.5 T scanner.

A hybrid radial-cartesian strategy was developed by Kecskemeti et al. [71] for more efficient sampling and benefiting from isotropic in-plane resolution and stack of star approach for through-plane k-space coverage. Despite being highly effective in a variety of clinical applications, the TE in these techniques is still not short enough to resolve the intravoxel dephasing encountered in stenotic flows.

4D UTE

One impediment of conventional 4D flow MRI is the inaccuracy of measured velocity in the presence of a stenotic narrowing which leads to disturbed and turbulent flow. This inaccuracy is the consequence of signal loss, intravoxel dephasing, and flow-related artifact in the presence of disturbed and turbulent flow. Several approaches have been developed to mitigate the signal loss and flow-related artifacts in PC-MRI [72-74]. One important approach that has revealed significant impact in correction of the signal loss involves reduction of the echo time (TE) and gradient duration [36, 75]. Reducing the TE improves signal loss and intravoxel dephasing by giving less time to spins to mix and dephase in the time period between excitation until signal acquisition. The approach results in higher signal to noise ratio and more reliable estimation of disturbed and jet flows since a shorter TE will mitigate the effect of intravoxel dephasing caused by random fluid mixing.

4D UTE flow MRI was developed in [36] to counter this issue. It uses a combination of radial 4D PC MRI and Ultra Short TE (UTE) acquisition [35] methods and provides significantly shorter TEs with improvement in flow quantification of disturbed and turbulent blood flow and stenotic flows. In [36], it was shown that 4D UTE flow MRI is

capable of performing more accurate flow quantification for the case of stenotic flows with velocities greater than 4m/s when compared to conventional 4D flow. The imaging parameters for phantom studies were as follows. Conventional 4D flow: spatial resolution: 1.5*1.5*3 mm^3, FOV = 100*100*60 mm^3, flip angle = 10, number of slices = 20, TE/TR = 5.9/13 ms for Venc = 50 cm/s and TE/TR = 3.9/8 ms for Venc = 700 cm/s, scan time = 17:54 minutes for Venc = 50 cm/s and scan time = 6:38 for Venc = 700cm/s. Imaging parameters for 4D UTE flow were: spatial resolution: 1.5*1.5*3 mm^3, FOV = 100*100*60 mm^3, flip angle = 10, number of slices = 20, TE/TR = 3.3/13 ms for Venc = 50 cm/s and TE/TR = 0.98/8 ms for Venc = 700 cm/s, scan time = 18:02 minutes for Venc = 50 cm/s and scan time = 6:50 minutes for Venc = 700cm/s. For 4D UTE scan, 50% radial sampling was used to reduce the scan time. The scan parameters for in vivo results were as follows: spatial resolution = 2.5*2.5*5 mm3, FOV = 230*230*50, flip angle = 10, Venc = 400 cm/s, number of phases = 16, TE/TR = 3/6.9 for conventional 4D flow and TE/TR= 1.15/4.6 ms for 4D UTE MRI. For the 4D UTE sequence, 75% sampling of radial k-space lines was performed to reduce the scan time. The scan time for both 4D scans was about 4 minutes. However, due to the application of navigator gating, each scan took on the order of 10 minutes. Imaging was performed on a 1.5T scanner. They concluded that the main limitations of 4D flow MRI is long acquisition time, which is more problematic when performing in vivo studies. Long acquisitions for in vivo studies lead to the need to reduce volume coverage and/or spatial and temporal resolutions. Although the scan time for 4D UTE flow is in general longer than conventional 4D flow, it can be reduced through radial undersampling of k-space but at the cost of reduced accuracy.

In [76] 6 patient with mild to moderate aortic stenosis were scanned with conventional 4D flow and 4D UTE methods as well as Doppler Ultrasound as the reference technique. Same scan parameters as mentioned in [36] were used. Results showed good agreement between both 4D flow and Doppler ultrasound methods. However, in 4D flow, low temporal resolution may lead to underestimation of peak velocities. Additional issue was total scan times, longer than 10 minutes due to reduced scan efficiency resulting from use of a respiratory navigator. Relative to conventional 4D flow, it was reported that 4D UTE flow has more significant correlation with Doppler US in patients with peak gradient > 40 mm Hg where more significant spin dephasing may be present.

Spiral 4D flow MRI

An important impediment of conventional 4D flow MRI is that the total scan time is long, especially in large volumes with high spatial resolutions.

Spiral k-space trajectory has valuable attributes which can help overcome some of the problems with conventional 4D flow acquisitions [77, 78]. The most important advantage of the spiral acquisitions is its scan efficiency due to elimination of the phase-encoding gradient and use of two readout gradients which are applied simultaneously. However, spiral 4D flow also has the advantage of reducing the phase error and signal loss by permitting a shorter echo time. In addition, signal to noise ratio (SNR) is higher due to oversampling of center of k-space [13, 79].

In general however, spiral readouts in phase contrast MRI are more sensitive to system imperfection, and RF and B_0 inhomogeneity. With new advances in MRI hardware, including gradient coils and RF coils, this problem has been solved to some extent. A

second important previous limitation was the off-resonance artifact which was encountered when performing k-space coverage with a long spiral arm. This problem may be avoided by providing k-space coverage through multiple short interleaved spiral arms.

Nayak [13] proposed a rapid 2D spiral PC sequence for quantification of flow in high speed flow jets in patients with congenital defects and patients with valvular disease. His method used short spiral readouts (less than 4ms) in order to minimize flow artifacts and used prospective gating. This method also achieved a good spatial resolution (2*2*4 mm) which helped reduce partial volume errors. Because of the short readout time, this method was capable of overcoming the off resonance artifact as shown through a Bloch equations simulation. Acquisition could be performed in one breath-hold for a single slice with single direction flow encoding. The main limitation of this method was that to obtain all 3 velocity directions, 3 separate acquisitions were needed, increasing scan time by a factor of three. Another issue, inherent to all 2-D imaging methods is their inability to perform 3D volume acquisition. Finally, another concern relates to measurement of peak velocity. As noted in [13], in all single velocity encoding PC MRI techniques, the measured peak velocity is underestimated by a factor of $\cos\alpha$, where α is angle between the flow direction and the flow encoding direction.

Similar to Nayak et al., previously a rapid 2D Spiral Phase Contrast technique with short echo and scan times for imaging the iliac artery was proposed [50]. Scan parameters were: spatial resolution = 1.5*1.5 mm^2, slice thickness = 5 mm, FOV = 250*250 mm^2, Venc = 100 cm/s, segmentation factor (TFE factor) = 3, temporal resolution = 42 ms, TE/TR = 2.6 / 7 ms for spiral acquisition and TE/TR= 4.1/7 ms for Cartesian acquisition.

Flow wave form in iliac artery was plotted using both techniques. The spiral method reduced the scan times from 55 seconds in Cartesian to 26 seconds (and even down to 11 seconds) with the same level of accuracy. Experiments were performed at 3T. In comparison to the conventional Cartesian acquisition, all spiral acquisitions have the ability to overcome flow-induced ghosting artifacts in the phase encoding direction which occur due to vessel pulsations and are prominent in Cartesian scans.

A major drawback of previous Spiral techniques was that they acquired velocities only in one flow encoding direction, therefore requiring 3 separate scans to collect all velocity components. Recently, Sigfridsson et al. [77], proposed spiral 4D flow MRI with stack of spiral interleaves for pulsatile 3D velocity acquisition in a 3D volume. They proposed two spiral configurations to acquire k-space data. The first configuration, referred to as TR-interleaved, acquires one spiral interleave per cardiac cycle every TR seconds and interleaves the velocity scan segments every TR seconds --using a segment factor of one results in temporal resolution of 1*4*TR. This approach requires N heart beats to collect N spiral arms for full k-space coverage giving rise to 3 separate velocity encoded Cines. The second configuration referred to as beat-interleaved, interleaves one velocity encoding in each heart-beat. Assuming a segment factor of two, results in temporal resolution of 2*1*TR since separate velocity encodings are performed in different heart beats, thus requiring 2*N heart beats to collect 3 velocity encoded Cines. Assuming a constant TR, the second configuration can achieve a higher temporal resolution at the cost of a longer scan time. Due to adoption of the spiral acquisition, when compared with the conventional 4D flow acquisition, their method was able to reduce the scan time up to half. The main issue with their method is the long echo time which may result in artifacts

when imaging patients with a vascular or valvular narrowing. The Sigfridsson et al.'s method provides echo times on the order of 3.5 ms in spiral acquisition versus 3.4 ms for the conventional Cartesian acquisition for identical imaging parameters. The other limitation of their approach was the relatively large voxel size (2.8*2.8*2.8 mm^3) which may lead to partial volume artifact. It is expected that partial volume artifact will be more severe for the case of stenotic flows which include turbulent jet and eddy flows and as a result a range of varying velocities in a short distance distal to a stenotic narrowing.

3.2.4. Hadamard Flow Encoding

The conventional (non-Hadamard) PC acquisition uses 2 acquisitions (a flow encoded and a flow compensated) to reconstruct each component of the velocity map separately. Doumoulin et al. [80], proposed use of Hadamard flow encoding in order to improve SNR for better visualization of 3D PC MRA. To increase the SNR, the four-point balanced Hadamard technique may be employed in conjunction with both the conventional and the non-conventional 4D flow MRI methods. Conventional (non-Hadamard) flow encoding consists of one flow compensated scan followed by 3 flow sensitive scans. However in this case, the bipolar velocity encoding gradients are only present in one flow encoding direction at each time (the flow-sensitive scan) and when present, they have a positive polarity. Hadamard flow encoding on the other hand makes use of bipolar velocity encoding in all directions in that all acquisitions are flow-sensitive, but the polarity of the velocity encoding gradient for separate directions may be positive or negative. Table 3 shows Hadamard and non-Hadamard flow encoding gradient polarities.

As illustrated in Table 3 for Hadamard scheme, in acquisition 1, the velocity encoding gradient has a positive polarity in all directions. Acquisition 2 encodes velocity with positive bipolar polarity in the Z direction and negative bipolar polarity in the Y and X directions. Acquisition 3 encodes velocity with positive bipolar polarity in Y direction and negative bipolar polarity in Z and X directions. Finally acquisition 4 encodes velocities with positive bipolar polarity in X direction and negative bipolar polarity in Z and Y directions.

In the non-Hadamard scheme, acquisition 1 is a flow compensated scan and does not have velocity encoding gradient in any direction. Acquisition 2 encodes velocity in Z direction with positive polarity and is flow compensated in Y and X directions. Acquisition 3 encodes velocity in Y direction with positive polarity and compensates flow in Z and X direction. Finally acquisition 4 encodes velocity in X direction with positive polarity and compensates flow in Z and Y directions.

Table 3 Comparison of velocity encoding polarities for the Hadamard and Non-Hadamard flow encoding methods. The entries in the table mean that to obtain flow velocity component for a specific velocity encoding direction, results are added, subtracted, or have zero weight.

Hadamard Gradient Polarity		Consecutive Acquisition number			
		1	2	3	4
Velocity Encoding Direction	Z	+	+	-	-
	Y	+	-	+	-
	X	+	-	-	+
Non-Hadamard Gradient Polarity		Consecutive Acquisition number			
		1	2	3	4
Velocity Encoding Direction	Z	0	+	0	0
	Y	0	0	+	0
	X	0	0	0	+

To reconstruct velocity in Hadamard scheme data in each direction all 4 acquisitions are combined using following equations:

$$+Scan_1 + Scan_2 - Scan_3 - Scan_4 = 4 * V_Z \quad (47)$$

$$+Scan_1 - Scan_2 + Scan_3 - Scan_4 = 4 * V_Y \quad (48)$$

$$+Scan_1 - Scan_2 - Scan_3 + Scan_4 = 4 * V_X \quad (49)$$

Equations 1-3 can be rewritten in matrix form as

$$\begin{bmatrix} +1 & +1 & -1 & -1 \\ +1 & -1 & +1 & -1 \\ +1 & -1 & -1 & +1 \end{bmatrix} \begin{bmatrix} Scan_1 \\ Scan_2 \\ Scan_3 \\ Scan_4 \end{bmatrix} = 4 * \begin{bmatrix} V_Z \\ V_Y \\ V_X \end{bmatrix}$$

The main point that the reader should pay attention to is that by performing velocity encoding in all directions at all times results in a 4 fold increase in SNR but results in the same total scan time.

3.3. Conclusion

This chapter reviewed the fundamentals of 4D flow MR imaging using both Cartesian and Non-Cartesian trajectories. Also some of the more important previous applications of 4D flow to clinical imaging were reviewed. From this overview, it may be observed that long scan times and long echo times are major drawbacks of conventional 4D flow methods. The next chapter will discuss the details of the new 4D RTE Spiral flow imaging technique which as the name suggests is based on the spiral acquisition with a

stack of spirals which not only results in reduced scan times but it also results in reduction of the echo time in comparison with conventional 4D flow techniques.

CHAPTER 4

4D REDUCED TE (RTE) FLOW MRI

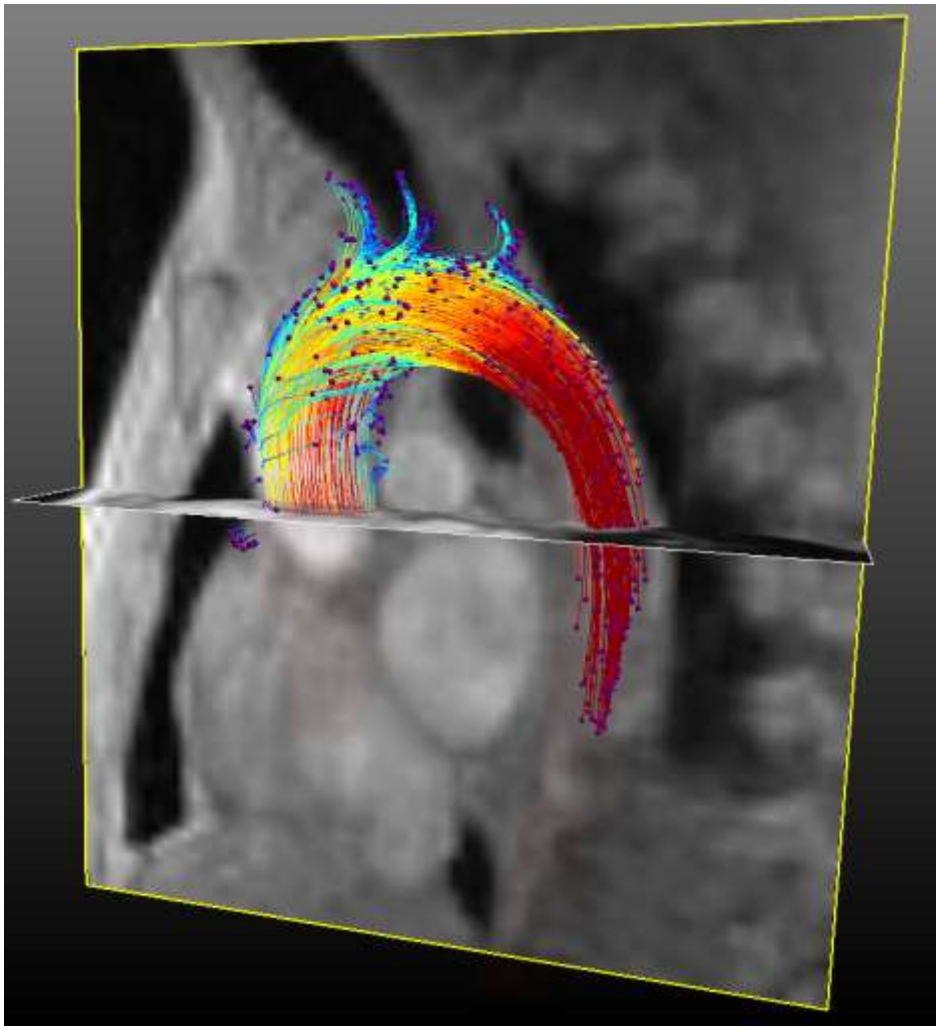

4.1. Introduction

In this chapter, a detailed description of 4D RTE Spiral PC MRI technique will be given. Subsequently, we report on extensive in-vivo and in-vitro validation of the methods. In-vitro studies were performed in a stenotic flow phantom under both steady and pulsatile flows using both conventional 4D flow MRI and 4D RTE spiral flow MRI. The comparison of results between these methods will be described in this chapter. In addition, five healthy volunteers and five patients with mild to moderate aortic stenosis were recruited and imaged to demonstrate the feasibility of the proposed method for in-vivo applications. Results from a correlative study of the proposed method with Doppler US are also reported in this chapter.

4.2. Reduced-TE Spiral 4D flow MRI

As noted earlier, in addition to the longer acquisition times, atherosclerotic disease and vascular occlusions cause challenges to conventional PC acquisitions; due to intravoxel dephasing secondary to disturbed blood flow and turbulence distal to narrowing, often resulting in signal loss and flow-related artifacts [13, 36, 37, 81].

In addition to scan efficiency, spiral acquisitions with shorter TE also have the potential to reduce the signal loss and flow-related artifacts and improve the accuracy of flow quantification which as noted in Section 2.3 can be handled with a 4D UTE approach [36]. In this thesis, a reduced-TE spiral 4D flow MRI technique has been designed which in addition to reducing the total scan time, through the combination of bipolar and slice select gradients also reduces the TE when compared to Sigfridsson et al.'s implementation.

4.2.1 Combining the bipolar and slice select gradients

Kadbi et al. [36, 55] showed that the echo time (TE) can be shortened through combination of slice selection gradient with bipolar flow encoding gradient. In the case of 4D UTE PC which involves radial acquisition of k-space and FID sampling, TE is defined as the distance from center of excitation RF pulse to the beginning of the readout gradient.

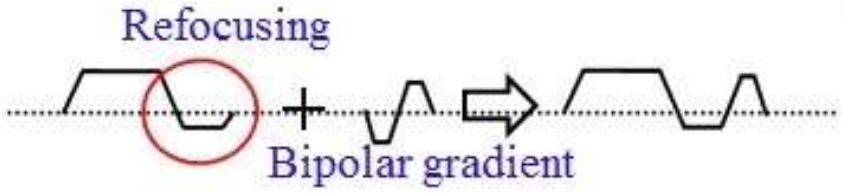

Figure 49 combination of refocusing lob of slice selection gradient with bipolar velocity encoding gradient to acquire shorter echo time.

Figure 49 demonstrates combination of refocusing lob of slice select gradient with bipolar velocity encoding gradient. In comparison to the conventional Cartesian acquisition, this approach can reduce the echo time (TE) up to 0.5-1.5 ms depending on the length of each gradient and assigned Venc value.

Figure 50 demonstrates 4D reduced-TE spiral pulse sequence with combined gradients [55]. This sequence has 4 parts, each lasting for one repetition time (TR) and leading to minimum temporal resolution of 4*TR. As shown in the figure, the pulse sequence consists of flow encoding in z, y and x directions and a reference scan which is flow compensated. Figure 51 shows the schematic of 4-point balanced Hadamard 4D flow with spiral readouts that we utilized for MRI flow data collections described in Chapter 4.

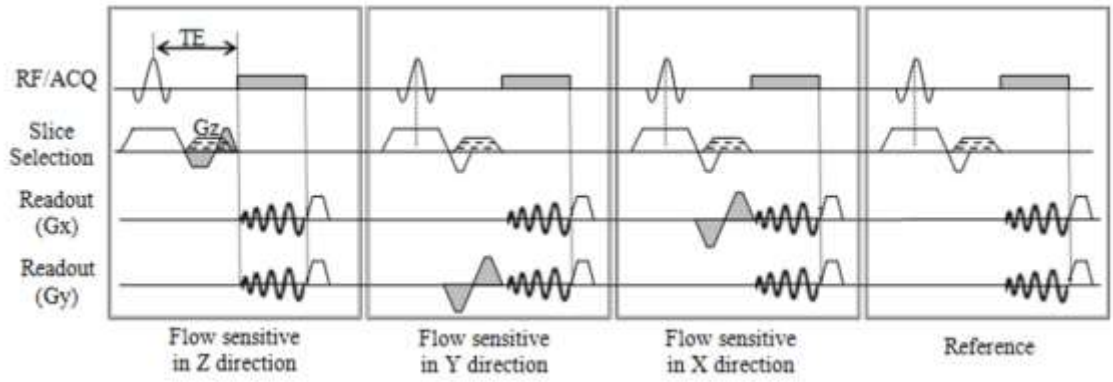

Figure 50: Reduced TE Spiral 4D pulse sequence. It consists of 4 parts. Flow encoding in Z, Y, and x directions and reference scan from left to right respectively.

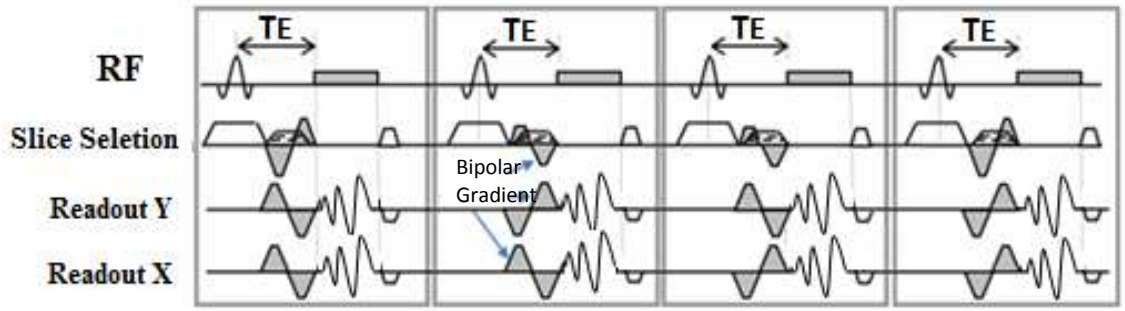

Figure 51: Reduced TE Spiral 4D flow with 4-point balanced Hadamard velocity encoding scheme

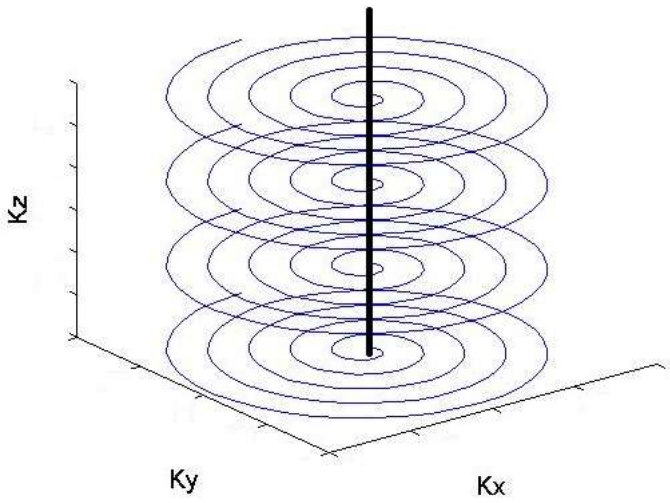

Figure 52: 3D k-space with stack of spirals in z direction.

A stack of spiral trajectories will be used to cover the 3D k-space volume as illustrated in figure 52. Additionally to avoid the off resonance artifact in the outer regions of k-space, which occurs due to T2* signal decay, we can use a stack of interleaved spiral arms in k-space [55].

Interleaved spiral adopts cover k-space with several short spiral arms instead of one long spiral arm. This technique decreases repetition time (TR) and consequently improves the temporal resolution. Other advantages include higher sampling density at the center of k-space which will increase the SNR. Figure 53 shows a stack of interleaved spiral trajectories, covering the 3-D k-space.

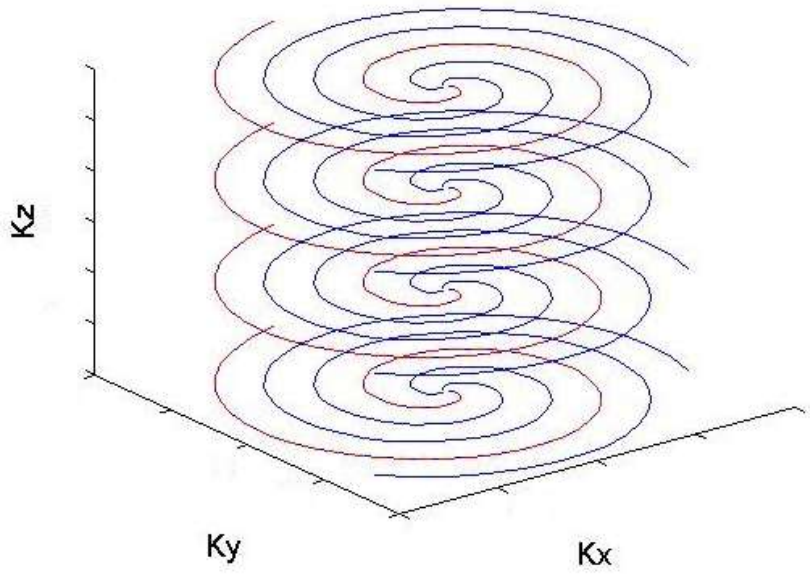

Figure 53: 3D k-space with stack of interleaved spiral arms. In this illustration, each 2D plane of constant Kz is covered by 3 spiral arms.

Short repetition time (TR) in interleaved Spiral also allows acquiring more than one interleave in each cardiac cycle and still maintains a reasonable temporal resolution. In general there is always a tradeoff between length of interleaves to cover the k-space and

temporal resolution. Using longer spiral interleaves will lead to a reduced number of read-outs to cover the k-space and as a result shorter scan times (though at the price of a longer TR and poor temporal resolution and in general worse image quality due to T2* decay and off-resonance effects). To achieve a better temporal resolution, one should use many short spiral interleaves, but this will lead to longer scan times. The latter approach in general will lead to improved image quality due to reduction of off-resonance artifact. Depending on the specific application, and image quality and scan time constraints, different spiral configurations may be adopted.

4.3. In-vitro stenotic flow phantom circuit

Experiments were carried out using a closed loop flow system (Figure 54). A MR compatible, computer controlled pump (LB Pump, LB Technology LLC, Louisville, Ky) with the capability to generate user-provided flow waveforms was used. An idealized rigid model of axisymmetric Gaussian shape was machined from transparent acrylic using conventional CNC machining methods initially aimed at 90% area occlusion. Later, the exact geometry was measured with high-resolution CT scans (0.22 × 0.22 × 0.625 mm3) and the area occlusion was found to be 87%. There were additional imperfections in fabrication of the phantom which caused the phantom geometry to not be completely axi-symmetric. The stenosis diameter narrowed from 25.4 mm at the inlet to 9.04 mm at the throat. To ensure fully developed laminar flow at the entrance of the model, a 75-cm long straight rigid acrylic tube was placed upstream of the test section. The viscosity of the blood-mimicking solution utilized in the flow circuit was measured using a LVT Cone-Plate viscometer (Brookfield Labs., Stoughton, MA, USA) to be 0.0043 Pa.s at 68°F. The density of the solution was 1035 kg/m3.

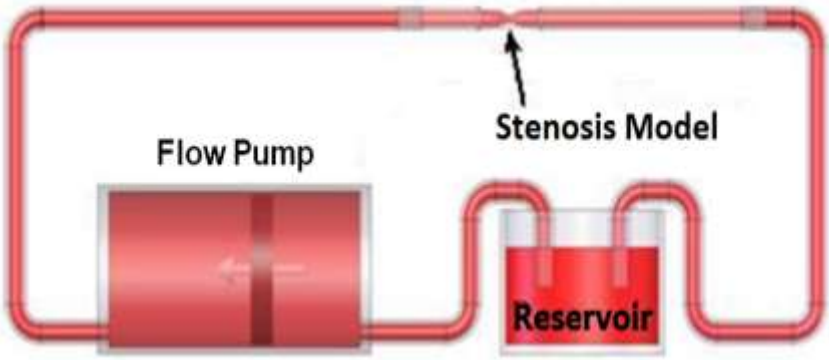

Figure 54 Schematic of the stenotic flow circuit used in MRI experiments. Within the phantom, flow goes from left to right. Note that the z coordinate runs along the phantom and x,y coordinates are axial to the phantom.

4.4. In-vitro imaging Protocol

Imaging was performed on a Philips Achieva 1.5T scanner (Philips Healthcare, Best, NL) using a 16-element SENSE knee coil. The imaging volume covered 60 mm of phantom including 15 mm proximal and 45 mm distal to the stenosis. Center of knee coil and iso-center of scanner was positioned 15 mm distal to the throat of the stenosis. Table 4 summarizes the imaging parameters for conventional 4D flow and 4D RTE spiral flow acquisitions with 12, 24, and 36 interleaves for Q= 50 ml/s, 100 ml/s, and 150 ml/s. The size of the field of view (FOV) as well as the spatial resolution, flip angle, matrix size, and number of signal averages were kept the same for all experiments.

To design the spiral configuration, about 70% of the total read-out time for one Cartesian acquired frame was divided by the number of proposed interleaves. In these experiments, the total read-out time was 66 phase-encoding steps * 3.2 ms for each read-out per phase-encoding step=211.2 ms. Total read-out time per frame was therefore calculated to be 144 ms for the spiral acquisition and was divided by the number of planned spiral interleaves, leading to 12, 6, and 4 ms readouts for 12, 24 and 36 interleaves, respectively. In the case of 12 interleaves with 12ms readouts, readout time was reduced

to 9ms to avoid off-resonance artifact and in order to improve the image quality. Table 4 reports the imaging parameters for all experiments. Figure 55 shows the actual set up of flow phantom inside the MRI scanner.

Table 4 Scan parameters for conventional 4D and 4D RTE spiral acquisition with 12, 24, and 36 interleaves for steady flow phantom studies at Q=50 ml/s, 100ml/s and 150 ml/s flow rates.

Q [ml/s]		**50**	**100**	**150**
Reynolds Number	Inlet	618	1236	1854
	Throat	1711	3422	5134
Venc [cm/s]		150	300	450
FOV [mm]		100*100*60		
Resolution [mm]		1.5*1.5*3		
Matrix Size		68*68		
Flip angle		6^{o}		
Number of signal averages		1		
Cartesian	TE/TR [ms]	3.6 / 6.4	3.3 / 6.1	3.2 / 6.0
	Readout time [ms]	3.2	3.2	3.2
RTE Spiral-12	TE/TR [ms]	2 / 13	1.71 / 13	1.57 / 13
	Readout time [ms]	9	9	9
RTE Spiral-24	TE/TR [ms]	2 / 10	1.71 / 10	1.57 / 9.9
	Readout time [ms]	6	6	6
RTE Spiral-36	TE/TR [ms]	2 / 8.8	1.71 / 8.5	1.57 / 8.4
	Readout time [ms]	4	4	4

Figure 55 Actual set up of flow phantom inside MRI scanner. The pump and control unit are in the lower right hand corner of the room and cannot be seen in the picture.

4.5. In-Vitro Experimental results

4.5.1. Steady Flow

For the steady flow experiments, 3 flow rates of 50 ml/s, 100 ml/s and 150 ml/s were investigated. These flow rates are associated with Reynolds number of 618, 1236 and 1854 at the inlet and Reynolds numbers 1711, 3422 and 5134 at throat of stenosis for flow rates of 50, 100 and 150 ml/s respectively (Table 4). These Reynolds numbers cover the range of Reynolds numbers encountered in human circulation except perhaps flow through a severe aortic valvular stenosis which may result in peak Reynolds numbers of 10,000.

Table 4 shows Reynolds numbers, Venc, TE, TR, and scan time for steady flow experiments for both the conventional 4D flow and 4D RTE spiral acquisitions at 3 flow rates. To compensate for the constant noise of flow-on acquisitions, the image of flow-off acquisition with identical imaging parameters were subtracted from the phase image of flow-on acquisitions for all 4D flow acquisitions. To compute flow waveforms from velocity data, velocity data were manually segmented in each axial slice based on a circular mask with a predefined diameter in in-house software developed in matlab. To reduce the effect of partial volume effect, pixels having less than 50% area inside the ROI were excluded from flow calculation analyses. Flow in each cross section results from summation of all through-plane velocity components for that slice.

Quantitative Comparison of Flows

To assess the degree of accuracy between the reference flow at the inlet and measured flow, the relative root mean squared error metric was adopted:

$$\mathrm{RRMSE} = 100\% \times \sqrt{\frac{\sum_n (\mathrm{Q_{sp/conv}(t) - Q_{inlet}(t)})^2}{\sum_n (\mathrm{Q_{inlet}}(t))^2}} \tag{50}$$

where Q_{inlet} is inlet reference flow measured with conventional 4D flow by averaging the flow in 3 slices proximal to the stenotic narrowing and Qsp/conv is the measured flow using the proposed 4D RTE spiral acquisition or the conventional 4D flow acquisition. n is the slice position number along the phantom length where in n=1 is the first collected slice and n=20 is last collected slice. Note that n=5 is the slice located at the center of the stenosis, slice n=1 is located at z=-12 mm and slice n=20 is located at z=+45 mm. Figure 56 shows a schematic geometry of the phantom and different regions of FOV for data

analyses. To further assess accuracy for the case of steady flows, we also calculated a mean flow rate by averaging the flow rate across all 20 collected slices and compared that with the reference flow. Table 5 shows scan time, measured mean flow rate, and RRMSE for both the conventional 4D flow acquisition and the 4D RTE spiral flow acquisition with 12, 24, and 36 interleaves for Q= 50 ml/s, 100 ml/s, and 150 ml/s constant flow rates.

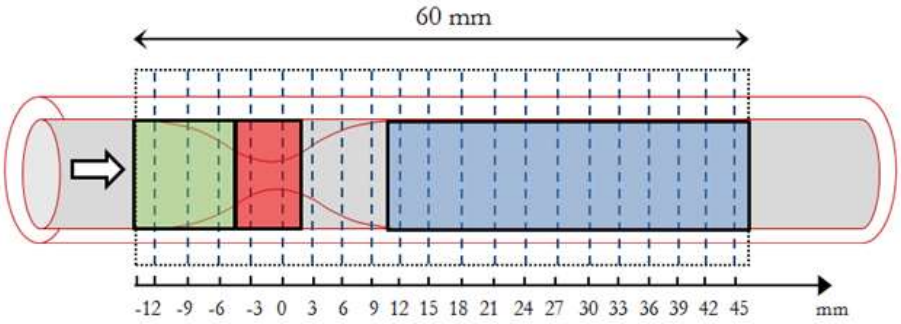

Figure 56: A schematic geometry of the phantom and the sagittal extent of the FOV for data collection. Dashed lines represent the location of axial slices along the phantom. The green, red, and blue areas are regions proximal, at the throat, and distal to the stenosis that were considered separately in the data analyses. Taken from [36].

According to the pump's manufacturer specification sheet, there can be up to 4% error between prescribed flow rate which is set in the pump's controller panel and a measured flow rate. Additionally the prescribed pulsatile flow waveform is significantly different from the measured flow waveform due to compliance of the tubes and flow connectors. For these two reasons, as noted earlier, we use the mean flow waveforms in 3 slices proximal to stenosis using Conventional 4D flow acquisition as the reference flow measurement. All the 20 collected slices were used for RRMSE calculations separated into 3 regions (proximal, at the throat, and distal to the stenosis). There is an overlap between the slices used to calculate Q_{conv} and the slices used to calculate Q_{inlet}. We acknowledge that this overlap will introduce a positive bias for the performance measures

that were reported in Table 5 for the Cartesian acquisition. As expected, a lower RRMSE was observed in the low flow rate case of 50ml/s and higher errors were observed in distal slices at the higher flow rate of 150 ml/s. As may be seen from Table 5, more spiral interleaves lead to increased errors under all flow regimes. This is due to the oversampling of center of the k-space which overestimates the flow rate. Echo time is another parameter which affects the accuracy. Echo time is independent of the number of interleaves and is lower for higher Vencs. All post processings were performed using in-house developed code in Matlab (The Matchworks, Natick, MA).

Table 5 scan time, mean measured flow and RRMSE for Conventional 4D flow and 4D RTE spiral flow acquisitions for different flow rates at three regions: proximal, at the throat, and distal to the stenosis (see figure 56).

Q [ml/s]		50	100	150
Cartesian	Scan time [min:sec]	1:01	0:52	0:51
	Mean measured flow [ml/s]	49.62	95.94	156.62
	RRMSE Proximal [%]	0	0	0
	RRMSE Throat [%]	16.09	13.95	25.53
	RRMSE distal [%]	2.90	4.78	30.90
RTE Spiral-12	Scan time [min:sec]	0:18	0:18	0:18
	Mean measured flow [ml/s]	53.4	104.85	165.19
	RRMSE Proximal [%]	4.01	4.02	13.37
	RRMSE Throat [%]	9.89	13.65	25.46
	RRMSE distal [%]	11.52	12.57	38.15
RTE Spiral-24	Scan time [min:sec]	0:40	0:39	0:38
	Mean measured flow [ml/s]	55	105.25	155.11
	RRMSE Proximal [%]	3.71	7.33	14.60
	RRMSE Throat [%]	22.13	12.39	16.49
	RRMSE distal [%]	11.45	13.54	26.65
RTE Spiral-36	Scan time [min:sec]	0:51	0:49	0:48
	Mean measured flow [ml/s]	51.4	103.27	165.69
	RRMSE Proximal [%]	1.99	5.70	7.24
	RRMSE Throat [%]	12.09	13.13	16.26
	RRMSE distal [%]	9.70	7.23	25.54

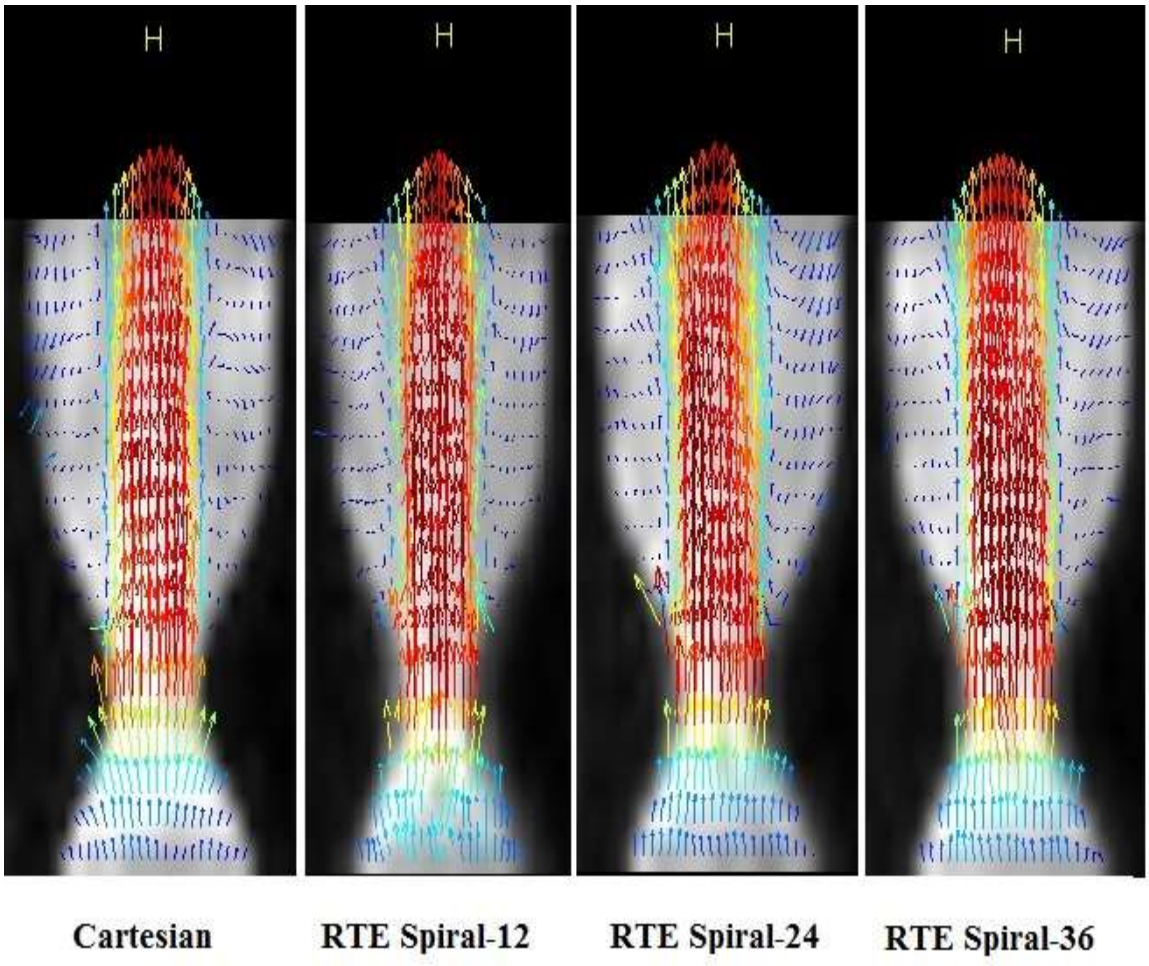

Figure 57 Sagittal view of velocity vector profile visualization at Q=50 ml/s steady flow for Conventional 4D and 4D RTE spiral acquisitions.

Figure 57 shows velocity vector profiles for Q=50 ml/s for conventional 4D and 4D RTE spiral acquisitions with 12, 24 and 36 spiral interleaves. All 4 acquisitions measured the flow with similar accuracy; however, the scan time was much shorter for the 4D RTE spiral acquisitions. Moreover, 4D RTE Spiral acquisitions permitted echo times on the order of 2 ms in comparison to 3.6 ms for the conventional 4D acquisition. In case of high flow rates and presence of intravoxel dephasing, turbulence and flow jets, 4D RTE spiral acquisitions were able to obtain better velocity profiles when compared to conventional acquisition.

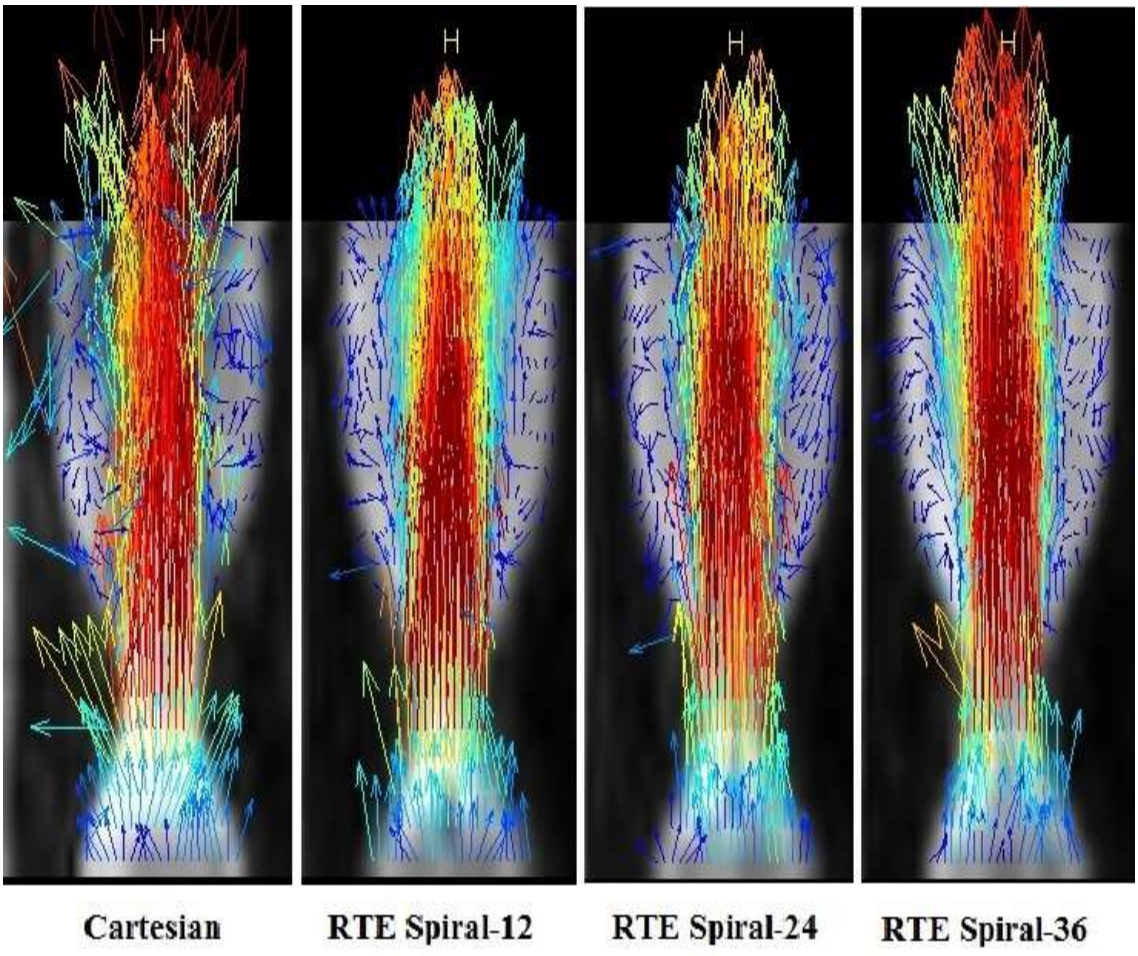

Figure 58 Sagittal view of visualization of velocity vectors at Q=150 ml/s for conventional 4D and 4D RTE spiral acquisitions.

Figure 58 demonstrates velocity vector profiles at Q=150 ml/s for conventional 4D and 4D RTE spiral acquisitions. Based on experience, if the number of spiral interleaves is appropriately chosen so that streaking artifacts are avoided, due to the inherent shorter echo times, the spiral acquisition can provide improved visualization of velocity profiles when compared against the Cartesian acquisition.

The streaking artifact in the spiral acquisition becomes prominent when the k-space is undersampled. Figure 59 (a) illustrates the streaking artifacts in an axial phantom image with 12 interleaves while (b) and (c) illustrate that by increasing the number of

interleaves to 24 and 36 results in complete removal of the streaking artifact. Based on qualitative (Figures 60-65) and quantitative results (Table 5) we can conclude that for the phantom studies, 24 interleaves strikes a balance between accuracy and scan efficiency. All studies with 24 interleaves led to acceptable RRMSE when compared to Cartesian acquisitions while achieving favorable scan times (65-75% of the scan time for conventional 4D flow).

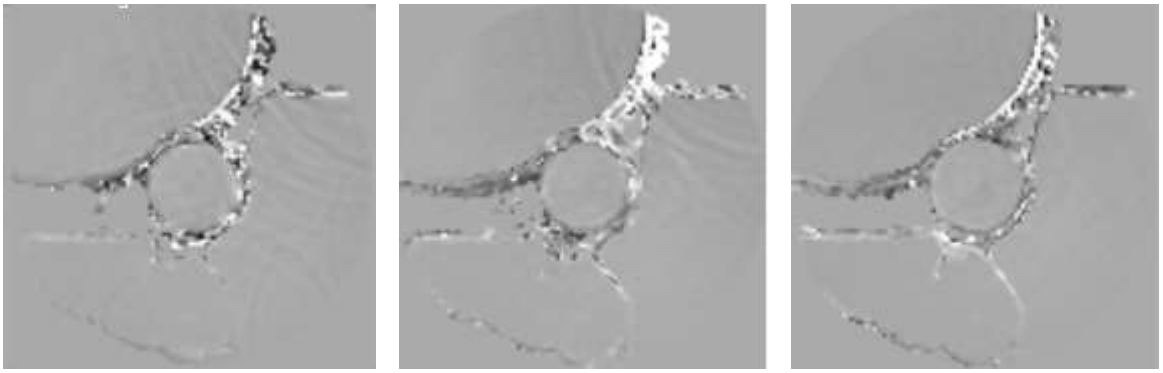

(a) (b) (c)

Figure 59 The effect of the number of interleaves on streaking artifacts at Q=50 ml/s steady flow on an axial slice located proximal to the throat of the stenosis in a reduced TE spiral 4D flow study. Reconstructed velocity image with (a) 12 spiral interleaves (b) 24 spiral interleaves and (c) 36 spiral interleaves.

4.5.2. Qualitative comparison of velocity profiles

Figures 60 and 61 display velocity profiles at mid sagittal slice and three axial slices at 12 mm Proximal to the stenosis, at the throat of the stenosis, and 21 mm distal to the throat of the stenosis for conventional 4D flow (Figure 60) and 4D RTE spiral flow (with 24 spiral interleaves) (Figure 61). There is no noticeable difference between the velocity profiles at Q=50 ml/s and results show good agreement between conventional 4D flow and 4D RTE spiral flow acquisitions. Figure 62 and 63 show velocity profiles in the same

axial and sagittal slices for Q=100ml/s. Some mild distortions are visible in velocity profiles from conventional 4D flow due to higher velocity in Figure 62.

Figures 64 and 65 display axial and mid-sagittal velocity profiles for Q=150 ml/s. Results from conventional 4D flow show flow artifacts in velocity profiles at distal locations. However the results from RTE spiral flow display a noticeable improvement when compared with the Cartesian results. This improvement is primarily due to shorter echo time of the RTE spiral acquisitions (TE= 1.57 ms) versus the longer echo time (TE=3.2 ms) for the Cartesian acquisition. The visual results in Figures 64 and 65 reaffirm the quantitative results which were reported in Table 5.

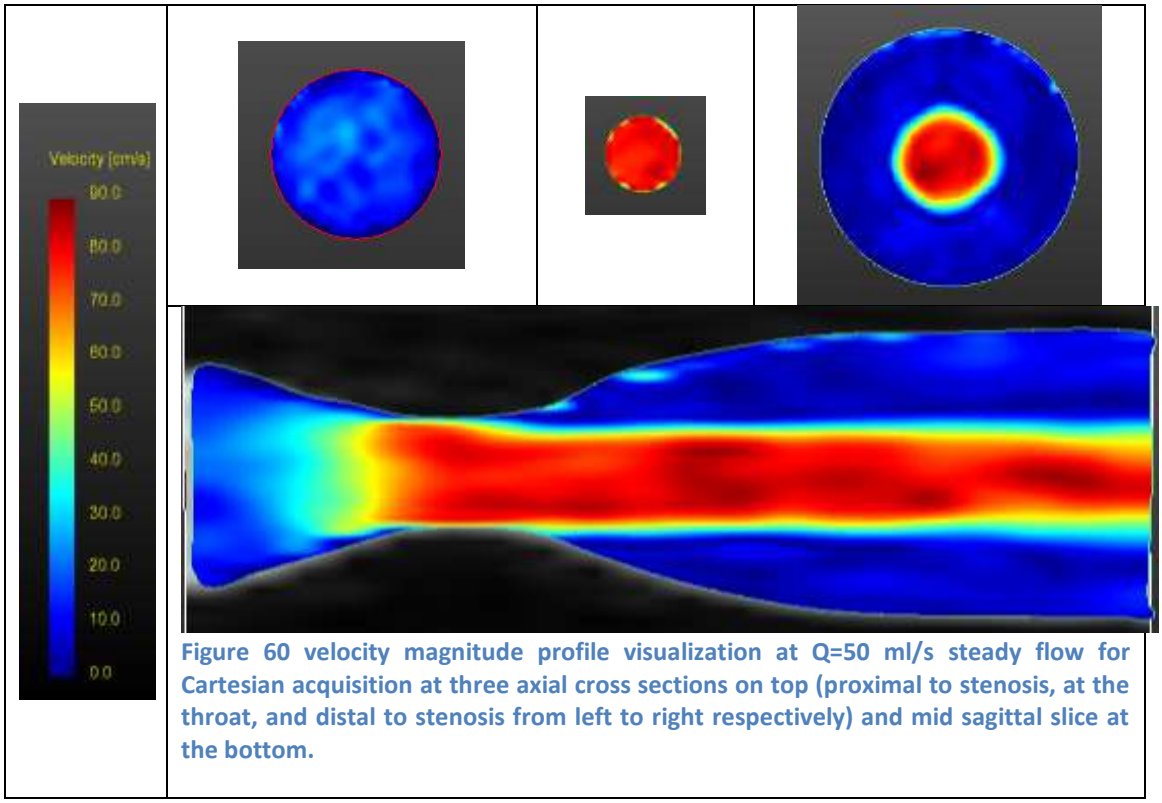

Figure 60 velocity magnitude profile visualization at Q=50 ml/s steady flow for Cartesian acquisition at three axial cross sections on top (proximal to stenosis, at the throat, and distal to stenosis from left to right respectively) and mid sagittal slice at the bottom.

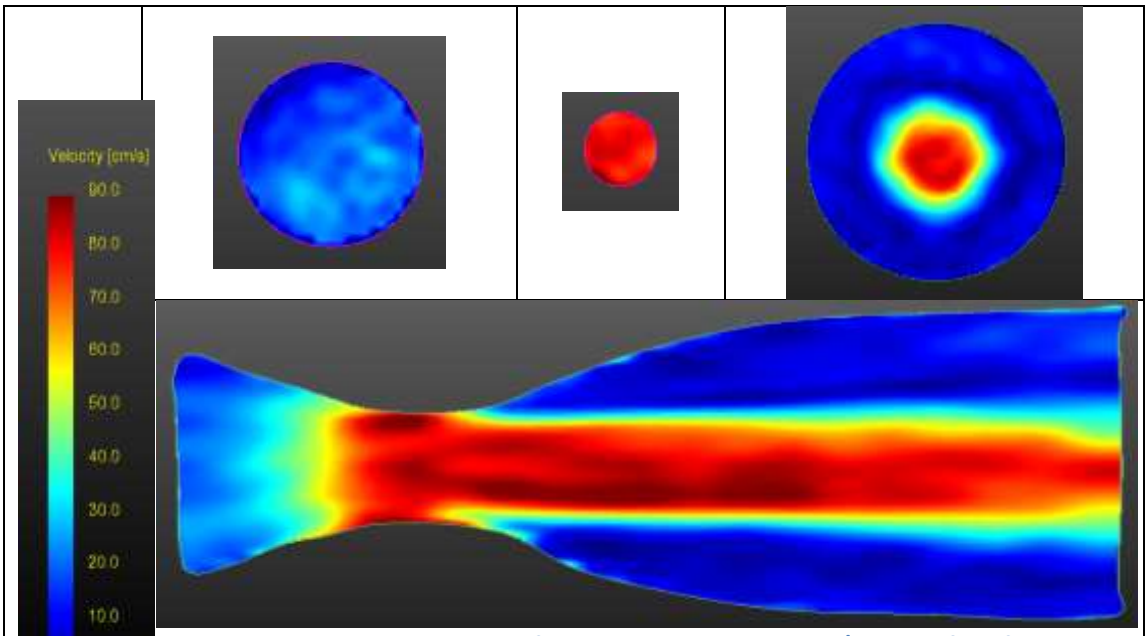

Figure 61 velocity magnitude profile visualization at Q=50 ml/s steady flow for 4D RTE spiral acquisition at three axial cross sections on top (proximal to stenosis, at the throat, and distal to stenosis from left to right respectively) and mid sagittal slice at the bottom.

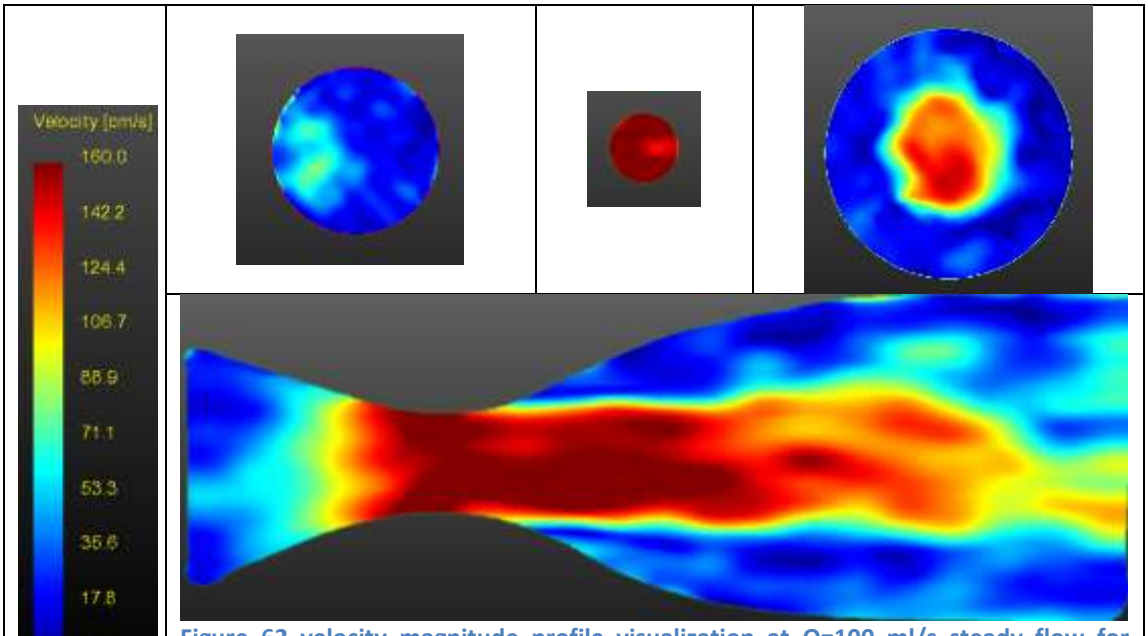

Figure 62 velocity magnitude profile visualization at Q=100 ml/s steady flow for Cartesian acquisition at three axial cross sections on top (proximal to stenosis, at the throat, and distal to stenosis from left to right respectively) and mid sagittal slice at the bottom.

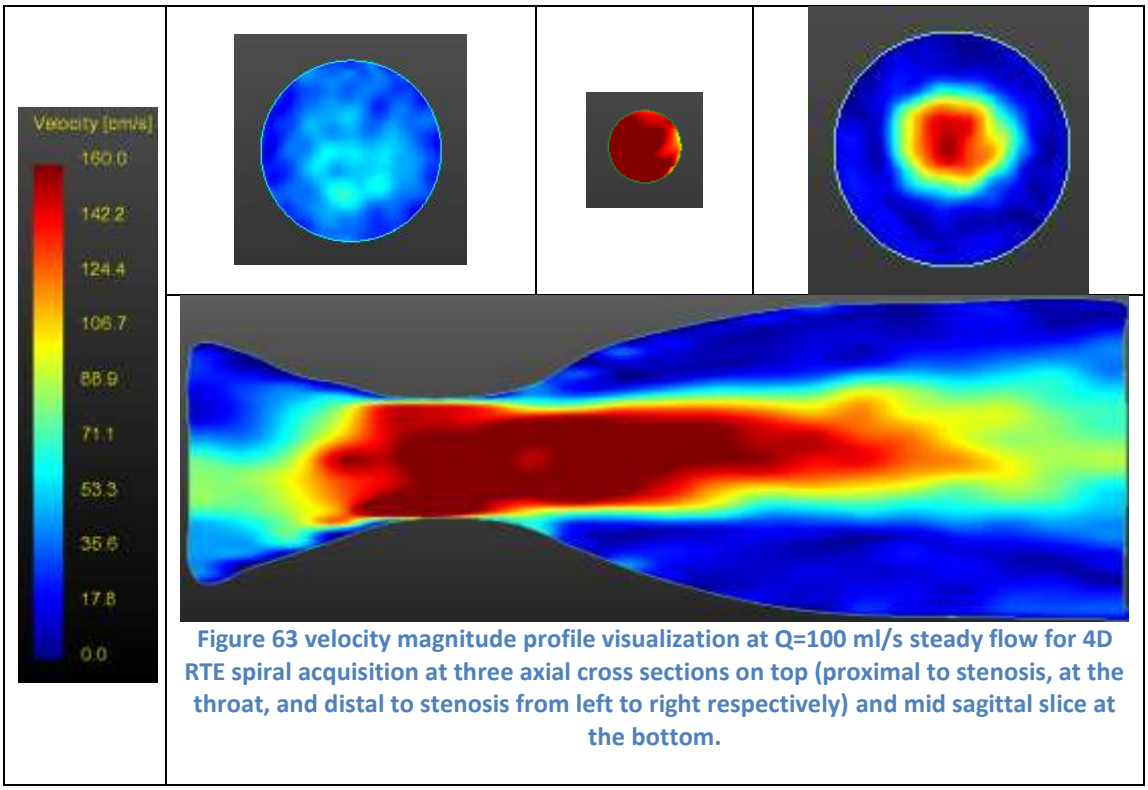

Figure 63 velocity magnitude profile visualization at Q=100 ml/s steady flow for 4D RTE spiral acquisition at three axial cross sections on top (proximal to stenosis, at the throat, and distal to stenosis from left to right respectively) and mid sagittal slice at the bottom.

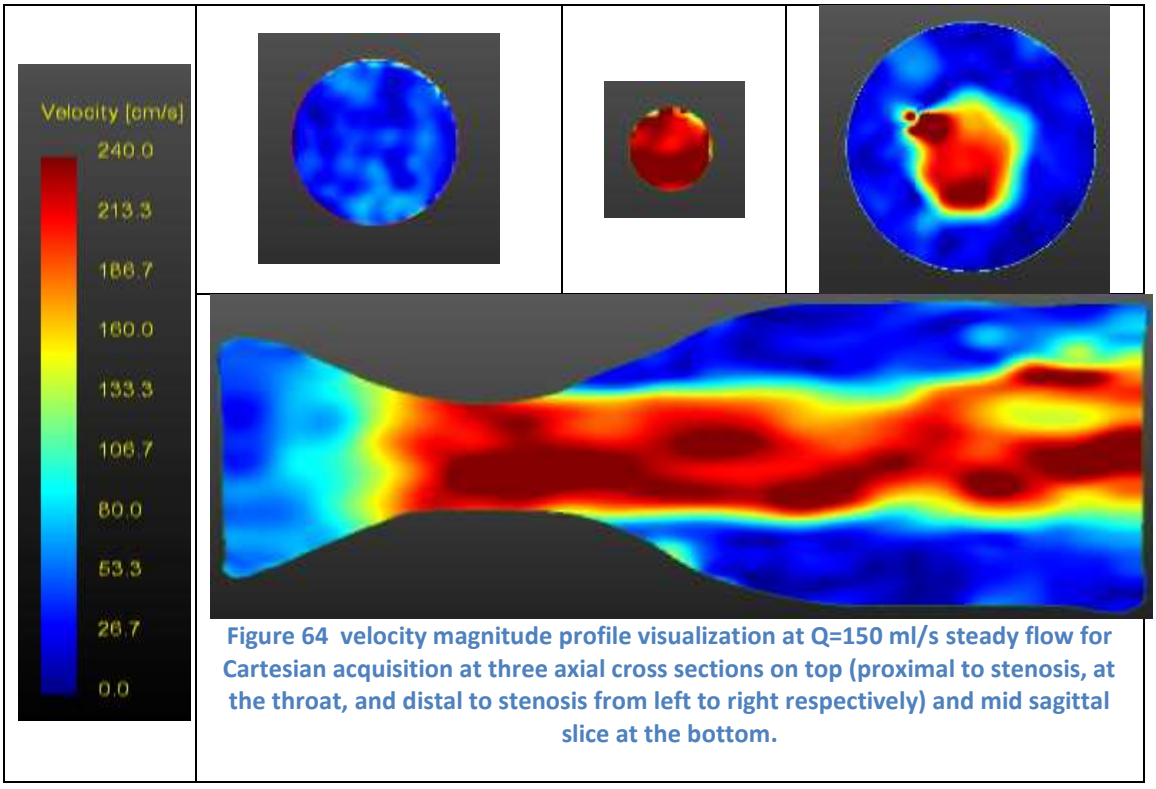

Figure 64 velocity magnitude profile visualization at Q=150 ml/s steady flow for Cartesian acquisition at three axial cross sections on top (proximal to stenosis, at the throat, and distal to stenosis from left to right respectively) and mid sagittal slice at the bottom.

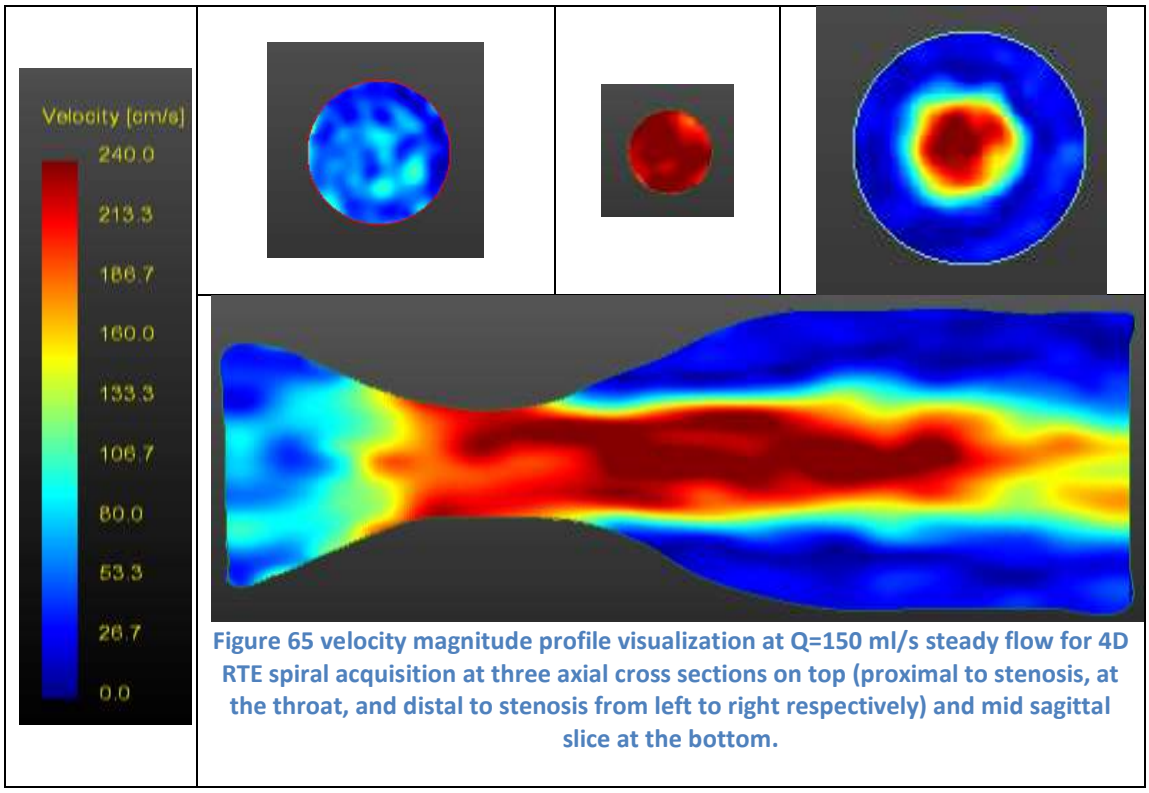

Figure 65 velocity magnitude profile visualization at Q=150 ml/s steady flow for 4D RTE spiral acquisition at three axial cross sections on top (proximal to stenosis, at the throat, and distal to stenosis from left to right respectively) and mid sagittal slice at the bottom.

4.5.3. Pulsatile Flow Experiments

Flow assessment and quantification was performed in the same phantom under pulsatile flow using both conventional 4D flow and the proposed 4D RTE spiral flow acquisition. The peak of the pulsatile flow waveform shown in figure 66 was adjusted to the value of the steady flow experiments described previously (i.e., Qmax=50, 100, and 150 ml/s) and prescribed at the pump. However it should be noted that due to compliance of tubes and flow connectors, relative to the flow waveform of Figure 66, the measured flow waveform in the phantom is damped. Figures 67-69 display the averaged damped measured flow waveforms with conventional Cartesian acquisition at 3 proximal slices a for 3 flow experiments with peak flow rates Qmax=50ml/s, Qmax=100ml/s, and Qmax=150 ml/s. It is observed that peak of flow waveforms were damped to about 55%

of prescribed value at the pump due to compliance of tubes in the flow system. For pulsatile flow acquisitions, the same imaging parameters as with steady flow acquisitions were used (see Table 6). ECG triggering from the pump was used and 15 images were acquired in each cycle.

Quantitative Comparison of Flows

A reference flow waveform was calculated by averaging the flow waveform obtained from conventional 4D flow at 3 slices proximal to the site of the stenosis. For each of the 4D RTE spiral acquisitions (i.e., with 12, 24, or 36 interleaves) and for the conventional 4D flow, the RRMSE was calculated between the measured flow and the reference flow waveforms:

$$\mathrm{RRMSE} = 100\% \times \sqrt{\frac{\sum_t \sum_n (Q_{sp/conv}(t) - Q_{inlet}(t))^2}{\sum_t \sum_n (Q_{inlet}(t))^2}} \tag{51}$$

where Q_{inlet} is average inlet flow measured with conventional 4D flow at 3 proximal slices and Qsp/conv is the measured flow using proposed 4D RTE spiral acquisition or conventional 4D flow. n is slice position through phantom length in which n=1 is the first collected slice and n=20 is last collected slice. t is time index in cardiac cycle in which t=1 the first phase and n=15 is last phase in cardiac cycle.

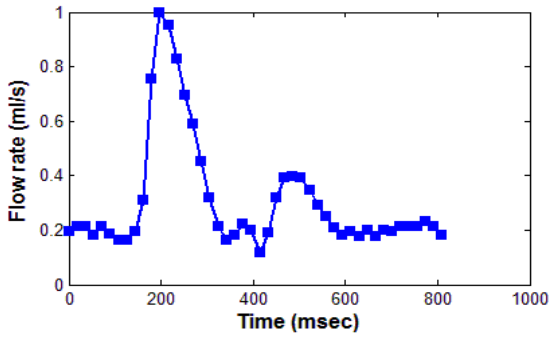

Figure 66: The normalized pulsatile flow waveform prescribed at the pump for pulsatile phantom experiments.

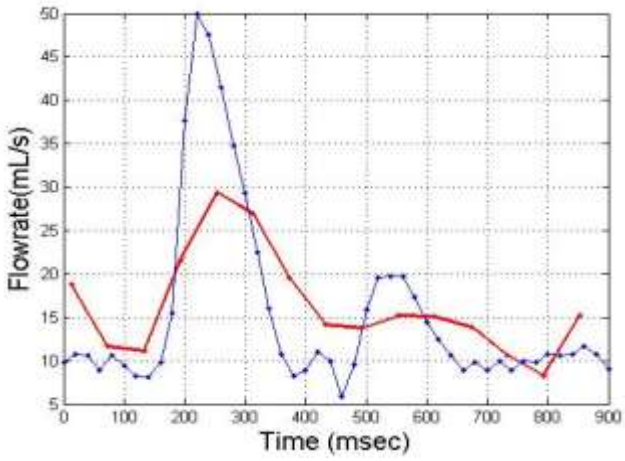

Figure 67 prescribed pulatile flow waveform of Q=50ml/s used in pulsatile study (blue). Due to the compliance of tubes and flow connectors, the measured flow waveform at the inlet becomes damped (red).

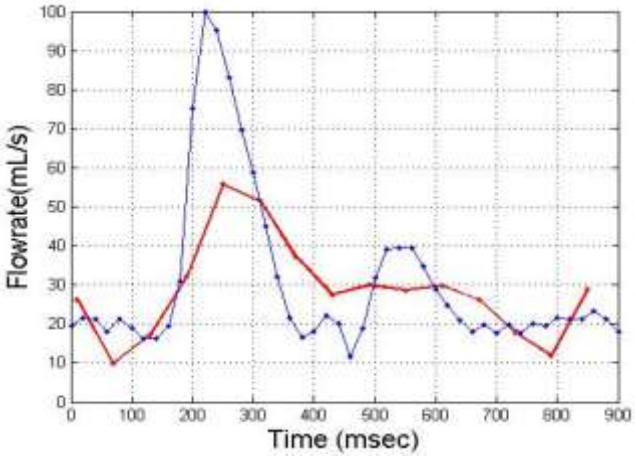

Figure 68 prescribed pulatile flow waveform of Q=100ml/s used in pulsatile study (blue). Due to the compliance of tubes and flow connectors, the measured flow waveform at the inlet becomes damped (red).

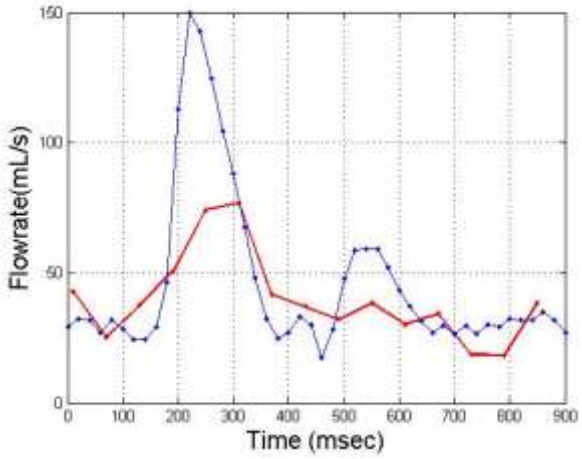

Figure 69 prescribed pulatile flow waveform of Q=150ml/s used in pulsatile study (blue). Due to the compliance of tubes and flow connectors, the measured flow waveform at the inlet becomes damped (red).

Table 6 shows scan time and the measured RRMSE between reference flow waveform and conventional 4D flow and 4D RTE spiral flow for different number of interleaves under 3 pulsatile flow waveforms (Qmax=50 ml/s, 100 ml/s, 150 ml/s) at proximal, the throat, and distal to the stenosis.

As noted earlier, using 3 proximal slices in the Cartesian acquisition to calculate the reference flow for RRMSE measurement purposes introduces a positive bias (i.e., lower errors) for the reported RRMSE measure for the Cartesian entries in Table 7. Based on the RRMSE metric, and considering that there is a positive bias for the Cartesian acquisition, we can classify the performance of the 4D RTE spiral and conventional 4D scans to be similar. In the high flow rate of 150 ml/s, RTE-spiral 36 achieved the same RRMSE as Cartesian again considering the positive bias for the Cartesian acquisition, it may be concluded that RTE spiral-36 has a better performance. RRMSE errors in 4D RTE spiral acquisition should be judged relative to Cartesian and not just by absolute value of error. Scan time is another important criterion in this table. RTE-Spiral 12, RTE-

spiral 24, and RTE-spiral 36 have scan times of 5:14, 10:62 and 7:50 respectively, in comparison to conventional Cartesian which had a scan time of 14:20.

Table 6 Scan parameters for conventional 4D flow and 4D RTE spiral acquisition with 12, 24, and 36 interleaves for a pulsatile flow phantom studies at Qmax=50 ml/s, 100ml/s and 150 ml/s flow rates. In segmented acquisition technique, segmentation factor refers to the number of acquired k-space line in each segment.

Q [ml/s]		**50**	**100**	**150**
Venc [cm/s]		150	300	450
FOV [mm]		100*100*60		
Resolution [mm]		1.5*1.5*3		
Matrix Size		68*68		
Flip angle		6^{o}		
Number of signal averages		1		
Cartesian	TE/TR [ms]	3.6 / 6.4	3.3 / 6.1	3.2 / 6.0
	Readout time [ms]	3.2	3.2	3.2
	Segmentation factor	2	2	2
	Number of phases	15	15	15
RTE Spiral-12	TE/TR [ms]	2 / 13	1.71 / 13	1.57 / 13
	Readout time [ms]	9	9	9
	Segmentation factor	1	1	1
	Number of phases	15	15	15
RTE Spiral-24	TE/TR [ms]	2 / 10	1.71 / 10	1.57 / 9.9
	Readout time [ms]	6	6	6
	Segmentation factor	1	1	1
	Number of phases	15	15	15
RTE Spiral-36	TE/TR [ms]	2 / 8.8	1.71 / 8.5	1.57 / 8.4
	Readout time [ms]	4	4	4
	Segmentation factor	2	2	2
	Number of phases	14	14	14

Note that despite having more spiral interleaves, Spiral 36 had scan time less than others spiral configurations (spiral 12 and spiral 24) due to having segmentation factor of 2, but it was still able to achieve the same number of phases because of shorter TR (Table 6). RRMSE of proximal slices for Cartesian acquisition is zero since reference scan and experiment are identical.

Table 7 Scan time and measured RRMSE (in percent error) for conventional 4D flow and 4D RTE spiral flow acquisitions for different peak flow rates.

Inlet Flow Qmax [ml/s]	Location	Cartesian	RTE Spiral-12	RTE Spiral-24	RTE Spiral-36
50	Proximal	0	9.12	13.59	16.34
	Throat	5.24	17.84	14.01	14.95
	Distal	11.96	23.75	19.08	11.81
	Scan Time (min:sec)	14:20	5:14	10:26	7:50
100	Proximal	0	23.56	26.36	28.76
	Throat	21.42	20.38	19.47	26.12
	Distal	15.92	21.91	26.00	26.40
	Scan Time (min:sec)	14:20	5:14	10:26	7:50
150	Proximal	0	38.80	31.80	20.52
	Throat	16.43	15.47	20.14	19.95
	Distal	26.82	31.09	33.40	26.81
	Scan Time (min:sec)	14:20	5:14	10:26	7:50

4.5.4. Qualitative Comparison of Flow Waveforms

As an additional comparison between the Conventional 4D flow and RTE spiral flow, the flow waveforms from both acquisitions were directly measured. Proximal: flow waveforms at 3 axial slices proximal to the stenosis were averaged, Throat: 3 axial slices at the throat of the stenosis were averaged and compared. Distal: 12 axial slices distal to the stenosis were averaged and compared. Figures 70-72 report the results for the case of low flow rate with Qmax=50 ml/s using conventional Cartesian and 3 RTE spiral acquisitions. Results show that there is good agreement in flow quantification between 4D Conventional and RTE Spiral acquisition in all 3 locations with more accuracy in proximal slices.

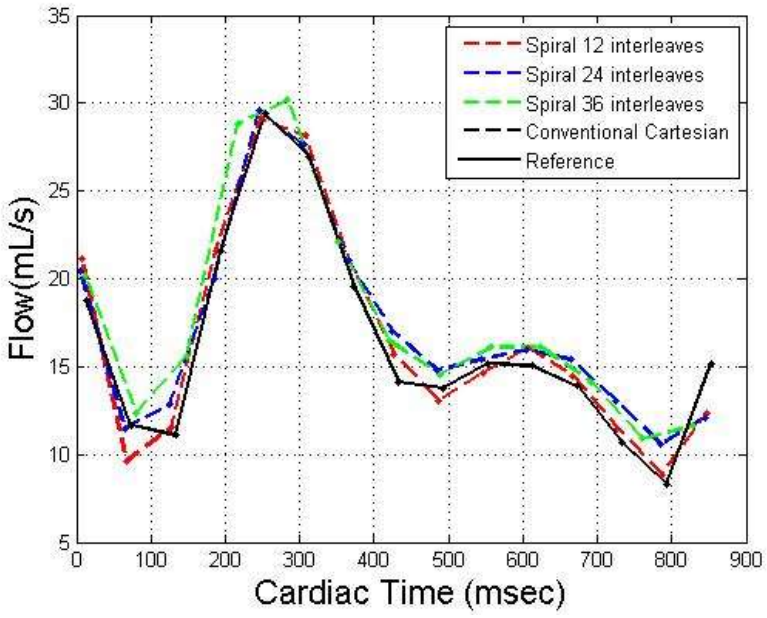

Figure 70 Mean flow waveform from 3 proximal slices for both 4D conventional and 4D RTE spiral acquisitions with Qmax=50 ml/s. In proximal slices, reference and Cartesian plots are identical.

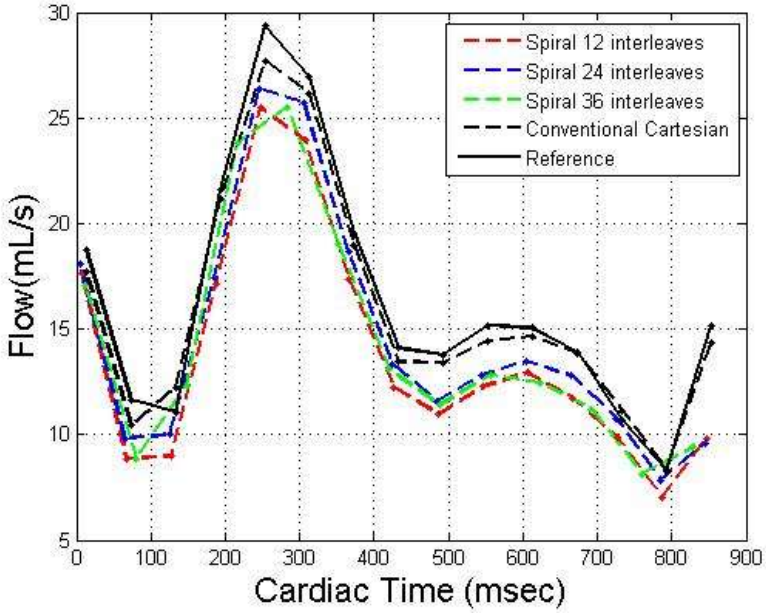

Figure 71 Mean flow waveform in 3 axial slices at the throat of the stenosis for both 4D conventional and 4D RTE spiral acquisitions with Qmax= 50 ml/s.

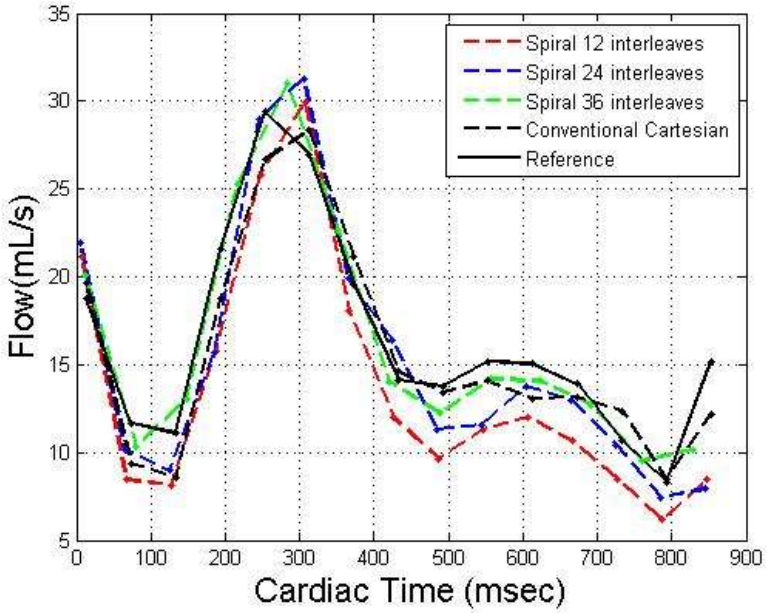

Figure 72 Mean flow waveform in 12 slices distal to the stenosis for both 4D conventional and 4D RTE spiral acquisitions with Qmax=50 ml/s.

Figure 73-75 show flow waveform for flow rate Qmax=100 ml/s using conventional 4D and three RTE spiral configurations. In proximal slices, there is good agreement between all acquisition methods, however, more discrepancies were observed at the throat and distal slices due to higher velocity and acceleration after the throat of the stenosis. Qualitatively, all methods work well with acceptable accuracy in comparison to the reference flow waveform except for 4D RTE spiral-12 acquisition at the throat of the stenosis which had more errors in the diastolic phase which can be due to off resonance.

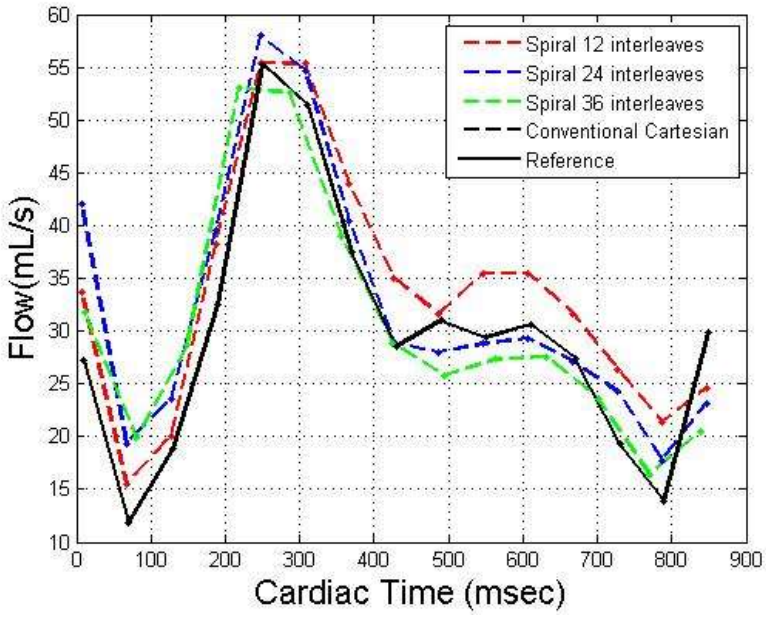

Figure 73 Mean flow waveform from 3 proximal slices for both 4D conventional and 4D RTE spiral acquisitions with Qmax=50 ml/s. In proximal slices reference and Cartesian plots are identical.

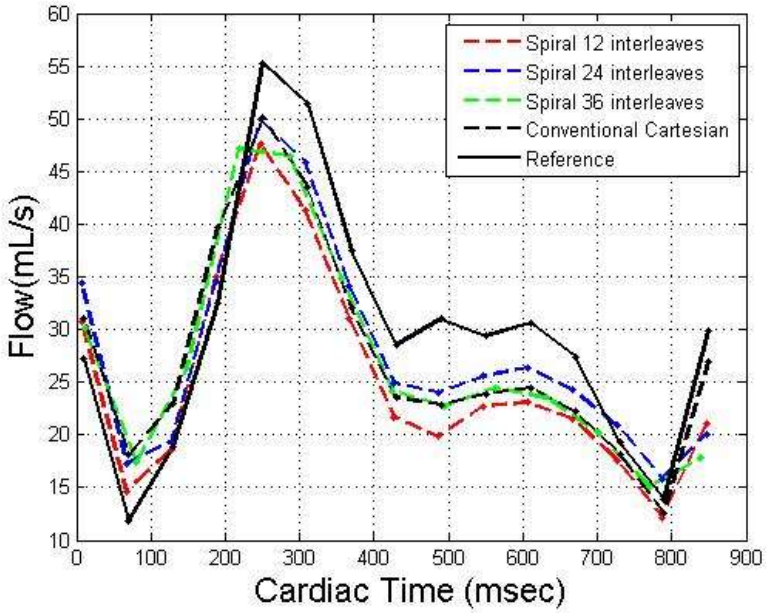

Figure 74 Mean flow waveform in 3 axial slices at the throat of the stenosis for both 4D conventional and 4D RTE spiral acquisitions with Qmax= 100 ml/s

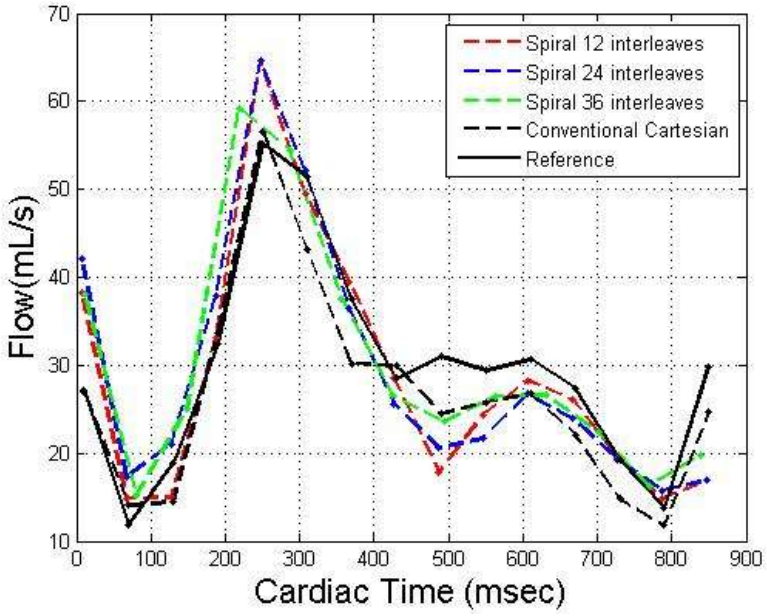

Figure 75 Mean flow waveform in 12 slices distal to the stenosis for both 4D conventional and 4D RTE spiral acquisition with Qmax=100 ml/s.

Figures 76-78 show the same visualization for pulsatile flow rate with Qmax= 150 ml/s using both conventional 4D flow and three RTE spiral acquisitions with 12, 24, and 36 interleaves. Differences between reference flow waveform and 4 other acquisition are a bit more in higher flow rate due to higher velocity fluctuation. However results are all in acceptable range based on the RRMSE criteria. Results show slightly higher degree of discrepancies in distal slices due to appearance of turbulence accelerations. The measured flow using conventional 4D flow technique results in flow discrepancy specifically in distal slices at higher flow rates in comparison to RTE spiral flow and this is mainly because of longer echo times. This discrepency is more noticeable in peak systolic time due to the existence of higher velocities leading to more signal loss and intravoxel dephasing. It should be mentioned that signal dephasing can lead to both positive phase and negative phase corresponding to positive flow or negative flow.

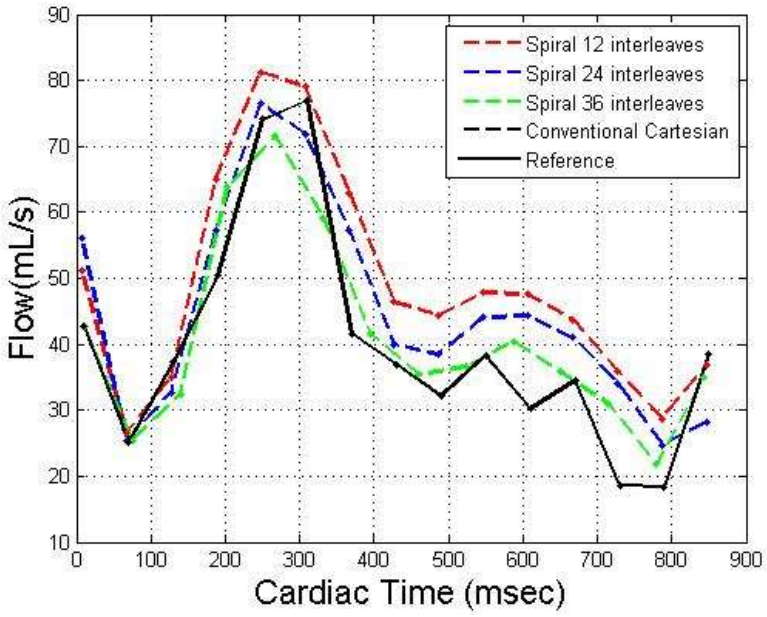

Figure 76 Mean flow waveform in 3 proximal slices for both 4D conventional and 4D RTE spiral acquisitions with Qmax=150 ml/s.

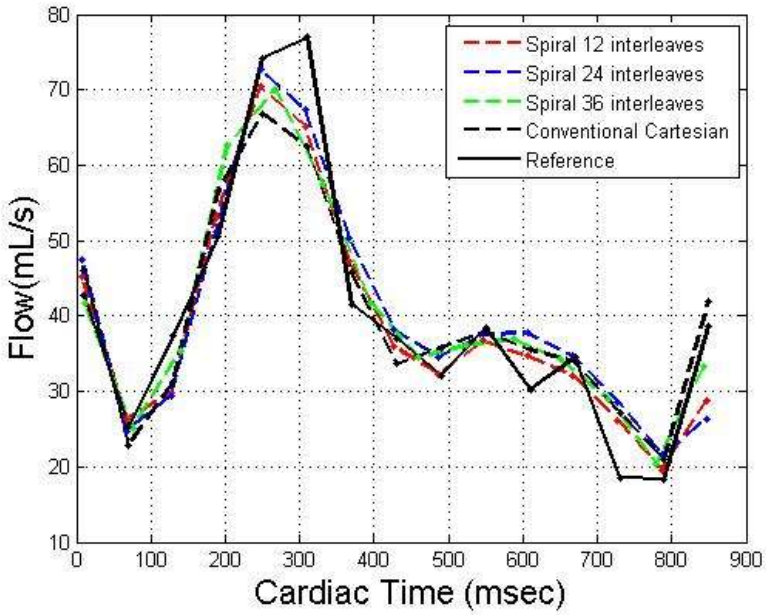

Figure 77 Mean flow waveform in 3 slices at the throat of the stenosis for both 4D conventional and 4D RTE spiral acquisition with Qmax=150 ml/s.

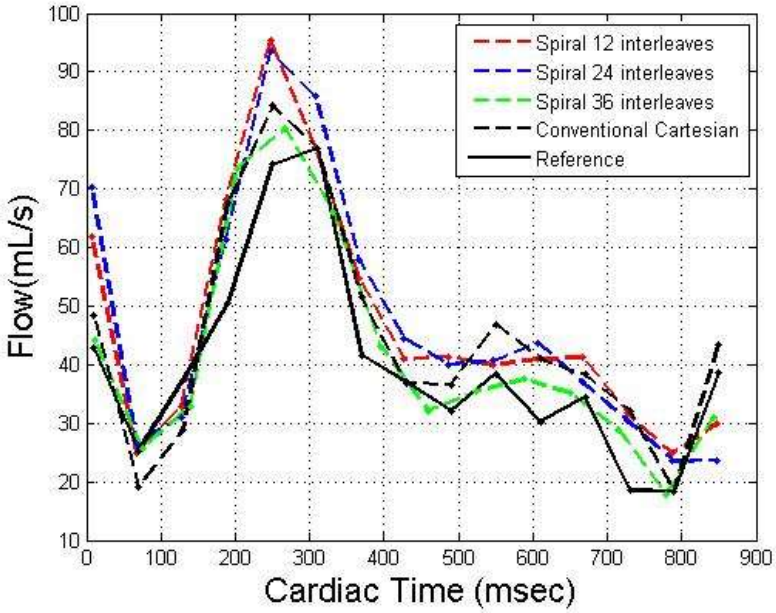

Figure 78 Mean flow waveform in 12 slices distal to the stenosis for both 4D conventional and 4D RTE spiral acquisition with Qmax=150 ml/s.

4.6. In-vivo studies

Aortic Stenosis: Aortic stenosis (AS) is a common form of valvular heart disease. When hemodynamically significant, AS may lead to left ventricular enlargement and dysfunction. It is a hemodynamically age-related progressive disease which occurs at the opening of the aortic valve with symptoms related to the degree of valvular narrowing. In the majority of people with mild to moderate stenosis, no symptoms are present. Patients with severe AS become symptomatic with syncope, chest pain, and heart failure and are at a risk of sudden cardiac death, possibly due to left ventricular hypertrophy which develops as a result of an increase in after-load. Although there are other causes of AS, the most common cause is age-related progressive calcification of the normal three-leaflet aortic valve. Echo Doppler and Catheterization are the mainstay for diagnosis. AS is classified as mild (< 25 mm Hg pressure drop, > 1.5 cm^2 area), moderate (25-40 mm Hg pressure drop, 1.0-1.5 cm^2 area), severe (> 40 mm Hg pressure drop, > 0.75-1.0 cm^2 area), and critical (> 70 mm Hg pressure drop, < 0.75 cm^2 area). Guidelines for assessment of AS severity for velocities depend on LV function, with velocities < 2 m/s with normal LV function being appropriate, while in 2-4 m/s range requiring further quantification and analysis, especially with poor LV function and finally, velocities > 4 m/s with normal LV function point to severe AS.

The clinical indications for cardiovascular MR for Aortic Stenosis disease were stated in a consensus panel report in 2004 [82]: “The low cost, flexibility, and ease of handling make transthoracic echocardiography the primary clinical tool for evaluation of valvular heart disease. Moreover Transesophageal Echocardiogram (TEE) is superior to Cardiac MR (CMR) in assessment of valve morphology and detection of small and rapidly

moving vegetation attached to the valves in endocarditis. However, CMR may play a complementary role when transthoracic acoustic windows are poor and a TEE approach is undesirable, or when results of echocardiography and catheterization are conflicting. Furthermore, CMR is a valuable tool for individual follow-up of the severity of regurgitant lesions and for quantification of the effects of valvular lesions on ventricular volumes, function, and myocardial mass …"

4.7. Prior patient studies

Several groups have reported measuring flow quantification and peak velocity, effective area of the aortic valve, and pressure gradient from PC MRI [13, 83, 84]. These studies compared PC MRI with Doppler ultrasound and revealed a good agreement between the two, but note that these were predominantly single slice studies. In [73], Sondergaards et al. studied 12 patients with AS using Doppler ultrasound and conventional 2D PC MRI with TE=3.5 msec. When compared to Doppler, in most subjects, the cardiac output were underestimated as an average of 0.2 L/minutes with range of [-0.6, +0.8] L/minutes by PC MRI. Left ventricle could be catheterized in only nine patients; in these cases, MR measured a mean valve area of 1.2 cm^2 compared with 0.9 cm^2 derived from catheterization data, with a mean difference of 0.2 cm^2 between the 2 methods. The paper concluded that MR has the potential to become a clinical tool in assessment of severity of disease in aortic stenosis.

Kilner et al., [83] studied 29 patients with aortic and mitral valve stenosis using both conventional 2D PC MRI with TE=3.6 msec and Doppler US and reported a good agreement between the two techniques in 28 patients. Mean of peak velocity at the level

of valve in AS patients was 3m/s and mean of difference between MR and echo Doppler measurement was 23 cm/s with standard deviation of 0.49 cm/s.

In another study by Caruthers et al., [85] 24 patients with aortic stenosis (ranging with a valve area from 0.5 to 1.8 cm^2) were imaged with 2D PC MRI with TE=2.9 msec and Doppler US to obtain velocity information at the level of the aortic valve. From this flow data, pressure gradients were estimated by means of the modified Bernoulli equation The correlation coefficients between modalities for peak pressure gradients were r = 0.83 and for mean pressure gradients were r = 0.87. Doppler velocity-time integral (VTI) were calculated to estimate aortic valve orifice dimensions by means of the continuity equation. The measurements of VTI correlated well, leading to an overall good correlation between modalities for the estimation of valve dimension (r=0.83). In more than half of the patients with severe AS, peak velocities were underestimated when using PC MRI.

In another study, Waters et al. studied 23 patients with mild and moderate AS using conventional 2D PC MRI with TE=2.9 msec and Doppler US at the aortic valve. The maximum observed velocity in this patient group was 2.5 m/s, which is not classified as severe stenosis. The effects of variable image position and valvular pathology on velocity measurements were also investigated in this study. Quantitative flow images were acquired in parallel planes (2 in aortic root, 2 in outflow tract), in patients with aortic stenosis. Velocity time integrals (VTIs) were computed and cross-correlations were performed between various positions. Supravalvular VTIs correlated well with one another (R = 0.96), with comparable values. The two subvalvular VTIs exhibited a linear relationship (R = 0.93) but with a 23% difference in mean values [86].

In [76] we investigated assessment and quantification of aortic stenosis hemodynamics with conventional 4D flow and 4D UTE flow. The scan parameters were as follows: spatial resolution = 2.5*2.5*5 mm3, FOV = 230*230*50, flip angle = 10, Venc = 400 cm/s, number of phases = 16, TE/TR = 3/6.9 for conventional 4D flow and TE/TR= 1.15/4.6 ms for 4D UTE MRI. For the 4D UTE sequence, 75% sampling of radial k-space lines was performed to reduce the scan time. The scan time for both 4D scans was about 4 minutes. However, due to the application of navigator gating, each scan took on the order of 10 minutes. Imaging was performed at 1.5T. Results were compared with Doppler ultrasound and showed good agreement between peak velocity at cite of aortic valve. Results show 4D UTE flow have more correlation with Doppler ultrasound in patients with peak pressure gradient > 40 mm Hg.

Conventional 4D flow MRI data acquisition with current technology suffers from long scan times in the case of high spatio-temporal resolution studies. In clinical applications, respiratory gating prolongs imaging time for up to 15-20 minutes, depending on patients' breathing pattern and scan parameters. Although 4D UTE flow gives more accurate results, it can prolong the scan times significantly. However, it is difficult for cardiac patients who by and large are elderly to lay down and hold still inside the magnet for 15 minutes, increasing the likelihood of unwanted patient movements which introduce artifacts and degrade accuracy of velocity maps. Therefore, it is important to reduce the imaging times. We believe 4D RTE spiral flow is a good technique to study patients with AS since it strikes a balance between shorter scan time and short echo time.

4.8. Protocol for Human Studies

The study was approved by the Institutional Review Board at VA Robley Rex Medical Center in Louisville, KY. Based on standard clinical protocol, and as a part of initial evaluations, patients typically undergo Doppler ultrasound of the at-risk valves. Patient selection and enrollment in this study was based on review of these initial evaluations. Inclusion criteria were: 1) Evidence of Aortic valvular disease obtained by a noninvasive study including CTA, MRA and/or Doppler with a 50-90% diameter stenosis, or regurgitation. 2) Study subjects to be in stable condition at the time of MRI study, and they should be able to lay flat for the duration of the exam (for about 1 hour). Exclusion criteria were: 1) age <20 or > 90 years old, 2) unconscious or mentally unstable patients, 3) individuals such as pregnant women, prisoners, institutionalized individuals or those unable to give informed consent, 4) patients with severe hypertension (> 200 mmHg systolic and/or 110 mmHg diastolic), 5) those weighting more than 350 lb, 6) chronic atrial fibrillation and arrhythmias precluding ECG gating, 7) claustrophobia, 8) any metallic implant including but not limited to cardiac pacemakers, defibrillator, cochlear implant, tissue expander, any aneurism clip, insulin pump, drug infusion pump, older mechanical heart valves (pre-6000 series Starr-Edward caged ball), metallic foreign bodies (such as gunshot, shrapnel, BB, ...), older orthopedic plates and screws, transdermal drug patches, penile implant or pump and prior metal fragments in the eye related to prior metal welding, or other contraindication of the MRI examination. All patients gave informed consent prior to enrolling in the study.

Five healthy volunteers and five patients with mild to moderate Aortic Stenosis were recruited to the study. The patients underwent an initial Doppler Ultrasound exam

followed immediately with both a conventional 4D flow and 4D RTE spiral flow MRI exams back-to-back. However, the healthy volunteers only underwent the MRI portion of the protocol. The demographics for both groups of volunteers are provided in Table 8.

Table 8 Demographic information for all healthy volunteer and patient subjects.

Subject number	Gender	Weight (Kg)	Age
Volunteer 1	Male	78	32
Volunteer 2	Male	63	31
Volunteer 3	Male	70	30
Volunteer 4	Male	76	42
Volunteer 5	Male	70	28
Patient 1	Male	94	70
Patient 2	Male	96	67
Patient 3	Male	90	65
Patient 4	Female	--	53
Patient 5	Male	101	89

Doppler Ultrasound

At the Robley Rex Veterans Affairs Medical Center echocardiography laboratory, transthoracic echocardiography was acquired with an iE33 commercially available echocardiography system (Philips Health Care, Best, The Netherland) using a S5-1 transducer (2-4 mHz for 2-Dimensional imaging and 1.9 mHz for spectral Doppler imaging). Doppler images were performed at a minimal sweep speed of 100 mm/sec to achieve an acquisition rate (or frame rate) of 200/sec. Two-dimensional images of the aortic valve and left ventricular outflow tract were obtained from the parasternal long-axis and apical 5-chamber views. Continuous wave Doppler of aortic valve velocity was obtained from the apical, suprasternal notch and right parasternal windows. Pulsed wave

Doppler was obtained of the left ventricular outflow tract from the apical 5-chamber view. All images were digitally recorded.

Continuous wave Doppler of aortic valve yielding the highest peak velocity was analyzed. Peak and mean aortic valve velocities were obtained. Peak and mean gradients were obtained by the modified Bernoulli method. Aortic valve and left ventricular outflow tract velocity-time integrals were measured. Left ventricular outflow tract diameter was measured at peak systole immediately below the aortic valve hinge points and outflow tract area calculated assuming it to be a circular shape. Aortic valve area was calculated by the continuity equation using velocity-time integrals. All measurements were obtained in triplicate and averaged.

MRI

MRI examinations were performed on a 1.5T Achieva Philips scanner using a dedicated 5 channel SENSE cardiac coil. The patient was positioned supine in standard clinical fashion on the MRI table and standard ECG signal was obtained during imaging for the purpose of gating. Additionally, to mitigate the effect of breathing artifacts on imaging, respiratory gating with navigator echoes was undertaken. Several scans were performed to determine the orientation of heart and aortic valve. The imaging volume was adjusted so that the aortic valve was located proximal to the center of the volume and slices were perpendicular to aortic root in the left-ventricular outflow tract (LVOT). Figure 79 shows location of 3D imaging volume in the LVOT slice planning scan. Ten contiguous slices were included in each 4D scan, each with a slice thickness of 5 mm. Other imaging parameters were as follows: Venc= 400 cm/s in all three flow directions, flip angle= 6

degrees, spatial resolution= 2.5*2.5*5.0 mm. Depending on the size of subject, FOV in the in-plane direction was enlarged but the 50 mm in the through plane direction was kept constant for all subjects. 15 Cine cardiac phases were collected in each cardiac cycle.

To design the 4D RTE spiral configuration, about 70% of the total scan time for one Cartesian acquisition was divided by the number of planned interleaves. In our Cartesian Sequence, for predefined spatial resolution and FOV of 200*200*50 mm, and for a heart rate of 60, the scan time is 323 seconds. The total scan time for the 4D RTE spiral acquisition was calculated to be 0.70*323 = 226.1 seconds. We adopted 36 interleaves with 4 msec per read-out for each interleave, leading to total scan time of 224 seconds.

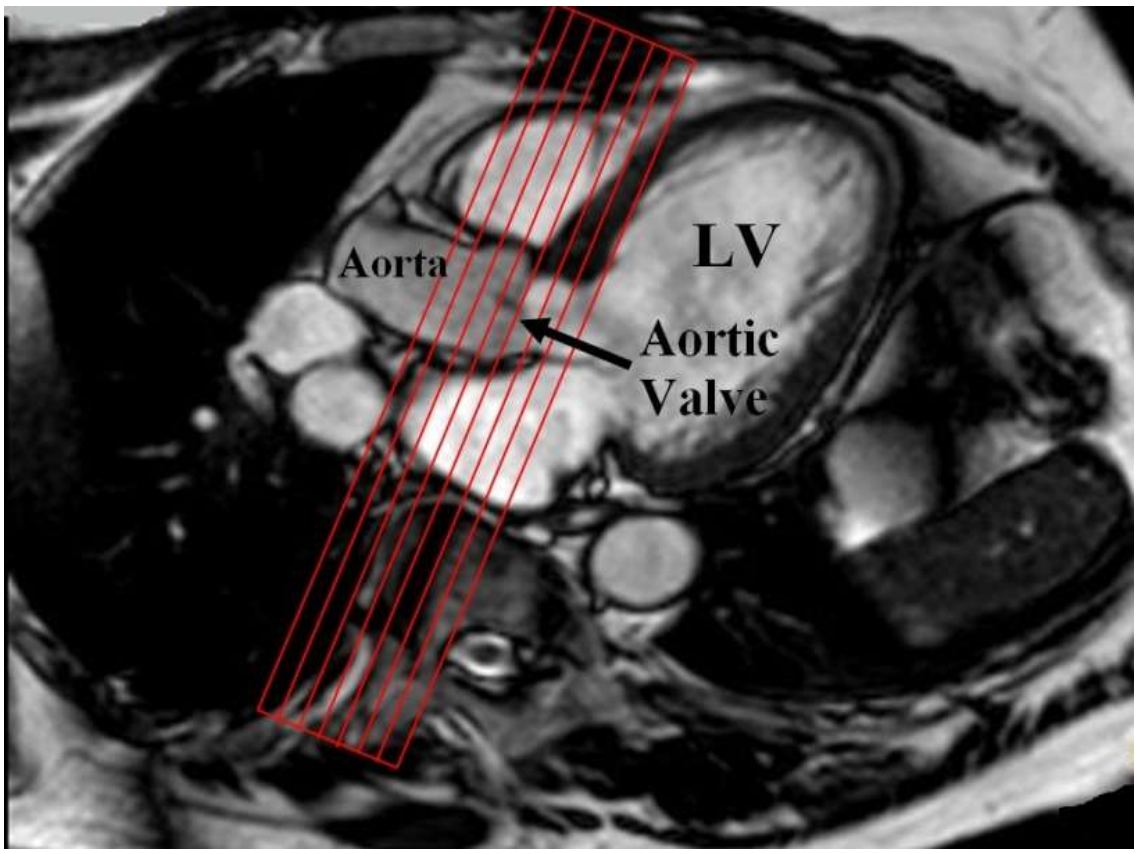

Figure 79 Left Ventricular out-flow tract showing sagittal view of the aortic valve used to accurately set up the imaging volume perpendicular to the aortic root.

Table 8 reports the imaging parameters for both conventional 4D and 4D RTE spiral scans. As may be seen, all relevant imaging parameters were kept identical between the two scans. However, there is a 45% reduction in echo time and 30% reduction in scan time with the proposed 4D RTE spiral acquisition in comparison to the conventional 4D. For the typical patient, the scan time for the conventional method was on the order of 15-25 minutes versus 10-15 minutes for the proposed 4D RTE spiral method.

Table 9 Scan parameters and scan time for conventional 4D and 4D RTE spiral acquisitions for in-vivo studies.

Protocol	4D Conventional	4D RTE Spiral
Field of View [mm]	200*200*50	200*200*50
Resolution [mm]	2.5*2.5*5	2.5*2.5*5
Matrix size	80*80	80*80
Venc [cm/s]	400	400
Number of phases	15	15
Flip Angle	6	6
Number of signal averaging	1	1
Segmentation factor (TFE)	3	2
Repetition time –TR- [ms]	5.1	7.7
Echo time – TE- [ms]	2.9	1.68
Readout time [ms]	2.1	4
Scan time [min:sec]	5:23	3:44
Number of interleaves / phase encoding steps	80	36

4.9. Data analysis

Subsequent to data acquisition, anonymized data were transferred to the Medical Imaging Lab at the University of Louisville, for post processing. All the post-processing and the flow assessments were performed using Matlab (The Mathworks, Natick, MA). The first step in data analysis involved delineation of the region of interest (ROI). The aortic valve and the aorta were segmented manually in each slice and in each cardiac phase. Due to the pulsation of the aorta, the shape, area, and position of vessel contours varied in each time frame. In each patient flow waveform, peak velocity, time to peak AV, AV Eject time, and LVOT diameter were measured and statistically compared with Doppler echo. LVOT diameter was measured in two directions using MRI data and the average of the two measurements was reported for comparison to Doppler. Flow waveform was calculated by integrating the through-plane velocity component in an axial slice at the level of aortic valve in all cardiac phases. It should be noted that in all subjects flow was measured at the level of the aortic valve. However, depending on whether the patient had AR or AS, the peak velocity occurred either proximal or distal to the valve. Time of AV peak, which is the time at which maximum out flow through the aortic valve occurs relative to beginning of the heart cycle (R-wave in ECG signal), and the AV eject time during which the valve is open, and the LV ejects blood into the Aorta, were determined from the calculated flow waveform of flow through the aortic valve; however, because of the lower temporal resolution in MR experiments (about 50-60 ms), the times measured are not as accurate as Doppler which has a much higher temporal resolution. Peak velocity was determined by examining the velocities in a slice at the level of the aortic valve and all slices distal to the aortic valve in all phases. From the peak velocity, one can

calculate the maximum pressure gradient across the aortic valve, a measure commonly used in clinical echocardiography as an indicator of AS severity, using the simplified Bernoulli equation.

4.10. In-vivo results

4.10.1. Healthy Volunteers

For all subjects, Table 10 reports the measured parameters for both MRI acquisition techniques. As may be seen, there is a very good agreement between conventional 4D flow and 4D RTE flow in measurement of LVOT diameter (RRMSE = 3.66%). Also both methods result in very close values for "AV eject time" (RRMSE = 3.94%) and "time to peak AV" (RRMSE = 1.64%).

Peak velocity and average flow columns show that Conventional 4D flow underestimates peak velocity and average flow relative to 4D RTE spiral flow which can be due to longer echo times in the Cartesian acquisition leading to underestimation of- high velocities at peak systolic time. In addition oversampling of the center of the k-space in 4D RTE spiral flow relative to Cartesian induces a positive bias in velocity value and subsequently in flow profiles, leading to higher velocities than the actual velocities present.

Figures 80-84 display flow versus cardiac time for 5 healthy volunteers at the level of aortic valve (left column) and at the level 15mm distal to the aortic valve (right column) using both conventional 4D flow MRI (blue plot) and 4D RTE spiral flow MRI (red plot). Qualitatively, there is good correlation between the two MRI techniques in flow measurement for all healthy subjects. However, 4D RTE spiral flow MRI slightly overestimates flow when compared to conventional 4D flow MRI, except in subject one

and only at the peak systolic time where conventional 4D flow MRI measured the flow rate to be 7% higher than that measured by 4D RTE spiral flow MRI. It is interesting to note that in volunteer 3, the first cardiac phase has as high a flow rate as the flow rate at the peak systolic time.

Table 10 Measured parameters using conventional 4D flow and 4D RTE spiral flow in five healthy volunteers. The average flow refers to the flow measured during the R-R interval and averaged over the number of time points. Peak velocity is the peak systolic velocity measured during the cardiac cycle. Time to peak AV is the time from the first image (slightly after on-set of the R wave) to peak measureable systolic velocity. AV eject time is the effective systolic time measured. LVOT is the diameter of the left-ventricular out flow tract. Please see text for additional details.

Volunteer number	MRI Modality	Average Flow (ml/s)	Peak Velocity (cm/s)	Time to Peak AV (ms)	AV Eject Time (ms)	LVOT Diameter (cm)
1	Conventional 4D	68.16	168	97	320	3.05
	4D RTE spiral	79.17	180	97	320	3.15
2	Conventional 4D	55.28	132	95	300	2.43
	4D RTE spiral	65.14	161	93	310	2.68
3	Conventional 4D	79.89	139	94	300	2.65
	4D RTE spiral	94.5	139	93	320	2.60
4	Conventional 4D	71.9	142	80	280	2.85
	4D RTE spiral	85.02	168	77	300	2.80
5	Conventional 4D	69.15	179	94	270	2.45
	4D RTE spiral	90.23	184	93	280	2.40

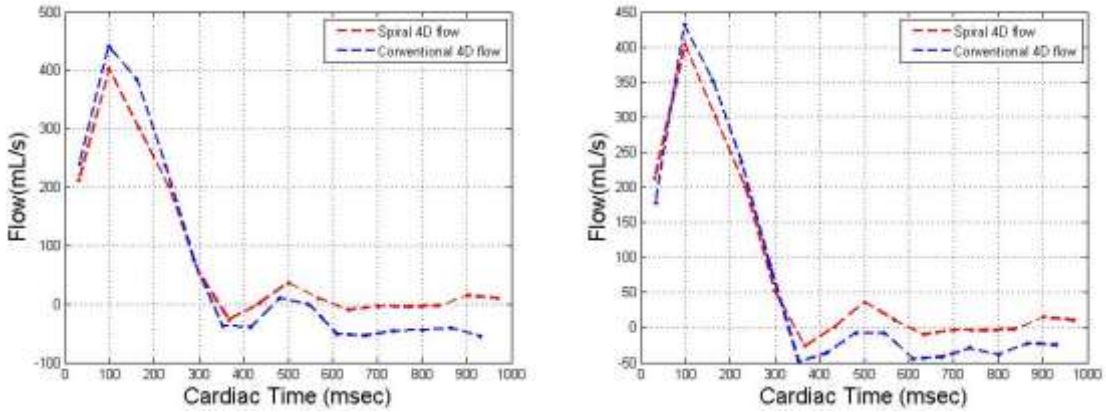

(a) (b)

Figure 80 Flow waveform versus time at the level of the aortic valve (a), and 15 mm distal to the aortic valve (b) in volunteer 1, using conventional 4D flow (blue plot) and 4D RTE spiral flow (red plot).

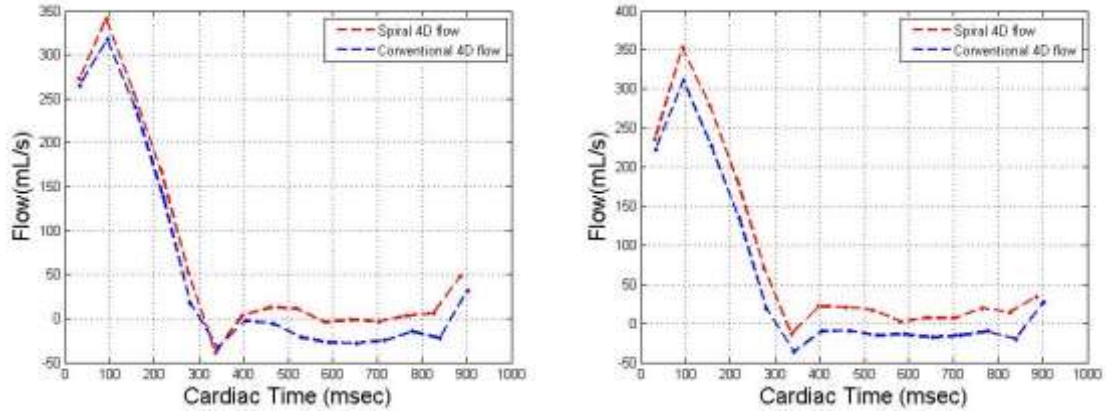

(a) (b)

Figure 81 Flow waveform versus time at the level of the aortic valve (a), and 15 mm distal to the aortic valve (b) in volunteer 2, using conventional 4D flow (blue plot) and 4D RTE spiral flow (red plot).

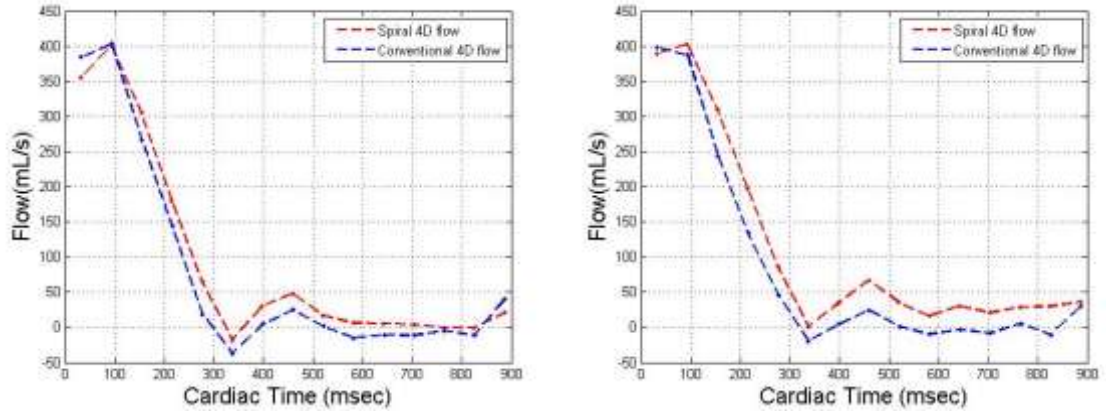

(a) (b)

Figure 82 Flow waveform versus time at the level of the aortic valve (a), and 15 mm distal to the aortic valve (b) in volunteer 3, using conventional 4D flow (blue plot) and 4D RTE spiral flow (red plot).

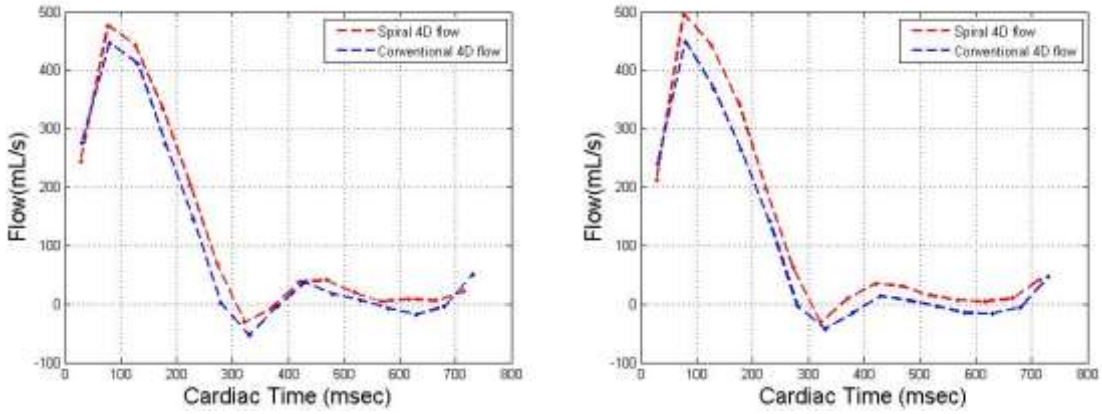

Figure 83 Flow waveform versus time at the level of the aortic valve (a), and 15 mm distal to the aortic valve (b) in volunteer 4, using conventional 4D flow (blue plot) and 4D RTE spiral flow (red plot).

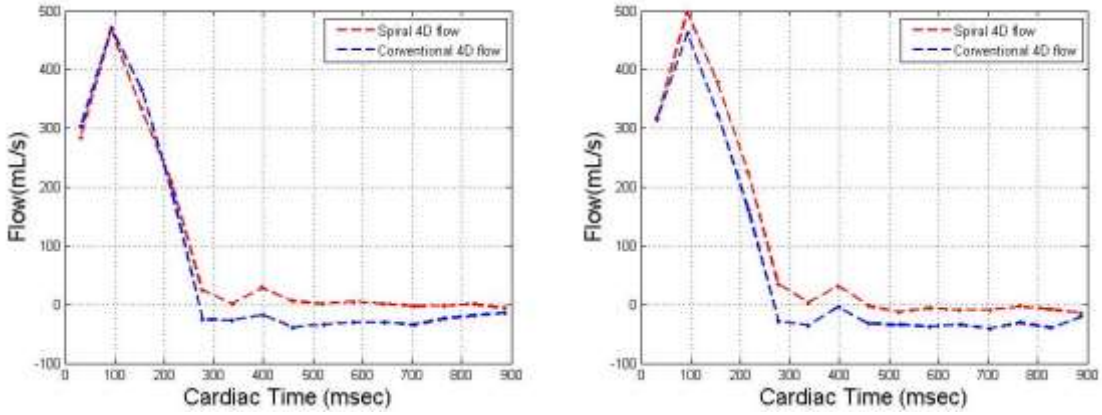

Figure 84 Flow waveform versus time at the level of the aortic valve (a), and 15 mm distal to the aortic valve (b) in volunteer 5, using conventional 4D flow (blue plot) and 4D RTE spiral flow (red plot).

In all subjects, both conventional 4D flow and 4D RTE spiral flow resulted in close values for AV eject time and the LVOT diameter. Figure 85 shows the Bland-Altman plot for AV eject time in 5 subjects using both conventional 4D flow and 4D RTE spiral flow. As may be seen from the plot, the two methods resulted in very close values (bias = -12.5 ms, agreement limits = -31.26 to 6.26 ms). Figure 86 shows Bland-Altman plot for LVOT diameter measurement using the two techniques (bias = -0.06 cm, agreement limit = -0.34 to 0.21 cm). Figure 86 indicates that the two MRI techniques result in very close values for the LVOT diameter.

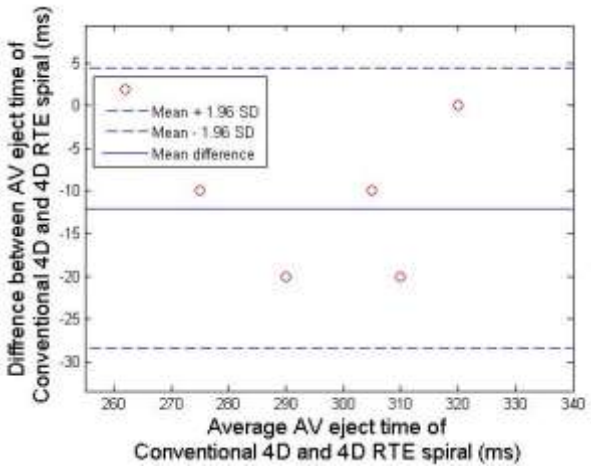

Figure 85 Bland–Altman plot of measured AV eject time at the aortic valve in 5 volunteers, demonstrating AV eject time differences versus mean AV eject time between conventional 4D flow and 4D RTE spiral flow.

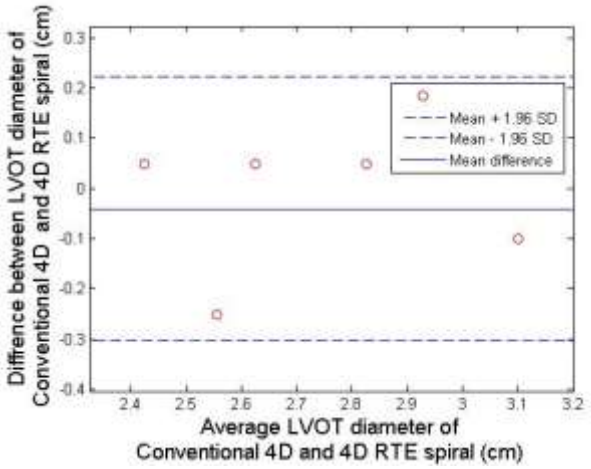

Figure 86 Bland-Altman analysis of LVOT diameter measured at the Aortic valve in 5 volunteers using conventional 4D flow and 4D RTE spiral flow.

Figures 87-91 show the 3D velocity profile and 2D velocity magnitude (inset) of flow through the aortic valve at the peak systolic time in 5 healthy volunteer using conventional 4D flow MRI (top row) and 4D RTE spiral flow MRI (bottom row). Results illustrate that both techniques can display the shape of the aortic valve in peak systolic time. In summary, the healthy volunteer results in this section showed acceptable performance of both techniques when imaging healthy subjects having peak systolic velocities less than 2 m/s.

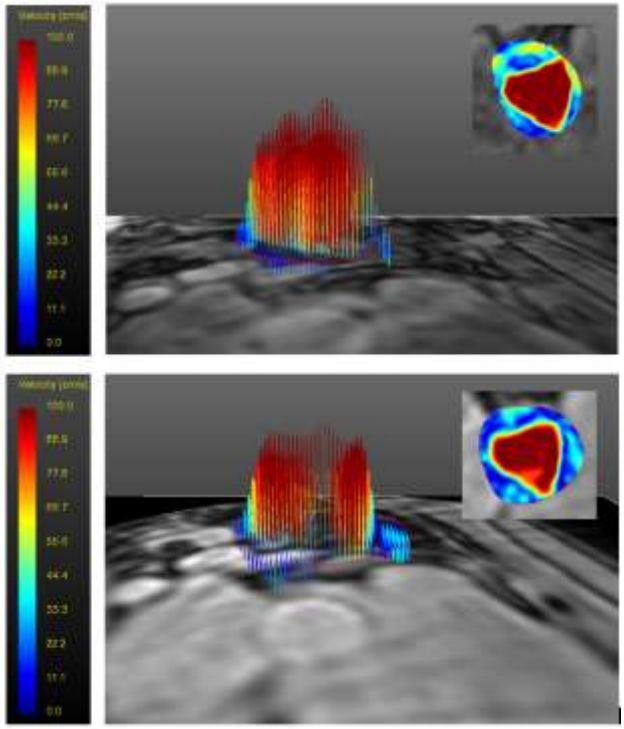

Figure 87. Velocity profiles in both 3D and 2D views (inset) in volunteer 1 using Conventional 4D flow (top) and 4D RTE spiral flow (bottom).

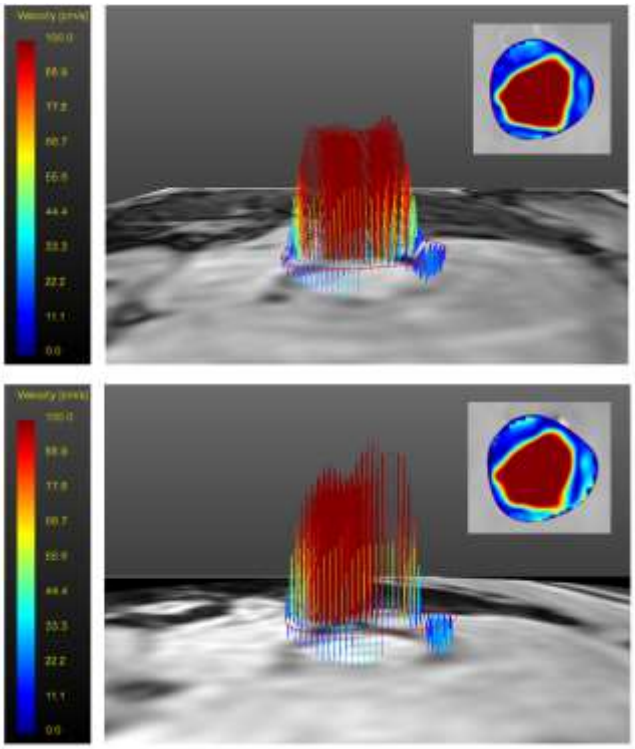

Figure 88. Velocity profiles in both 3D and 2D views (inset) in volunteer 2 using Conventional 4D flow (top) and 4D RTE spiral flow (bottom).

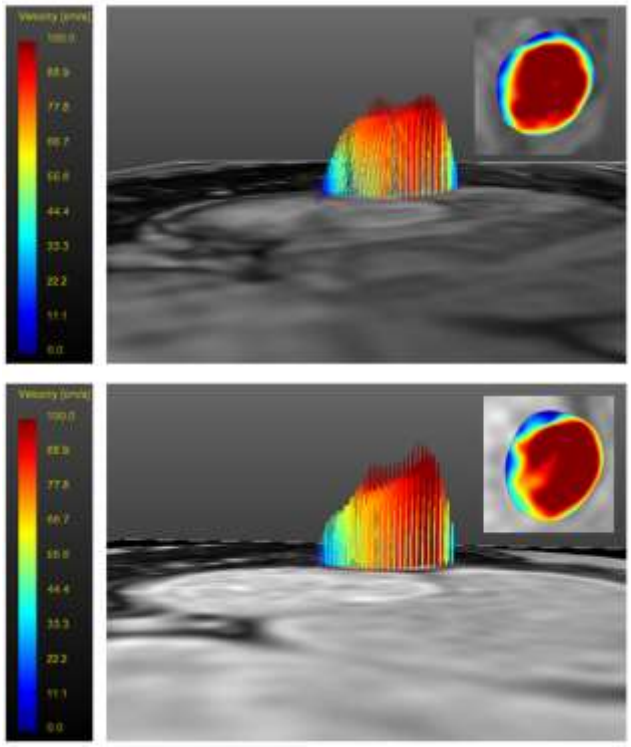

Figure 89. Velocity profiles in both 3D and 2D views (inset) in volunteer 3 using Conventional 4D flow (top) and 4D RTE spiral flow (bottom).

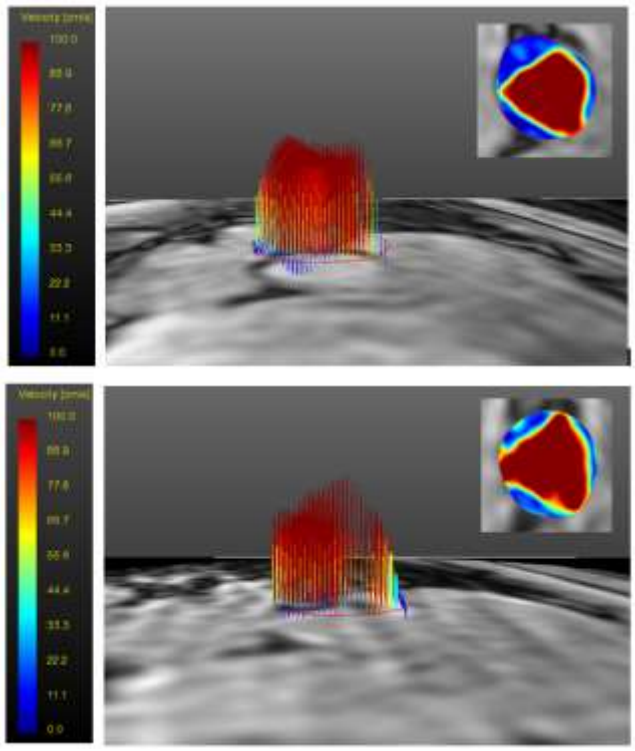

Figure 90. Velocity profiles in both 3D and 2D (inset) views in volunteer 4 using Conventional 4D flow (top) and 4D RTE spiral flow (bottom).

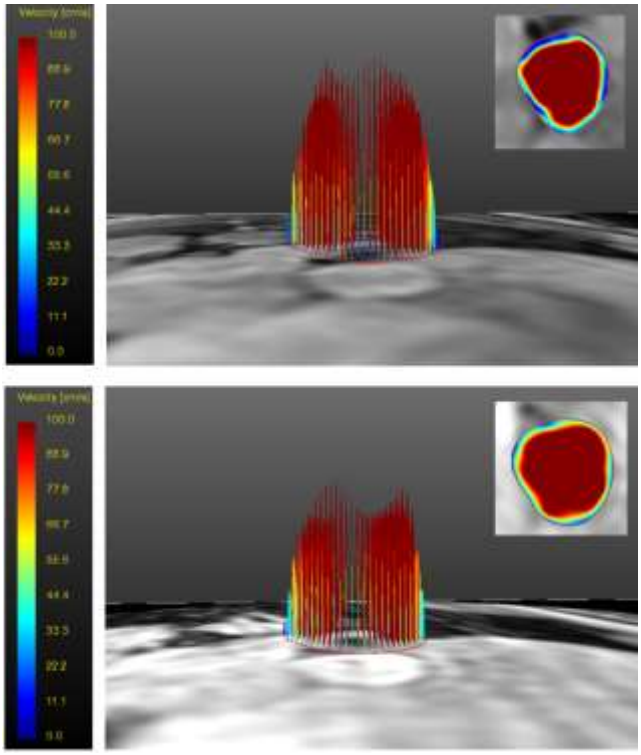

Figure 91. Velocity profiles in both 3D and 2D (inset) views in volunteer 5 using Conventional 4D flow (top) and 4D RTE spiral flow (bottom).

4.10.2. AS patient Study

In this section, performance of the conventional 4D flow and 4D RTE Spiral Flow techniques are compared when imaging subjects with aortic stenosis or regurgitation. Five patients with mild to moderate disease were scanned using both conventional 4D flow and 4D RTE spiral flow. The subjects were also scanned with Doppler ultrasound immediately prior to MRI. Table 10 shows the calculated parameters (for a description, please see previous section) using conventional 4D flow, 4D RTE Spiral flow, and Doppler US for all patients. The peak velocity measured using both conventional 4D flow and 4D RTE spiral flow MRI demonstrated good agreement with Doppler US in all subjects. The Relative Root Mean Squared Error (RRMSE) metric was calculated

between peak velocity from the two MRI methods and Doppler US. The RRMSE average over 5 AS subjects showed 5.99% error for 4D RTE spiral flow vs. 8.04% for conventional 4D flow. This indicates that on average, 4D RTE spiral flow measures peak velocities with a slightly higher accuracy. The maximum pressure gradient is a major clinical index which is commonly used to ascertain the severity of disease in patients with aortic stenosis. The last column in table 10 reports on the maximum pressure gradient in peak systolic time as calculated using the simplified Bernoulli equation.

Table 11. The measured parameters using conventional 4D flow and 4D RTE spiral flow in five patients with mild to moderate aortic stenosis.

Patient	Modality	Slice	Average Flow (ml/s)	Peak Velocity (cm/s)	AV Time to Peak (ms)	AV Eject Time (ms)	LVOT Diameter (cm)	Max pressure gradient
P1 (AR)	Conventional	4	164	414	159	350	3.3	69
	4D RTE	4	128	485	159	350	3.2	94
	Doppler	AV	---	449	--	--	2.0	81
P2 (AS)	Conventional	4	77.5	252	95	325	2.7	25
	4D RTE	4	88.6	266	95	330	3.0	28
	Doppler	AV	---	278	140	325	2	31
P3 (AS)	Conventional	3	75.26	366	154	370	3.05	54
	4D RTE	3	79.62	385	154	370	3.05	59
	Doppler	AV	---	391	125	340	2.3	61
P4 (AS)	Conventional	4	63.61	242	94	320	2.3	23
	4D RTE	4	62.23	240	94	310	2.4	23
	Doppler	AV	---	217	100	320	2.0	19
P5 (AS)	Conventional	4	41.82	278	94	315	3.1	31
	4D RTE	4	57.20	277	93	335	2.8	31
	Doppler	AV	---	293	95	280	2.5	35

Figures 92-96 display flow versus time for the five patients with AS/AR at the level of aortic valve (left column) and at a level 15mm distal to the aortic valve (right column) using both conventional 4D flow (blue plot) and 4D RTE spiral flow (red plot). Qualitatively, in patients 2, 3 and 4 there is very good correlation between the two MRI techniques in flow quantification. In subject 1, both at the level of the valve as well as in the slice 15 mm distal to the valve, and in subject 5 in the slice 15 mm distal to the slice, discrepancy in flow waveforms between the two techniques becomes more noticeable. In subject 2, both MRI techniques report almost identical values for flow in peak systolic time. In general, for all patients, 4D RTE spiral flow MRI slightly overestimates flow when compared to conventional 4D flow MRI at peak systolic time. This may occur due to oversampling of k-space center in 4D RTE spiral inducing an overestimation of flow in the flow measurement relative to the reference method (Doppler US).

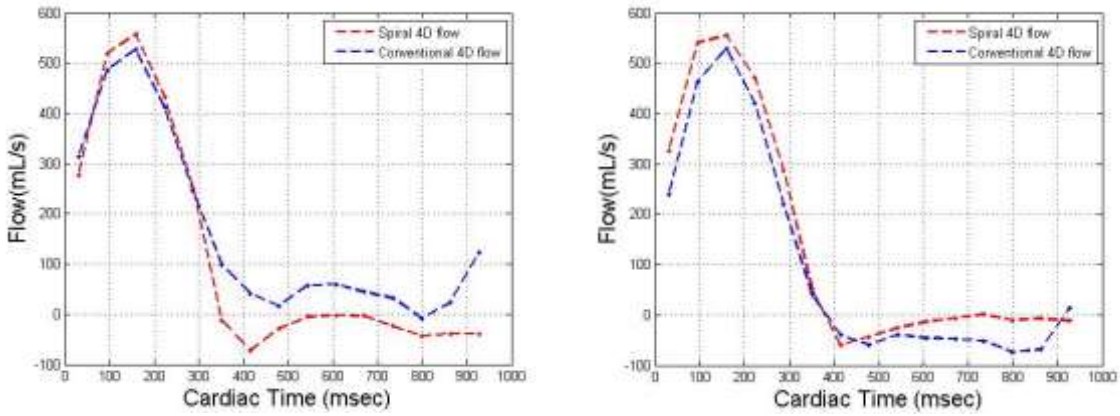

Figure 92 Flow waveform versus time at the level of the aortic valve (a), and 15 mm distal to the aortic valve (b) in patient 1 with AR, using conventional 4D flow (blue plot) and 4D RTE spiral flow (red plot).

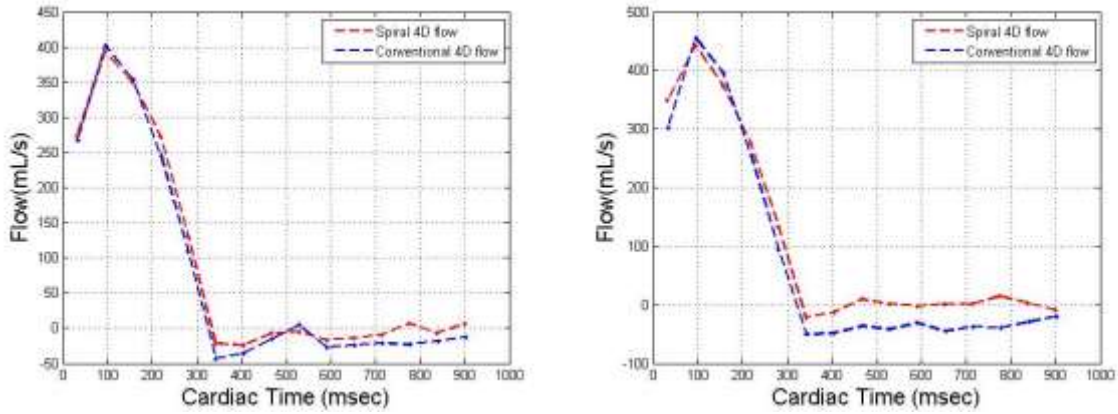

Figure 93 Flow waveform versus time at the level of the aortic valve (a), and 15 mm distal to the aortic valve (b) in patient 2 with AS, using conventional 4D flow (blue plot) and 4D RTE spiral flow (red plot).

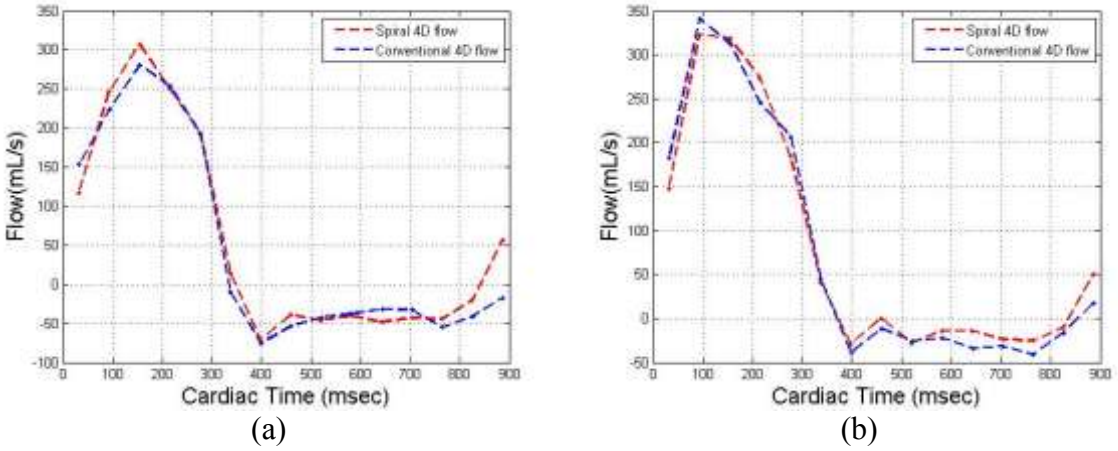

Figure 94 Flow waveform versus time at the level of the aortic valve (a), and 15 mm distal to the aortic valve (b) in patient 3 with AS, using conventional 4D flow (blue plot) and 4D RTE spiral flow (red plot).

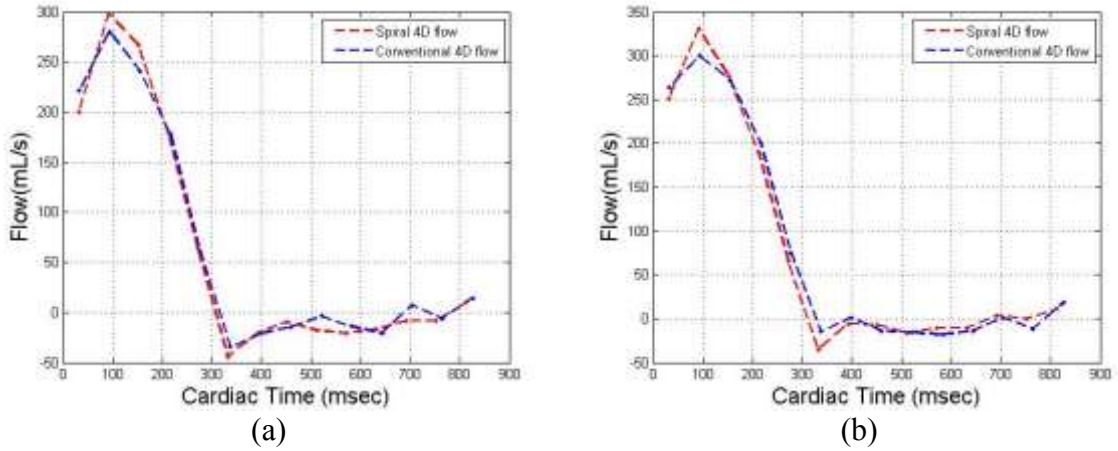

Figure 95 Flow waveform versus time at the level of the aortic valve (a), and 15 mm distal to the aortic valve (b) in patient 4 with AS, using conventional 4D flow (blue plot) and 4D RTE spiral flow (red plot).

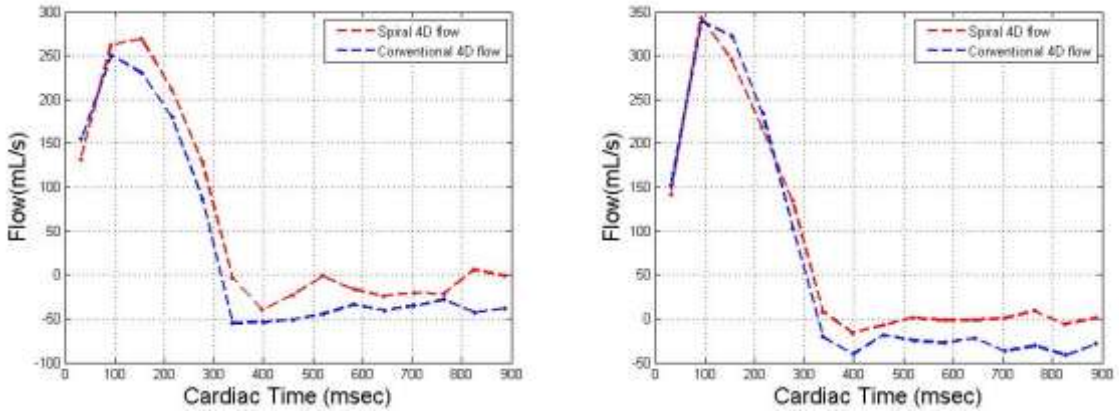

Figure 96 Flow waveform versus time at the level of the aortic valve (a), and 15 mm distal to the aortic valve (b) in patient 5 with AS, using conventional 4D flow (blue plot) and 4D RTE spiral flow (red plot).

In all subjects, both conventional 4D flow and 4D RTE spiral flow resulted in similar values for the AV eject time and LOV diameter. However in case of the LVOT diameter, MRI based methods resulted in considerably larger values relative to Doppler; this, is mainly due to circular LVOT assumption of Doppler which results in a smaller diameter in the anterior-posterior (AP) direction by Doppler. However, with MRI no assumption about the valve shape is required and one can use the actual shape of LVOT, resulting in a more accurate measurement.

Figure 97 reports the Bland-Altman plots, showing direct comparison between conventional 4D flow and Doppler US in LVOT measurement (bias = 0.73 cm, agreement limits = 0.02 to 1.44 cm), and between 4D RTE spiral flow and Doppler US in LVOT measurement (bias = 0.73 cm, agreement limits = -0.02 to 1.48 cm). Figure 97 indicates that both MRI methods have identical bias for LVOT diameter measurement (0.73cm) relative to Doppler. Figure 98 displays Bland-Altman plots showing pressure gradient differences versus mean measured pressure gradient between Doppler echo and

conventional 4D flow (left) and between Doppler echo and 4D RTE spiral flow (right). Based on bland Altman criteria, 4D RTE spiral flow has smaller bias (bias = 1.6 mmHg, agreement limits = -12.30 to 15.30 mmHg) than conventional 4D flow (bias = -5 mmHg, agreement limits = -16.43 to 6.43 mmHg) and should estimate peak pressure gradient and consequently severity of valve disease more precisely.

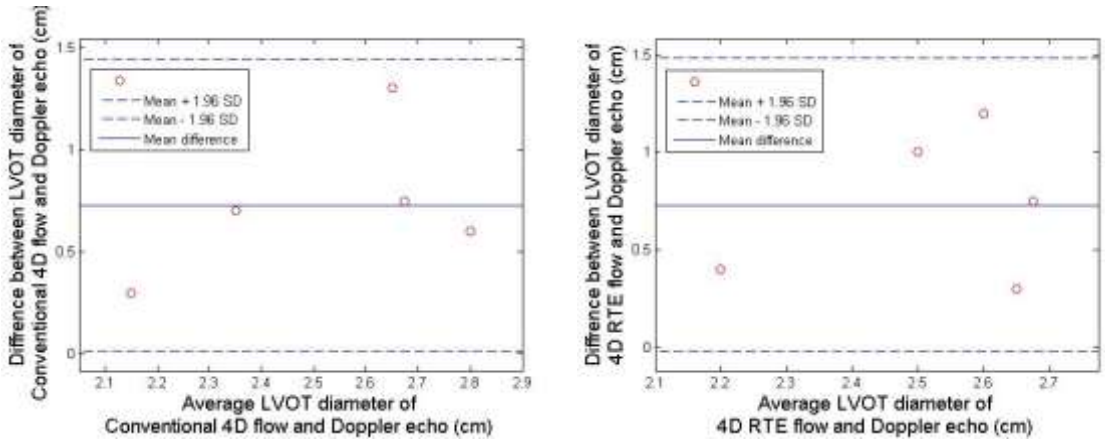

Figure 97 Bland–Altman plot at aortic valve in 5 patient demonstrating LVOT diameter differences versus mean LVOT diameter between (left) conventional 4D flow and Doppler echo, (right) between 4D RTE spiral flow and Doppler echo.

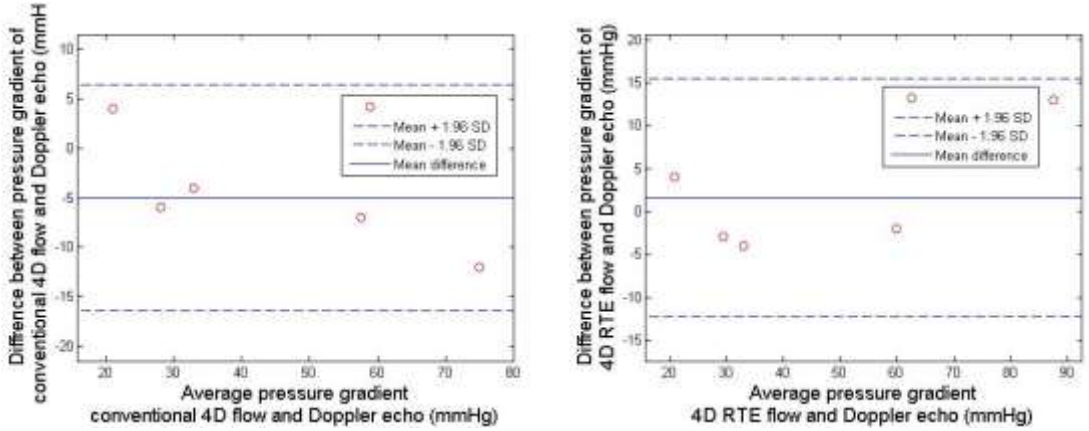

Figure 98 Bland–Altman plot at aortic valve in 5 patient demonstrating peak pressure gradient differences versus mean of peak pressure gradients between (left) conventional 4D flow and Doppler echo, (right) between 4D RTE spiral flow and Doppler echo.

Figures 99-104 display the 3D velocity profile and 2D velocity magnitude (top right corner of each image) of aortic valve in five patients using conventional 4D flow MRI (top row) and 4D RTE spiral flow MRI (bottom row) in peak systolic time. Both techniques have acceptable performance in visualization of valve shape. Statistical assessments of all patients may be found in Table 10. Yellow arrows point to similarities in the results. For patient 1, diagnosed with Aortic regurgitation (AR), two visualizations are demonstrated. Figure 99 shows systolic time in which valve operates well and no stenosis is observed. Figure 100 shows end-diastolic time in which inefficiency of aortic valve is observed leading to regurgitant flow. Both MRI methods are able to display the retrograde flow in patient 1.

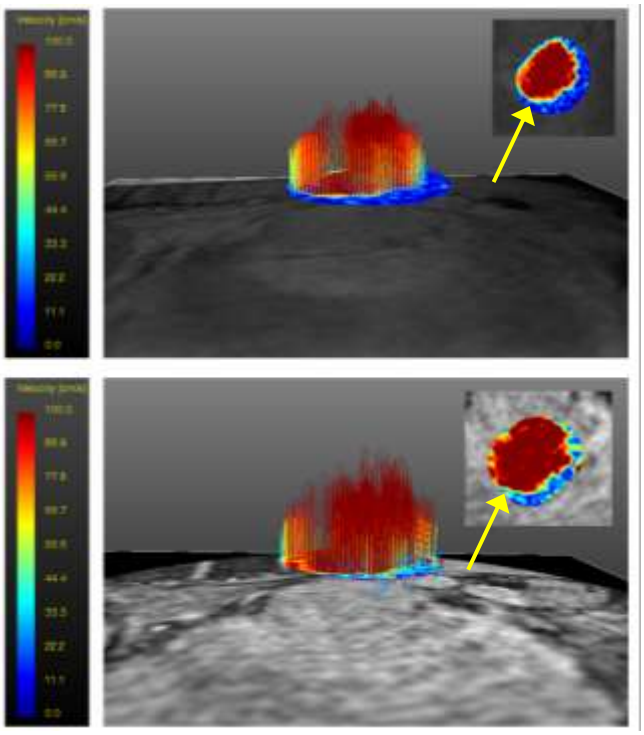

Figure 99. Velocity profiles in both 3D and 2D views (inset) in patient 1 with AR using Conventional 4D flow (top) and 4D RTE spiral flow (bottom) at peak systolic time.

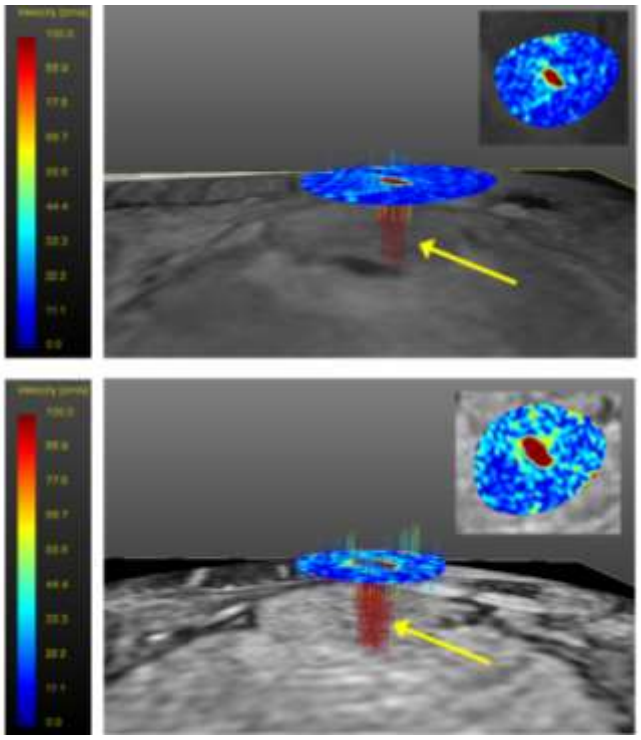

Figure 100. Velocity profiles in both 3D and 2D views (inset) in patient 1 with AR using Conventional 4D flow (top) and 4D RTE spiral flow (bottom) at peak diastolic time.

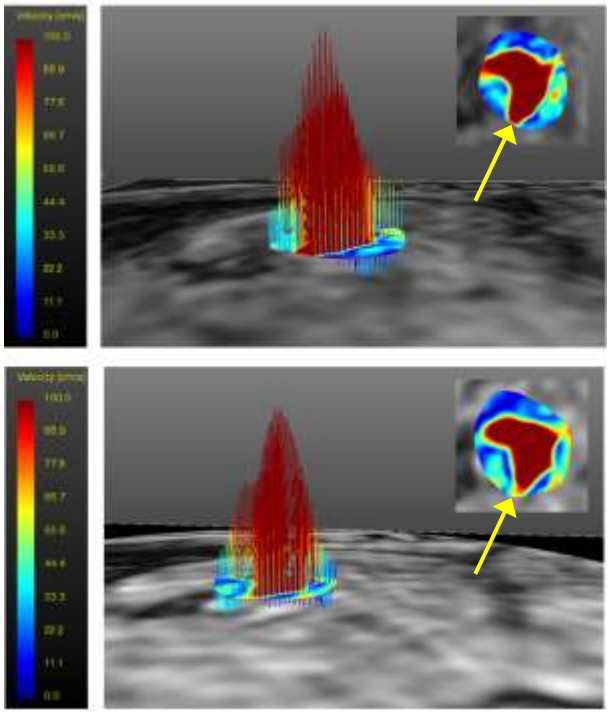

Figure 101. Velocity profiles in both 3D and 2D views (inset) in patient 2 with AS using Conventional 4D flow (top) and 4D RTE spiral flow (bottom) at peak systolic time.

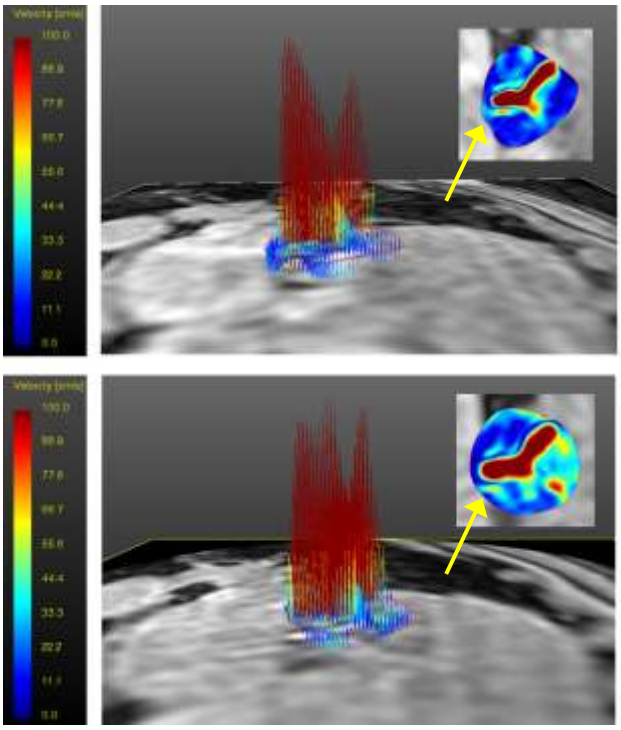

Figure 102. Velocity profiles in both 3D and 2D views (inset) in patient 3 with AS using Conventional 4D flow (top) and 4D RTE spiral flow (bottom) at peak systolic time.

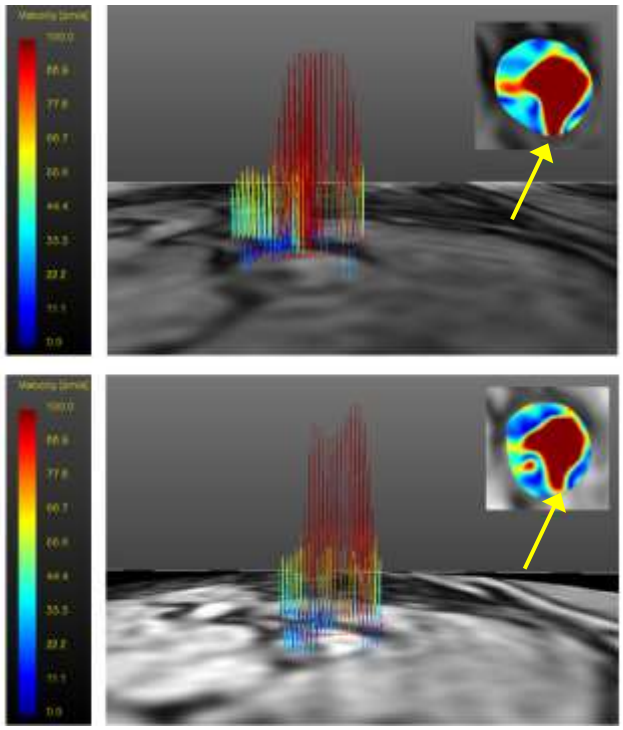

Figure 103. Velocity profiles in both 3D and 2D views (inset) in patient 4 with AS using Conventional 4D flow (top) and 4D RTE spiral flow (bottom) at peak systolic time.

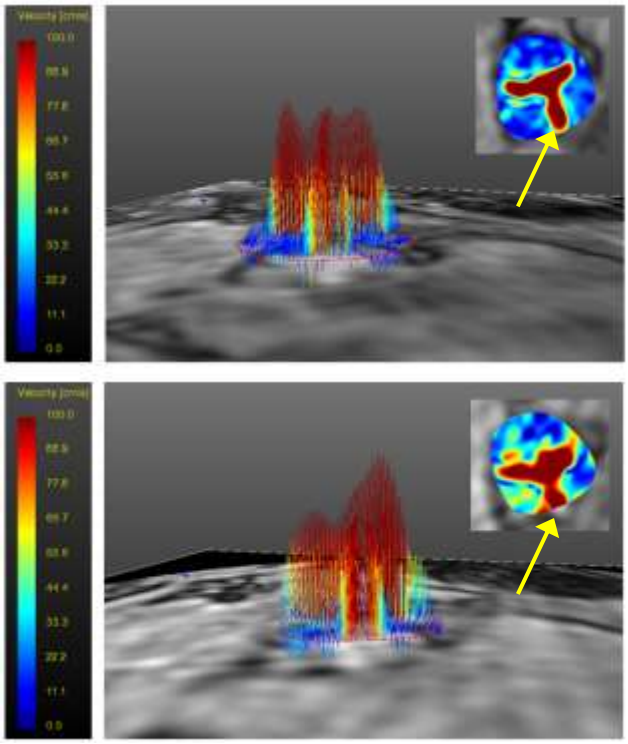

Figure 104. Velocity profiles in both 3D and 2D views (inset) in patient 5 with AS using Conventional 4D flow (top) and 4D RTE spiral flow (bottom) at peak systolic time.

7. Conclusions

This chapter investigated the feasibility of using a reduced TE stack of spirals k-space acquisition for 4D flow imaging in healthy volunteers and patients with Aortic Stenosis. The feasibility of performing efficient and accurate 4D velocity and flow measurement with the proposed pulse sequence under a variety of flow conditions was investigated. Results indicate substantial reductions in scan time when compared to conventional 4D flow. In phantom studies of stenotic flows, results based on the root mean squared error criterion indicate that 4D RTE Spiral flow is capable of providing the same level of accuracy as conventional 4D flow but with 30% reduction in scan times. Moreover, the proposed method has the added advantage of achieving a shorter echo time. In the second

part of results, application of the proposed sequence to 5 healthy volunteers and 5 subjects with mild to moderate Aortic Stenosis disease was reported. Results indicate that 4D RTE Spiral is capable of providing the same level of accuracy in flow measurement as in Conventional 4D flow MRI for imaging of the aortic valve, but on average with a 30% reduction in scan time and 45% reduction in echo time. Results indicate that 4D RTE Spiral flow MRI is an excellent technique for flow measurement in cardiac patients who are unable to tolerate longer scan times.

CHAPTER 5

CONCLUSIONS AND FUTURE RESEARCH DIRECTIONS

5.1. Introduction

This dissertation investigated the feasibility of using a reduced TE (RTE) stack of spirals k-space acquisition for 4D flow imaging and demonstrated an application in patients with Aortic Stenosis. The feasibility of performing efficient and accurate 4D velocity and flow measurement with the proposed pulse sequence under a variety of flow conditions was investigated. Results indicate substantial reductions in scan time when compared to conventional 4D flow. In phantom studies of stenotic flows, results based on the root mean squared error criterion indicate that 4D RTE Spiral flow is capable of providing the same level of accuracy as conventional 4D flow but with a 30% reduction in scan time. Moreover, the proposed method has the added advantage of achieving a shorter echo time - on the order of 2 ms versus 3.6 ms - for conventional 4D flow at Q=50ml/s and 1.57 ms versus 3.2 ms at Q=150 ml/s. Statistical results indicate that in low flow rates, there is a similar performance by both MRI methods; however, at the higher flow rates, 4D RTE spiral flow achieves slightly better accuracy with a 30% reduction in scan time. Also at low flow rates, qualitative results in phantom studies revealed that both methods have similar performance for flow profile visualization; however, at higher flow rates, 4D RTE spiral flow showed better performance in visualization of jet flows distal to occlusion relative to conventional 4D flow.

In the second part of results, application of the proposed sequence to 5 healthy volunteers and 5 subjects with mild to moderate Aortic Stenosis disease was investigated. Results indicate that 4D RTE Spiral is capable of providing the same level of accuracy in flow measurement as in Conventional 4D flow MRI for imaging of the aortic valve, but on average with a 30% reduction in scan time and 45% reduction in echo time. 4D RTE

Spiral was also able to achieve an echo time of 1.68 ms versus 2.9 ms for conventional 4D flow MRI, permitting less signal dephasing in the presence of jet flows distal to occlusions.

When compared to Doppler Ultrasound, 4D RTE Spiral flow measured peak velocity and maximum pressure gradient with a higher degree of accuracy relative to conventional 4D flow MRI; however, in LVOT diameter measurement, 4D RTE spiral flow and conventional 4D flow showed the same level of improvement when compared to Doppler Ultrasound. Results indicate that 4D RTE Spiral flow MRI is an excellent technique for flow measurement in cardiac patients who are unable to tolerate longer scan times.

5.2. Challenges

5.2.1. Imaging time

A long scan time is still a major limitation of 4D flow MRI in clinical studies and is more problematic when performing imaging while using navigator gating. Navigator gating prolongs the scan time at times by up to 10 minutes in total, depending on patient breathing and scan parameters. A 10 minute scan is still longer than typical cardiac scan times. To reduce scan time in 4D RTE Spiral flow, one may decrease the number of spiral interleaves (under sampling of the k-space) at the cost of reduction in flow measurement and visualization accuracy. As was demonstrated in the phantom studies, for the considered flow rates, 12 spiral interleaves in k-space results in a significant reduction in the scan time (up to 65% of conventional 4D flow). Such a k-space sampling strategy leads to appearance of streaking artifacts in the magnitude image. Interestingly

however, and despite the artifacts in the magnitude image, the errors in flow measurements as determined by RRMSE were acceptable.

Parallel imaging

To accelerate MRI data acquisition it is possible to acquire fewer phase-encoding lines than the Nyquist limit in *k*-space. In parallel imaging, data are acquired using an array of independent receiver channels. Each receiver coil element is more sensitive to the specific volume of tissue nearest to the coil element, meaning each coil encodes additional spatial information into its received signal. For each coil element, under-sampling the k-space data in the frequency domain results in an aliased image in the spatial domain. To reconstruct an unaliased image some prior knowledge of the individual coil sensitivities are required.

Two major parallel imaging techniques exist. The first approach uses aliased image and coil sensitivities in the spatial domain to reconstruct an unaliased image - this is the so-called Sensitivity Encoding (SENSE) approach [87]. The second approach uses the coil sensitivities to reconstruct the undersampled k-space lines - this is the so-called GRAPPA (Generalized Auto-calibrating Partially Parallel Acquisition) technique [88].

Although SENSE and GRAPPA use different techniques to reconstruct the missing data, at low accelerations, they provide very good results with acceptable quality in clinical applications. SENSE is the most widespread used parallel imaging technique and offered by many companies (Philips (SENSE), Siemens (mSENSE), General Electric (ASSET), and Toshiba (SPEEDER)). However, GRAPPA is more beneficial in areas where it is difficult to obtain accurate coil sensitivity maps; for instance, in inhomogeneous regions with low spin density such as the lung and the abdomen, the image quality of SENSE

reconstructions might suffer from inaccurate sensitivity maps. In contrast, the GRAPPA algorithm provides good quality image reconstructions, since the sensitivity information is extracted from the k-space.

To further reduce scan time, it should be possible to apply 4D RTE spiral flow in conjunction with parallel imaging techniques. Previously, authors have reported use of parallel imaging with spiral acquisitions – the same approach may be applied to 4D RTE Spiral flow imaging [89].

k-t BLAST

Since Cine images of heart exhibit a significant correlation in k-space and time, it should be possible to acquire only a smaller portion of k-space and recover missing data by using a small set of training data. This leads to shorter scan times or higher temporal resolution. k-t BLAST [90], uses the existing correlation in k-space and time to reduce acquisition times, achieving up to 4-fold accelerations.

5.2.2. Artifact

4D RTE spiral flow and all center-out trajectory based methods in general are more sensitive to magnetic field and RF inhomogeneity. It is suggested to position region of interest in iso-center of magnet and RF coil to mitigate this artifact.

5.2.3. Temporal resolution

A second area for further investigation may be to employ retrospective gating, as prospective gating usually leads to missing information during end-diastole and therefore leads to flow measurement errors in diastole. Retrospective gating can collect flow images throughout the cardiac cycle while improving the temporal resolution.

5.3. Other potential areas of application

Application of 4D RTE spiral phase contrast to other region of interest remains to be investigated. A prime candidate is neurovascular and peripheral arterial flows – we intend to investigate application of 4D RTE Spiral flow to imaging of patients with vascular occlusive disease in order to determine the feasibility of this method in assessment and visualization of flow through vascular stenoses. It is expected that the approach will result in highly efficient scan times, though in comparison to the aorta, the challenge will be the small size of arteries, especially at the site of stenosis which may be very tight. When compared to imaging of the aorta, it is expected that there will be a need for significant improvements in spatial resolutions. On the positive side, when imaging neurovascular and peripheral arteries away from the thorax, 4D RTE spiral flow should result in significantly faster scan times since there will be no need for respiratory motion compensation.

REFERENCES

[1] A. G. Webb, *Introduction to Biomedical Imaging*, first ed.: IEEE Press Series on Biomedical Engineering, 2003.

[2] Z. P. Liang and P. C. Lauterbur, *Principles of magnetic resonance imaging : a signal processing perspective*. New York: IEEE Press, 2000.

[3] P. Suetens, *Fundamentals of Medical Imaging*: Cambridge University Press, 2002.

[4] G. Z. Yang, P. J. Kilner, N. B. Wood, S. R. Underwood, and D. N. Firmin, "Computation of flow pressure fields from magnetic resonance velocity mapping," *Magn Reson Med,* vol. 36, pp. 520-6, Oct 1996.

[5] D. Xu, K. L. Ryan, C. A. Rickards, G. Zhang, V. A. Convertino, and R. Mukkamala, "Improved pulse transit time estimation by system identification analysis of proximal and distal arterial waveforms," vol. 301, pp. H1389-H1395, 2011-10-01 00:00:00 2011.

[6] M. Markl, P. J. Kilner, and T. Ebbers, "Comprehensive 4D velocity mapping of the heart and great vessels by cardiovascular magnetic resonance," *J Cardiovasc Magn Reson,* vol. 13, p. 7, 2011.

[7] J. Stout. (2008). *Using MotionTrak for motion correction in body imaging*. Available: http://incenter.medical.philips.com/doclib/enc/fetch/2000/4504/3634249/3634100/4987812/5025553/5068598/5392198/FS35-12_Aptip_MotionTrak.pdf%3fnodeid%3d5392417%26vernum%3d1

[8] J. R. Cebral, M. A. Castro, S. Appanaboyina, C. M. Putman, D. Millan, and A. F. Frangi, "Efficient pipeline for image-based patient-specific analysis of cerebral aneurysm hemodynamics: technique and sensitivity," *IEEE Trans Med Imaging,* vol. 24, pp. 457-67, Apr 2005.

[9] Jerry Allison, Chris Wright, and T. Lavin. (2009). *MRI Physics Course*. Available: http://www.radiology.georgiahealth.edu/RadiologyPhysics/mri/MR%20cha11%20MRA.ppt

[10] G. Farzan, D. Xiaoyan, C. Alain De, D. Yvan, K. Martin, and G. Robert, "Low Reynolds number turbulence modeling of blood flow in arterial stenoses," *Biorheology,* vol. 35, pp. 281-294, 1998.

[11] J. L. A. Carvalho and K. S. Nayak, "Rapid quantitation of cardiovascular flow using slice-selective fourier velocity encoding with spiral readouts," *Magnetic Resonance in Medicine,* vol. 57, pp. 639-646, 2007.

[12] G. T. Luk Pat, J. M. Pauly, B. S. Hu, and D. G. Nishimura, "One-shot spatially resolved velocity imaging," *Magn Reson Med,* vol. 40, pp. 603-13, Oct 1998.

[13] K. S. Nayak, B. S. Hu, and D. G. Nishimura, "Rapid quantitation of high-speed flow jets," *Magnetic Resonance in Medicine,* vol. 50, pp. 366-372, 2003.

[14] A. J. Winkler and J. Wu, "Correction of intrinsic spectral broadening errors in doppler peak velocity measurements made with phased sector and linear array transducers," *Ultrasound in Medicine & Biology,* vol. 21, pp. 1029-1035, 1995.

[15] P. R. Hoskins, "Accuracy of maximum velocity estimates made using Doppler ultrasound systems," *Br J Radiol,* vol. 69, pp. 172-177, February 1, 1996 1996.

[16] M. O'Donnell, "NMR blood flow imaging using multiecho, phase contrast sequences," *Med Phys,* vol. 12, pp. 59-64, Jan-Feb 1985.

[17] G. D. Clarke, W. G. Hundley, R. W. McColl, R. Eckels, D. S. C. Chaney, H.-F. Li*, et al.*, "Velocity-encoded, phase-difference cine MRI measurements of coronary artery flow: Dependence of flow accuracy on the number of cine frames," *Journal of Magnetic Resonance Imaging,* vol. 6, pp. 733-742, 1996.

[18] C. Tang, D. D. Blatter, and D. L. Parker, "Accuracy of phase-contrast flow measurements in the presence of partial-volume effects," *Journal of Magnetic Resonance Imaging,* vol. 3, pp. 377-385, 1993.

[19] R. H. Mohiaddin, P. D. Gatehouse, M. Henien, and D. N. Firmin, "Cine MR fourier velocimetry of blood flow through cardiac valves: Comparison with doppler echocardiography," *Journal of Magnetic Resonance Imaging,* vol. 7, pp. 657-663, 1997.

[20] D. G. Nishimura, *Principles of Magnetic Resonance Imaging*: Stanford Univ 2010.

[21] T. M. Grist, C. A. Mistretta, C. M. Strother, and P. A. Turski, "Time-resolved angiography: Past, present, and future," *J Magn Reson Imaging,* vol. 36, pp. 1273-86, Dec 2012.

[22] P. R. Moran, "A flow velocity zeugmatographic interlace for NMR imaging in humans," *Magnetic Resonance Imaging,* vol. 1, pp. 197-203, 1982.

[23] T. Leiner, "Magnetic resonance angiography of abdominal and lower extremity vasculature," *Top Magn Reson Imaging,* vol. 16, pp. 21-66, Feb 2005.

[24] J. Meaney, "Magnetic resonance angiography of the peripheral arteries: current status," *European Radiology,* vol. 13, pp. 836-852, 2003.

[25] K. S. Nayak, P. A. Rivas, J. M. Pauly, G. C. Scott, A. B. Kerr, B. S. Hu*, et al.*, "Real-time black-blood MRI using spatial presaturation," *Journal of Magnetic Resonance Imaging,* vol. 13, pp. 807-812, 2001.

[26] N. J. Pelc, F. G. Sommer, K. C. Li, T. J. Brosnan, R. J. Herfkens, and D. R. Enzmann, "Quantitative magnetic resonance flow imaging," *Magn Reson Q,* vol. 10, pp. 125-47, Sep 1994.

[27] O. P. Simonetti, R. E. Wendt, 3rd, and J. L. Duerk, "Significance of the point of expansion in interpretation of gradient moments and motion sensitivity," *J Magn Reson Imaging,* vol. 1, pp. 569-77, Sep-Oct 1991.

[28] E. L. Hahn, "Detection of Sea-Water Motion by Nuclear Precession," *Journal of Geophysical Research,* vol. 65, pp. 776-777, 1960.

[29] P Van Dijk, "Direct Cardiac NMR Imaging of Heart Wall and Blood Flow Velocity," *Journal of Computer Assisted Tomography,* vol. 8, pp. 429-436, 1984.

[30] P. Gatehouse, J. Keegan, L. Crowe, S. Masood, R. Mohiaddin, K.-F. Kreitner*, et al.*, "Applications of phase-contrast flow and velocity imaging in cardiovascular MRI," *European Radiology,* vol. 15, pp. 2172-2184, 2005.

[31] Q. S. Xiang, "Temporal phase unwrapping for CINE velocity imaging," *J Magn Reson Imaging,* vol. 5, pp. 529-34, Sep-Oct 1995.

[32] M. J. Negahdar, J. Cha, M. Shakeri, M. Kendrick, M. Alshaher, I. Khodarahimi*, et al.*, "Effect of Venc on accuracy of velocity profiles in multi-slice phase-contrast MR imaging of stenotic flow," in *Biomedical Imaging (ISBI), 2012 9th IEEE International Symposium on*, 2012, pp. 820-823.

[33] A. H. Andersen and J. E. Kirsch, "Analysis of noise in phase contrast MR imaging," *Med Phys,* vol. 23, pp. 857-69, Jun 1996.

[34] A. V. Barger, D. C. Peters, W. F. Block, K. K. Vigen, F. R. Korosec, T. M. Grist*, et al.*, "Phase-contrast with interleaved undersampled projections," *Magnetic Resonance in Medicine,* vol. 43, pp. 503-509, 2000.

[35] M. Kadbi, H. Wang, M. J. Negahdar, L. Warner, M. Traughber, P. Martin*, et al.*, "A novel phase-corrected 3D cine ultra-short te (UTE) phase-contrast MRI technique," in *Engineering in Medicine and Biology Society (EMBC), 2012 Annual International Conference of the IEEE*, 2012, pp. 77-81.

[36] M. Kadbi, M. Negahdar, J. W. Cha, M. Traughber, P. Martin, M. F. Stoddard*, et al.*, "4D UTE flow: A phase-contrast MRI technique for assessment and visualization of stenotic flows," *Magn Reson Med,* Mar 6 2014.

[37] D. G. Nishimura, P. Irarrazabal, and C. H. Meyer, "A velocity k-space analysis of flow effects in echo-planar and spiral imaging," *Magn Reson Med,* vol. 33, pp. 549-56, Apr 1995.

[38] K. F. King, T. K. Foo, and C. R. Crawford, "Optimized gradient waveforms for spiral scanning," *Magn Reson Med,* vol. 34, pp. 156-60, Aug 1995.

[39] G. B. Pike, C. H. Meyer, T. J. Brosnan, and N. J. Pelc, "Magnetic resonance velocity imaging using a fast spiral phase contrast sequence," *Magnetic Resonance in Medicine,* vol. 32, pp. 476-483, 1994.

[40] J. L. A. Carvalho, J.-F. Nielsen, and K. S. Nayak, "Feasibility of in vivo measurement of carotid wall shear rate using spiral fourier velocity encoded MRI," *Magnetic Resonance in Medicine,* vol. 63, pp. 1537-1547, 2010.

[41] A. V. Barger, W. F. Block, Y. Toropov, T. M. Grist, and C. A. Mistretta, "Time-resolved contrast-enhanced imaging with isotropic resolution and broad coverage using an undersampled 3D projection trajectory," *Magnetic Resonance in Medicine,* vol. 48, pp. 297-305, 2002.

[42] Point spread function [Online]. Available: http://en.wikipedia.org/wiki/Point_spread_function

[43] M. Á. González Ballester, A. P. Zisserman, and M. Brady, "Estimation of the partial volume effect in MRI," *Medical Image Analysis,* vol. 6, pp. 389-405, 2002.

[44] M. J. P. van Osch, E.-j. P. A. Vonken, C. J. G. Bakker, and M. A. Viergever, "Correcting partial volume artifacts of the arterial input function in quantitative cerebral perfusion MRI," *Magnetic Resonance in Medicine,* vol. 45, pp. 477-485, 2001.

[45] P. G. Walker, G. B. Cranney, M. B. Scheidegger, G. Waseleski, G. M. Pohost, and A. P. Yoganathan, "Semiautomated method for noise reduction and background phase error correction in MR phase velocity data," *J Magn Reson Imaging,* vol. 3, pp. 521-30, May-Jun 1993.

[46] T. Miller, A. Landes, and A. Moran, "Improved accuracy in flow mapping of congenital heart disease using stationary phantom technique," *Journal of Cardiovascular Magnetic Resonance,* vol. 11, p. 52, 2009.

[47] D. L. K. M. Johnson, O. Wieben, "Eddy Current Corrections for Phase Contrast MRI Using Gradient Calibration," *ISMRM,* vol. 17, 2009.

[48] M. A. Bernstein, X. J. Zhou, J. A. Polzin, K. F. King, A. Ganin, N. J. Pelc*, et al.*, "Concomitant gradient terms in phase contrast MR: Analysis and correction," *Magnetic Resonance in Medicine,* vol. 39, pp. 300-308, 2006.

[49] P. Thunberg, L. Wigström, B. Wranne, J. Engvall, and M. Karlsson, "Correction for acceleration-induced displacement artifacts in phase contrast imaging," *Magnetic Resonance in Medicine,* vol. 43, pp. 734-738, 2000.

[50] M. J. Negahdar, M. Kadbi, M. Kotys, M. Alshaher, S. Fischer, and A. A. Amini, "Rapid flow quantification in iliac arteries with spiral phase-contrast MRI," in *Engineering in Medicine and Biology Society,EMBC, 2011 Annual International Conference of the IEEE*, 2011, pp. 2804-2808.

[51] L. Wigström, L. Sjöqvist, and B. Wranne, "Temporally resolved 3D phase-contrast imaging," *Magnetic Resonance in Medicine,* vol. 36, pp. 800-803, 1996.

[52] M. Markl, A. Harloff, T. A. Bley, M. Zaitsev, B. Jung, E. Weigang*, et al.*, "Time-resolved 3D MR velocity mapping at 3T: Improved navigator-gated assessment of vascular anatomy and blood flow," *Journal of Magnetic Resonance Imaging,* vol. 25, pp. 824-831, 2007.

[53] M. Markl, A. Frydrychowicz, S. Kozerke, M. Hope, and O. Wieben, "4D flow MRI," *J Magn Reson Imaging,* vol. 36, pp. 1015-36, Nov 2012.

[54] S. Uribe, P. Beerbaum, T. S. Sørensen, A. Rasmusson, R. Razavi, and T. Schaeffter, "Four-dimensional (4D) flow of the whole heart and great vessels using real-time respiratory self-gating," *Magnetic Resonance in Medicine,* vol. 62, pp. 984-992, 2009.

[55] M. Kadbi, M. Negahdar, M. Traughber, P. Martin, and A. A. Amini, "Assessment of flow and hemodynamics in the carotid artery using a reduced TE 4D flow spiral phase-contrast MRI," in *Engineering in Medicine and Biology Society (EMBC), 2013 35th Annual International Conference of the IEEE*, 2013, pp. 1100-1103.

[56] A. Frydrychowicz, J. T. Winterer, M. Zaitsev, B. Jung, J. Hennig, M. Langer*, et al.*, "Visualization of iliac and proximal femoral artery hemodynamics using time-resolved 3D phase contrast MRI at 3T," *Journal of Magnetic Resonance Imaging,* vol. 25, pp. 1085-1092, 2007.

[57] S. Wetzel, S. Meckel, A. Frydrychowicz, L. Bonati, E. W. Radue, K. Scheffler*, et al.*, "In vivo assessment and visualization of intracranial arterial hemodynamics with flow-sensitized 4D MR imaging at 3T," *AJNR Am J Neuroradiol,* vol. 28, pp. 433-8, Mar 2007.

[58] A. Harloff, F. Albrecht, J. Spreer, A. F. Stalder, J. Bock, A. Frydrychowicz*, et al.*, "3D blood flow characteristics in the carotid artery bifurcation assessed by flow-sensitive 4D MRI at 3T," *Magnetic Resonance in Medicine,* vol. 61, pp. 65-74, 2009.

[59] M. D. Hope, T. A. Hope, A. K. Meadows, K. G. Ordovas, T. H. Urbania, M. T. Alley*, et al.*, "Bicuspid aortic valve: four-dimensional MR evaluation of ascending aortic systolic flow patterns," *Radiology,* vol. 255, pp. 53-61, Apr 2010.

[60] Z. Stankovic, A. Frydrychowicz, Z. Csatari, E. Panther, P. Deibert, W. Euringer*, et al.*, "MR-based visualization and quantification of three-dimensional flow characteristics in the portal venous system," *Journal of Magnetic Resonance Imaging,* vol. 32, pp. 466-475, 2010.

[61] N. J. Pelc, M. A. Bernstein, A. Shimakawa, and G. H. Glover, "Encoding strategies for three-direction phase-contrast MR imaging of flow," *Journal of Magnetic Resonance Imaging,* vol. 1, pp. 405-413, 1991.

[62] B. Jung and M. Markl, "Phase-Contrast MRI and Flow Quantification," in *Magnetic Resonance Angiography*, J. C. Carr and T. J. Carroll, Eds., ed: Springer New York, 2012, pp. 51-64.

[63] K. M. Johnson and M. Markl, "Improved SNR in phase contrast velocimetry with five-point balanced flow encoding," *Magnetic Resonance in Medicine,* vol. 63, pp. 349-355, 2010.

[64] M. D. Hope, A. K. Meadows, T. A. Hope, K. G. Ordovas, G. P. Reddy, M. T. Alley*, et al.*, "Images in cardiovascular medicine. Evaluation of bicuspid aortic valve and aortic coarctation with 4D flow magnetic resonance imaging," *Circulation,* vol. 117, pp. 2818-9, May 27 2008.

[65] A. Harloff, C. Strecker, A. P. Frydrychowicz, P. Dudler, A. Hetzel, A. Geibel*, et al.*, "Plaques in the descending aorta: a new risk factor for stroke? Visualization of potential embolization pathways by 4D MRI," *J Magn Reson Imaging,* vol. 26, pp. 1651-5, Dec 2007.

[66] M. Carlsson, J. Toger, M. Kanski, K. M. Bloch, F. Stahlberg, E. Heiberg*, et al.*, "Quantification and visualization of cardiovascular 4D velocity mapping accelerated with parallel imaging or k-t BLAST: head to head comparison and validation at 1.5 T and 3 T," *J Cardiovasc Magn Reson,* vol. 13, p. 55, 2011.

[67] S. Uribe, P. Beerbaum, T. S. Sorensen, A. Rasmusson, R. Razavi, and T. Schaeffter, "Four-dimensional (4D) flow of the whole heart and great vessels using real-time respiratory self-gating," *Magn Reson Med,* vol. 62, pp. 984-92, Oct 2009.

[68] S. Uribe, V. Muthurangu, R. Boubertakh, T. Schaeffter, R. Razavi, D. L. G. Hill*, et al.*, "Whole-heart cine MRI using real-time respiratory self-gating," *Magnetic Resonance in Medicine,* vol. 57, pp. 606-613, 2007.

[69] M. D. Hope, A. K. Meadows, T. A. Hope, K. G. Ordovas, D. Saloner, G. P. Reddy*, et al.*, "Clinical evaluation of aortic coarctation with 4D flow MR imaging," *J Magn Reson Imaging,* vol. 31, pp. 711-8, Mar 2010.

[70] T. Gu, F. R. Korosec, W. F. Block, S. B. Fain, Q. Turk, D. Lum*, et al.*, "PC VIPR: A High-Speed 3D Phase-Contrast Method for Flow Quantification and High-Resolution Angiography," *American Journal of Neuroradiology,* vol. 26, pp. 743-749, April 1, 2005 2005.

[71] S. Kecskemeti, K. Johnson, Y. Wu, C. Mistretta, P. Turski, and O. Wieben, "High resolution three-dimensional cine phase contrast MRI of small intracranial aneurysms using a stack of stars k-space trajectory," *J Magn Reson Imaging,* vol. 35, pp. 518-27, Mar 2012.

[72] C. A. Hamilton, P. R. Moran, P. Santago, 2nd, and S. A. Rajala, "Effects of intravoxel velocity distributions on the accuracy of the phase-mapping method in phase-contrast MR angiography," *J Magn Reson Imaging,* vol. 4, pp. 752-5, Sep-Oct 1994.

[73] L. Sondergaard, P. Hildebrandt, K. Lindvig, C. Thomsen, F. Stahlberg, E. Kassis*, et al.*, "Valve area and cardiac output in aortic stenosis: quantification by magnetic resonance velocity mapping," *Am Heart J,* vol. 126, pp. 1156-64, Nov 1993.

[74] L. Sondergaard, F. Stahlberg, C. Thomsen, A. Stensgaard, K. Lindvig, and O. Henriksen, "Accuracy and precision of MR velocity mapping in measurement of stenotic cross-sectional area, flow rate, and pressure gradient," *J Magn Reson Imaging,* vol. 3, pp. 433-7, Mar-Apr 1993.

[75] K. R. O'Brien, B. R. Cowan, M. Jain, R. A. Stewart, A. J. Kerr, and A. A. Young, "MRI phase contrast velocity and flow errors in turbulent stenotic jets," *J Magn Reson Imaging,* vol. 28, pp. 210-8, Jul 2008.

[76] M. Negahdar, M. Kadbi, M. Kendrick, R. Longaker, M. Stoddard, and A. Amini, "Assessment and quantification of aortic stenosis hemodynamics with 4d flow: comparison with doppler echocardiography," in *ISMRM*, Milan, Italy, 2014.

[77] A. Sigfridsson, S. Petersson, C. J. Carlhall, and T. Ebbers, "Four-dimensional flow MRI using spiral acquisition," *Magn Reson Med,* vol. 68, pp. 1065-73, Oct 2012.

[78] R. L. Janiczek, C. H. Meyer, S. T. Acton, B. R. Blackman, and F. H. Epstein, "4D Spiral Phase-Contrast MRI of Wall Shear Stress in the Mouse Aorta," *International Society for Magnetic Resonance in Medicine(ISMRM),* 2009.

[79] A. Takahashi, T. Q. Li, St, oslash, J. dkilde, oslash*, et al.*, "A Pulse Sequence for Flow Evaluation Based on Self-Refocused RF and Interleaved Spiral Readout," *J Magn Reson,* vol. 126, pp. 127-32, May 1997.

[80] C. L. Dumoulin, S. P. Souza, R. D. Darrow, N. J. Pelc, W. J. Adams, and S. A. Ash, "Simultaneous acquisition of phase-contrast angiograms and stationary-tissue images with Hadamard encoding of flow-induced phase shifts," *Journal of Magnetic Resonance Imaging,* vol. 1, pp. 399-404, 1991.

[81] J. N. Oshinski, D. N. Ku, and R. I. Pettigrew, "Turbulent fluctuation velocity: the most significant determinant of signal loss in stenotic vessels," *Magn Reson Med,* vol. 33, pp. 193-9, Feb 1995.

[82] D. J. Pennell, U. P. Sechtem, C. B. Higgins, W. J. Manning, G. M. Pohost, F. E. Rademakers*, et al.*, "Clinical indications for cardiovascular magnetic resonance (CMR): Consensus Panel report," *European Heart Journal,* vol. 25, pp. 1940-1965, November 1, 2004 2004.

[83] P. J. Kilner, C. C. Manzara, R. H. Mohiaddin, D. J. Pennell, M. G. Sutton, D. N. Firmin*, et al.*, "Magnetic resonance jet velocity mapping in mitral and aortic valve stenosis," *Circulation,* vol. 87, pp. 1239-48, Apr 1993.

[84] L. Sondergaard, C. Thomsen, F. Stahlberg, E. Gymoese, K. Lindvig, P. Hildebrandt*, et al.*, "Mitral and aortic valvular flow: quantification with MR phase mapping," *J Magn Reson Imaging,* vol. 2, pp. 295-302, May-Jun 1992.

[85] S. D. Caruthers, S. J. Lin, P. Brown, M. P. Watkins, T. A. Williams, K. A. Lehr*, et al.*, "Practical value of cardiac magnetic resonance imaging for clinical quantification of aortic valve stenosis: comparison with echocardiography," *Circulation,* vol. 108, pp. 2236-43, Nov 4 2003.

[86] E. A. Waters, S. D. Caruthers, and S. A. Wickline, "Correlation analysis of stenotic aortic valve flow patterns using phase contrast MRI," *Ann Biomed Eng,* vol. 33, pp. 878-87, Jul 2005.

[87] K. P. Pruessmann, M. Weiger, M. B. Scheidegger, and P. Boesiger, "SENSE: sensitivity encoding for fast MRI," *Magn Reson Med,* vol. 42, pp. 952-62, Nov 1999.

[88] M. A. Griswold, P. M. Jakob, R. M. Heidemann, M. Nittka, V. Jellus, J. Wang*, et al.*, "Generalized autocalibrating partially parallel acquisitions (GRAPPA)," *Magn Reson Med,* vol. 47, pp. 1202-10, Jun 2002.

[89] R. M. Heidemann, M. A. Griswold, N. Seiberlich, G. Kruger, S. A. Kannengiesser, B. Kiefer*, et al.*, "Direct parallel image reconstructions for spiral trajectories using GRAPPA," *Magn Reson Med,* vol. 56, pp. 317-26, Aug 2006.

[90] J. Tsao, P. Boesiger, and K. P. Pruessmann, "k-t BLAST and k-t SENSE: dynamic MRI with high frame rate exploiting spatiotemporal correlations," *Magn Reson Med,* vol. 50, pp. 1031-42, Nov 2003.

CURRICULUM VITA

Name: Mohammadjavad Negahdar

Address: 425 Lutz Hall,
Department of Electrical and Computer Engineering
University of Louisville,
Louisville, Ky. 40292

Phone *:* 502-852-3400
E-mail*:* m0nega02@louisville.edu

EDUCATION

University of Louisville (UofL) Ph.D. Electrical and Computer Engineering. *Thesis: 4D Reduced-TE (RTE) Phase Contrast MRI for Rapid Quantification and Visualization of Blood Flow and Hemodynamics*.	Louisville, KY 2009 - 2014 GPA: 4.00 / 4.00
K.N. Toosi University of Technology (K.N.Toosi) M.S. Electrical and Computer Engineering. *Thesis: Cross-layer design for increasing a life-time of Wireless Sensor Networks.*	Tehran, Iran 2006 – 2008 GPA: 17.23 / 20
K.N. Toosi University of Technology (K.N.Toosi) B.S. Electrical and Computer Engineering. *Thesis: Develop and implementation a security algorithm in bluetooth systems.*	Tehran, Iran 2000 – 2005 GPA: 15.63 / 20
National Organization of Development of Exceptional Talents (NODET)	Tehran, Iran 1996 – 2000 GPA: 19.60 / 20

RESEARCH INTERESTS

- ✓ Medical Imaging
  - Cardiac and cardiovascular Imaging.
  - Fast imaging techniques.
  - MRI pulse programming.

- ✓ Medical Image Analysis.
  - Delayed reconstruction techniques.
  - Assessment of arterial hemodynamic based on MRI.

RESEARCH, TEACHING AND WORK EXPERIENCE

- ✓ Internship: Philips Healthcare in North America-MRI section, Cleveland, OH, Fall 2010.
  - Attending Sequence Development (SDM), Pulse Programming environment (PPE) and Data handling courses.
- ✓ Research Staff: Veteran's Affairs Medical Center, Louisville, KY, 2011-2014.
  - Developing new imaging and post processing for Rapid Quantification and Visualization of Blood Flow and Hemodynamics.
- ✓ Research Assistant: University of Louisville, Louisville, KY, 2011-2014.
  - Developing fast imaging methods using PC-MRI.
- ✓ Teaching Assistant:
  - Digital Signal Processing, University of Louisville, Louisville, KY, Fall 2013.
  - Principles of telecommunication systems, K.N. Toosi, Tehran, Iran, Fall and Spring 2007.
  - Microcontrollers, K.N. Toosi, Tehran, Iran, Spring 2004.
  - Logic circuit design, K.N. Toosi, Tehran, Iran, Fall 2003.
  - Instructor, Matlab programming language, K.N. Toosi, Tehran, Iran, Fall 2003.

SKILLS AND CERTIFICATES

- ✓ Sequence Development, Pulse Programming and Data handling, Philips Healthcare in North America, Cleveland, OH.
- ✓ Project Management at RWTUV, Tehran, Iran.
- ✓ HIPAA and CITI certified at University of Louisville Hospital, Louisville, KY.
- ✓ Extended CITI certified at Veterans Affairs Medical Center, Louisville, KY.
- ✓ Professional in Matlab and C++, Philips GOALC pulse programing language.

HONORS AND POSITIONS

- ✓ Outstanding Graduate Student Award, University of Louisville (2014).
- ✓ Grosscurth Fellowship award, University of Louisville (2009-2010).
- ✓ Third place (2011) and fifth place (2012) in engineering exposition, University of Louisville.
- ✓ Senator of Student Senate, University of Louisville (2013).
- ✓ Judge in Louisville Regional Science Fair (LRSF-2103).
- ✓ Second rank in Robo-deminer competition (2002).
- ✓ Seven years of study (Middle and High School) in the national Organization for Exceptional Talents (NODET).

JOURNAL AND CONFERENCE REVIEWER

Journals:

- ✓ IEEE Transaction on Medical Imaging
- ✓ Computerized Medical Imaging and Graphics.

Conferences:

- ✓ Medical Image Computing and Computer Assisted Intervention (MICCAI).
- ✓ International Symposium of Biomedical Imaging (ISBI).
- ✓ Engineering in Medicine and Biology Society (EMBS).

PROFESSIONAL ORGANIZATION MEMBERSHIP

- ✓ Member, International Society for Magnetic Resonance in Medicine (ISMRM).
- ✓ Member, Institute of Electrical and Electronics Engineering (IEEE).
- ✓ Member, IEEE Engineering in Medicine and Biology Society (EMBS).
- ✓ Member, SPIE Medical Imaging.

PUBLICATION

Book chapter:

- **MJ Negahdar**, M. Kadbi, A. Amini, "Flow Imaging with MRI", in Physics of cardiovascular and neurovascular imaging, Carlo Cavedon and Stephen Rudin, Taylor & Francis Books, Inc., New York, NY, (2014).

Peer reviewed Journals:

- M. Kadbi, **MJ Negahdar**, J. Cha, M. Traughber, P. Martin, M. Stoddard, and A. Amini, 4D UTE Flow: A Phase Contrast MRI Technique for Assessment of Stenotic Flows, Magnetic Resonance in Medicine-MRM (2014).

Peer reviewed Conferences:

- **MJ Negahdar**, M. Kadbi, M. Kendrick, R. Longaker, M. Stoddard, and A. Amin, Assessment and Quantification of Aortic Stenosis Hemodynamics with 4D Flow: Comparison with Doppler Echocardiography, 22th International Society of Magnetic Resonance in Medicine Annual Meeting (ISMRM). Milano, Italy (2014).
- **MJ Negahdar**, M. Kadbi, M. Kendrick, R. Longaker, S. Ikram, M. Stoddard, A. Amini, Non-invasive 3D pressure calculation from 4D flow: Pulsatile Phantom study, International Symposium on Biomedical Imaging (ISBI) Beijing, China (2014).
- **MJ Negahdar**, M. Kadbi, M. Kendrick, R. Longaker, S. Ikram, M. Stoddard, A. Amini, Assessment and Visualization of Pulsatile Flow in Aortic Stenosis with 4D Flow MRI, International Symposium on Biomedical Imaging (ISBI) Beijing, China (2014).
- **MJ Negahdar**, M. Kadbi, J. Cha, J. Cebral, and A. Amin, A Fast 3D Non-Iterative Approach to Pressure Calculation from PC-MRI: Phantom Experiments, 21th International Society of Magnetic Resonance in Medicine Annual Meeting (ISMRM). Salt Lake city, Utah, USA (2013).
- M. Kadbi, **MJ Negahdar**, M. Traughber, P. Martin, and A. Amini, A Fast Reduced TE 4D Spiral PC MRI Sequence for Assessment of Flow and Hemodynamics, 21th International Society of Magnetic Resonance in Medicine Annual Meeting (ISMRM). Salt Lake city, Utah, USA (2013).
- **MJ Negahdar**, M. Kadbi, V. Tavakoli, J. Heidenreich, and A. Amini, Comparison of Cartesian, UTE radial, and Spiral Phase-Contrast MRI in Measurement of Blood Flow in Extracranial Carotid Arteries: Normal Subjects, SPIE Medical Imaging, Orlando, Florida, USA (2013).
- **MJ Negahdar**, J. Cha, M. Kadbi, J. Cebral, and A. Amini, Noninvasive 3D Pressure Calculation From PC-MRI Via Non-Iterative Harmonics-based Orthoghonal Projection: Constant Flow Experiment, IEEE Engineering in Medicine and Biology conference (EMBC), Osaka, Japan (2013).
- **MJ Negahdar**, J. Cha, M. Shakeri, M. Kendrick, M. Alshaher, I. Khodarahimi, M. Sharp, A. Yancey, J. Heidenreich, and A. Amini, Effect of Venc on Accuracy of Velocity Profiles in Multi-Slice Phase-Contrast MR Imaging of Stenotic Flow, International Symposium on Biomedical Imaging (ISBI) Madrid, Spain (2012).
- M. Kadbi, **MJ Negahdar**, J. Cha, M. Traughber, P. Martin, and A. Amini, Validation of 3D Ultra-Short TE (UTE) Phase-Contrast MRI For Imaging of Steady Flow: Initial Phantom Experiments, IEEE Engineering in Medicine and Biology conference (EMBC), San Diego, CA, USA (2012).

- V. Tavakoli, **MJ Negahdar**, M. Kendrick, M. Alshaher, M. Stoddard, A. Amini, A Biventricular Multimodal (MRI/Ultrasound) Cardiac Phantom, IEEE Engineering in Medicine and Biology conference (EMBS), San Diego, CA, USA (2012).
- M. Kadbi, H. Wang, **MJ Negahdar**, L. Warner, M. Traughber, P. Martin, and A. Amini, A Novel Phase-Corrected 3D Cine Ultra-Short TE (UTE) Phase-Contrast MRI Technique, IEEE Engineering in Medicine and Biology conference (EMBC), San Diego, CA, USA (2012).
- **MJ Negahdar**, M. Kadbi, M. Kotys, S. Fischer, and A. Amini, Flow Quantification in the Iliac Arteries with Fast Spiral Phase Contrast MRI, IEEE Engineering in Medicine and Biology conference (EMBS), Boston, MA, USA (2011).
- **MJ Negahdar**, M. Shakeri, E. McDowell, J. Wells, S. Harkema, and A. Amini, Cine Phase-Contrast MRI Measurement of CSF Flow in the Cervical Spine: A Pilot Study in Patients with Spinal Cord Injury, SPIE Medical Imaging, Orlando, FL, USA (2011).
- M. Kadbi, H. Wang, **MJ Negahdar**, M. Kotys, S. Fischer, and A. Amini, A real-time cine late gadolinium enhancement imaging method at 3T, 19th International Society of Magnetic Resonance in Medicine Annual Meeting (ISMRM), Montreal, Canada (2011).
- **MJ Negahdar**, M. Ardebilipour, and M. Mapar, A Method for Coverage Control in Wireless Sensor Networks With Two Degrees of Freedo*m,* Second International Conference on Electrical Engineering 2008 (ICEE 2008), Pakistan (2008).
- **MJ Negahdar**, M. Ardebilipour, and M. Mapar, Adaptive Method for Decreasing Over-covered Areas in Wireless Sensor Networks*,* The Fourth International Conference on Wireless and Mobile Communications (*ICWMC 2008*) Athens, Greece (2008).
- M. Mapar, A. Sotoudeh, and **MJ Negahdar,** The Optimum Value of Alpha in the Pre-specified Coverage Control Algorithm in Wireless Sensor Networks to Achieve Minimum Active Nodes, 4th IEEE/IFIP International Conference in Central Asia on Internet (ICI 2008), Uzbekistan (2008).